

# Simultaneous Measurement of Oscillation Parameters in Beam and Atmospheric Neutrino Data from Tokai-to-Kamioka and Super-Kamiokande Experiments

# Daniel Robert Clement Barrow

# Magdalen College, Oxford University

<sup>10</sup> A Dissertation Submitted to Oxford University

<sup>11</sup> for the Degree of Doctor of Philosophy

<sup>12</sup>

13                   **Simultaneous Measurement of**

14                   **Oscillation Parameters in Beam and**

15                   **Atmospheric Neutrino Data from**

16                   **Tokai-to-Kamioka and**

17                   **Super-Kamiokande Experiments**

18                   *Abstract*

19                   Lorem ipsum dolor sit amet, consectetur adipiscing elit, sed do eiusmod tempor incididunt ut labore et dolore magna aliqua. Nulla aliquet porttitor lacus luctus accumsan tortor posuere. Pulvinar neque laoreet suspendisse interdum. Sem viverra aliquet eget sit. Nunc sed velit dignissim sodales ut eu sem integer vitae. At erat pellentesque adipiscing commodo elit at imperdiet dui accumsan. Fames ac turpis egestas integer eget aliquet nibh. Scelerisque eu ultrices vitae auctor eu augue. Purus non enim praesent elementum facilisis leo vel. Sollicitudin nibh sit amet commodo. Vitae auctor eu augue ut. Vel quam elementum pulvinar etiam. A condimentum vitae sapien pellentesque habitant morbi tristique senectus. Viverra accumsan in nisl nisi scelerisque eu ultrices. Sed viverra ipsum nunc aliquet bibendum enim. Sit amet purus gravida quis. In vitae turpis massa

<sup>32</sup> sed elementum tempus egestas sed sed. Vivamus arcu felis bibendum  
<sup>33</sup> ut tristique et egestas. Senectus et netus et malesuada fames ac turpis.  
<sup>34</sup> Ac auctor augue mauris augue.

## 35 Declaration

36 This dissertation is the result of my own work, except where ex-  
37 plicit reference is made to the work of others, and has not been sub-  
38 mitted for another qualification to this or any other university. This  
39 dissertation does not exceed the word limit for the respective Degree  
40 Committee.

41 Daniel Robert Clement Barrow

42 ©The copyright of this thesis rests with the author and is made available under a Creative  
43 Commons Attribution Non-Commercial No Derivatives licence. Researchers are free to copy,  
44 distribute or transmit the thesis on the condition that they attribute it, that they do not use  
45 it for commercial purposes and that they do not alter, transform or build upon it. For any  
46 reuse or redistribution, researchers must make clear to others the licence terms of this work.

47

## Acknowledgements

48 at pretium nibh ipsum. Eget nunc scelerisque viverra mauris in aliquam. Arcu vitae  
49 elementum curabitur vitae nunc sed velit dignissim. Sed arcu non odio euismod lacinia  
50 at quis risus sed. Vitae tempus quam pellentesque nec nam aliquam sem et tortor.  
51 Viverra aliquet eget sit amet tellus cras adipiscing. Purus sit amet luctus venenatis  
52 lectus magna. In aliquam sem fringilla ut morbi tincidunt augue. Fermentum dui  
53 faucibus in ornare. Aliquam malesuada bibendum arcu vitae elementum curabitur  
54 vitae nunc sed.

55 Ultricies leo integer malesuada nunc vel risus commodo. Tellus cras adipiscing  
56 enim eu turpis egestas pretium. Dictumst quisque sagittis purus sit amet volutpat  
57 consequat mauris nunc. Vitae congue mauris rhoncus aenean vel elit scelerisque  
58 mauris pellentesque. Vel facilisis volutpat est velit egestas dui id ornare. Suscipit  
59 adipiscing bibendum est ultricies. At in tellus integer feugiat scelerisque varius  
60 morbi enim. Cras semper auctor neque vitae tempus. Commodo sed egestas egestas  
61 fringilla phasellus faucibus. Cras pulvinar mattis nunc sed blandit. Pretium viverra  
62 suspendisse potenti nullam ac tortor vitae. Purus sit amet volutpat consequat. Orci  
63 sagittis eu volutpat odio facilisis mauris. Sit amet massa vitae tortor condimentum  
64 lacinia quis. Commodo sed egestas egestas fringilla phasellus. Sed libero enim sed  
65 faucibus turpis. Vitae tempus quam pellentesque nec.

66 Blandit massa enim nec dui. Viverra tellus in hac habitasse platea dictumst vestibulu-  
67 lum. Bibendum enim facilisis gravida neque convallis. Sagittis nisl rhoncus mattis  
68 rhoncus urna neque. Nisl rhoncus mattis rhoncus urna neque. Ac tortor vitae purus  
69 faucibus ornare. Aenean sed adipiscing diam donec adipiscing tristique risus. Sapien  
70 nec sagittis aliquam malesuada bibendum. Et leo duis ut diam quam nulla. Tellus  
71 rutrum tellus pellentesque eu tincidunt tortor aliquam nulla facilisi. Fermentum leo

<sup>72</sup> vel orci porta non pulvinar neque. Eget sit amet tellus cras adipiscing enim eu. Sed  
<sup>73</sup> viverra tellus in hac habitasse platea dictumst vestibulum.

<sup>74</sup> Sit amet consectetur adipiscing elit. At varius vel pharetra vel turpis nunc eget  
<sup>75</sup> lorem. Elit scelerisque mauris pellentesque pulvinar pellentesque habitant morbi  
<sup>76</sup> tristique senectus. Odio euismod lacinia at quis risus sed vulputate odio. Vitae suscipit  
<sup>77</sup> tellus mauris a diam maecenas sed enim ut. Dignissim convallis aenean et tortor at  
<sup>78</sup> risus viverra. Diam sollicitudin tempor id eu. Erat velit scelerisque in dictum. Blandit  
<sup>79</sup> cursus risus at ultrices. Ac tortor vitae purus faucibus ornare suspendisse sed.

# **Contents**

80	<b>1</b>	<b>Introduction</b>	<b>1</b>
81	<b>2</b>	<b>Neutrino Oscillation Physics</b>	<b>2</b>
82	2.1	Discovery of Neutrinos . . . . .	3
83	2.2	Theory of Neutrino Oscillation . . . . .	4
84	2.2.1	Three Flavour Oscillations . . . . .	5
85	2.2.2	The MSW Effect . . . . .	9
86	2.3	Neutrino Oscillation Measurements . . . . .	10
87	2.3.1	Solar Neutrinos . . . . .	10
88	2.3.2	Atmospheric Neutrinos . . . . .	13
89	2.3.3	Accelerator Neutrinos . . . . .	16
90	2.3.4	Reactor Neutrinos . . . . .	19
91	2.4	Summary . . . . .	21
92	<b>3</b>	<b>T2K and SK Experiment Overview</b>	<b>24</b>
93	3.1	The Super-Kamiokande Experiment . . . . .	25
94	3.1.1	The SK Detector . . . . .	26
95	3.1.2	Calibration . . . . .	29
96	3.1.3	Data Acquisition and Triggering . . . . .	33
97	3.1.4	Cherenkov Radiation . . . . .	35
98	3.2	The Tokai to Kamioka Experiment . . . . .	36
99	3.2.1	The Neutrino Beam . . . . .	38
100	3.2.2	The Near Detector at 280m . . . . .	42
101	3.2.2.1	Fine Grained Detectors . . . . .	44
102	3.2.2.2	Time Projection Chambers . . . . .	46

104	3.2.2.3	$\pi^0$ Detector . . . . .	47
105	3.2.2.4	Electromagnetic Calorimeter . . . . .	48
106	3.2.2.5	Side Muon Range Detector . . . . .	49
107	3.2.3	The Interactive Neutrino GRID . . . . .	50
108	<b>4</b>	<b>Bayesian Statistics and Markov Chain Monte Carlo Techniques</b>	52
109	4.1	Bayesian Statistics . . . . .	53
110	4.2	Monte Carlo Simulation . . . . .	55
111	4.2.1	Markov Chain Monte Carlo . . . . .	56
112	4.2.2	Metropolis-Hastings Algorithm . . . . .	59
113	4.2.3	MCMC Optimisation . . . . .	60
114	4.3	Understanding the MCMC Results . . . . .	64
115	4.3.1	Marginalisation . . . . .	64
116	4.3.2	Parameter Estimation and Credible Intervals . . . . .	66
117	4.3.3	Bayesian Model Comparisons . . . . .	67
118	4.3.4	Comparison of MCMC Output to Expectation . . . . .	69
119	<b>5</b>	<b>Simulation, Reconstruction, and Event Selections</b>	71
120	5.1	Simulation . . . . .	71
121	5.2	Event Reconstruction at SK . . . . .	76
122	5.3	Event Reduction at SK . . . . .	87
123	<b>6</b>	<b>Oscillation Probability Calculation</b>	92
124	6.1	Overview . . . . .	93
125	6.2	Treatment of Fast Oscillations . . . . .	101
126	6.3	Calculation Engine . . . . .	107
127	6.4	Matter Density Profile . . . . .	110
128	6.5	Production Height Averaging . . . . .	116

<b>129</b>	<b>Bibliography</b>	<b>120</b>
<b>130</b>	<b>List of Figures</b>	<b>131</b>
<b>131</b>	<b>List of Tables</b>	<b>139</b>



<sup>133</sup> Chapter 1

<sup>134</sup> Introduction

<sup>135</sup> **Chapter 2**

<sup>136</sup> **Neutrino Oscillation Physics**

<sup>137</sup> When first proposed, neutrinos were expected to be massless fermions that only in-  
<sup>138</sup> teract through weak and gravitational forces. This meant they were very difficult to  
<sup>139</sup> detect as they can pass through significant amounts of matter without interacting. De-  
<sup>140</sup> spite this, experimental neutrino physics has developed with many different detection  
<sup>141</sup> techniques and neutrino sources being used today. In direct tension with **the** standard  
<sup>142</sup> model physics, neutrinos have been determined to oscillate between different lepton  
<sup>143</sup> flavours, requiring them to have mass.

<sup>144</sup> **The observation techniques which lead to the discovery of the neutrino are doc-**  
<sup>145</sup> **umented in section 2.1.** The theory underpinning neutrino oscillation is described  
<sup>146</sup> in section 2.2. **This section and** includes the approximations which can be made to  
<sup>147</sup> simplify the understanding of neutrino oscillation in **a the** two-flavour approxima-  
<sup>148</sup> **tion as well as how the medium in which neutrinos propagate can manipulate the**  
<sup>149</sup> **oscillation probability. The past Past**, current, and future neutrino experiments are  
<sup>150</sup> detailed in section 2.3, including the reactor, atmospheric, and long-baseline accelerator  
<sup>151</sup> neutrino sources that have been used to successfully constrain oscillation **parameters**  
<sup>152</sup> **determination. Finally, the current state of oscillation parameter measurements are**  
<sup>153</sup> **summarised in section 2.4.**

## <sup>154</sup> 2.1 Discovery of Neutrinos

<sup>155</sup> At the start of the 20<sup>th</sup> century, the electrons emitted from the  $\beta$ -decay of the nucleus  
<sup>156</sup> were found to have a continuous energy spectrum [1,2]. This observation seemingly  
<sup>157</sup> broke the energy conservation invoked within that period's nuclear models. Postulated  
<sup>158</sup> in 1930 by Pauli as the solution to this problem, the neutrino (originally termed  
<sup>159</sup> "neutron") was theorized to be an electrically neutral spin-1/2 fermion with a mass  
<sup>160</sup> of the same order of magnitude as the electron [3]. This neutrino was to be emitted  
<sup>161</sup> with the electron in  $\beta$ -decay to alleviate the apparent breaking of energy conservation.  
<sup>162</sup> As a predecessor of **the today's** weak interaction model, Fermi's theory of  $\beta$ -decay  
<sup>163</sup> developed the understanding by coupling the four constituent particles; electron,  
<sup>164</sup> proton, neutron, and neutrino, into a consistent model [4].

<sup>165</sup> Whilst Pauli was not convinced of the ability to detect neutrinos, **the first obser-**  
<sup>166</sup> **vations of the particle were made in the mid-1950s when neutrinos from a reactor**  
<sup>167</sup> **were observed via the inverse  $\beta$ -decay (IBD) process,  $\bar{\nu}_e + p \rightarrow n + e^+$  [5,6]. The**  
<sup>168</sup> **detector consisted of two parts: a neutrino interaction medium and a liquid scintillator.**  
<sup>169</sup> **The interaction medium was built from two water tanks. These were loaded with**  
<sup>170</sup> **cadmium chloride to allow increased efficiency of neutron capture. The positron**  
<sup>171</sup> **emitted from IBD annihilates,  $e^+ + e^- \rightarrow 2\gamma$ , generating a prompt signal and the**  
<sup>172</sup> **neutron is captured on the cadmium via  $n + ^{108}Cd \rightarrow ^{109^*}Cd \rightarrow ^{109}Cd + \gamma$ , producing**  
<sup>173</sup> **a delayed signal. **The experiment observed an increase in the neutrino event rate****  
<sup>174</sup> ****when the reactor was operating compared to when it was switched off, in much the****  
<sup>175</sup> ****same way as modern reactor neutrino experiments operate. An increase in the coinci-****  
<sup>176</sup> ****dence rate was observed when the reactor was operating which was interpreted****  
<sup>177</sup> ****as interactions from neutrinos generated in the reactor.****

After the discovery of the  $\nu_e$ , the natural question of how many flavours of neutrino exist was asked. In 1962, a measurement of the  $\nu_\mu$  was conducted at the Brookhaven National Laboratory [7]. A proton beam was directed at a beryllium target, generating a  $\pi$ -dominated beam which then decayed via  $\pi^\pm \rightarrow \mu^\pm + (\nu_\mu, \bar{\nu}_\mu)$ , and the subsequent interactions of the  $\nu_\mu$  were observed. **As the subsequent interaction of the neutrino generates muons rather than electrons, it was determined the  $\nu_\mu$  was fundamentally different from  $\nu_e$ .** The final observation to be made was that of the  $\nu_\tau$  from the DONUT experiment [8]. Three neutrinos seem the obvious solution as it mirrors the known number of charged lepton (as they form weak isospin doublets) but there could be evidence of more. Several neutrino experiments have found anomalous results [9, 10] which could be attributed to sterile neutrinos. **However, however cosmological observations indicate the number of neutrino species  $N_{eff} = 2.99 \pm 0.17$  [11], as measured from the cosmic microwave background power spectrum, and Stanford Linear Accelerator found the number of active neutrino flavours to be  $N_\nu 2.9840 \pm 0.0082$  [12] from measurements of the Z-decay width.**

## 2.2 Theory of Neutrino Oscillation

As direct evidence of beyond Standard Model physics, a neutrino generated with lepton flavour  $\alpha$  can change into a different lepton flavour  $\beta$  after propagating some distance. This phenomenon is called neutrino oscillation and requires that neutrinos must have a non-zero mass (as seen in subsection 2.2.1). This **observation** is direct evidence of beyond standard model physics. This behaviour has been characterised by the Pontecorvo-Maki-Nakagawa-Sakata (PMNS) [13–15] mixing matrix which describes how the flavour and mass of neutrinos are associated. This is analogous to the Cabibbo-Kobayashi-Maskawa (CKM) [16] matrix measured in quark physics.

### <sup>203</sup> 2.2.1 Three Flavour Oscillations

<sup>204</sup> The PMNS parameterisation defines three flavour eigenstates,  $\nu_e$ ,  $\nu_\mu$  and  $\nu_\tau$  (indexed  
<sup>205</sup>  $\nu_\alpha$ ), which are **assigned based upon eigenstates of** the weak interaction **flavour states**  
<sup>206</sup> and three mass eigenstates,  $\nu_1$ ,  $\nu_2$  and  $\nu_3$  (indexed  $\nu_i$ ). Each mass eigenstate is the  
<sup>207</sup> superposition of all three flavour states,

$$|\nu_i\rangle = \sum_{\alpha} U_{\alpha i} |\nu_{\alpha}\rangle. \quad (2.1)$$

<sup>208</sup> Where  $U$  is the PMNS matrix which **is unitary and connects correlates** the mass  
<sup>209</sup> and flavour eigenstates.

<sup>210</sup> **Neutrinos interact with leptons of the same weak flavour eigenstate rather than**  
<sup>211</sup> **mass eigenstate. The weak interaction couples to flavour eigenstates so neutrinos**  
<sup>212</sup> **interact with leptons of the same flavour.** The propagation of a neutrino flavour  
<sup>213</sup> eigenstate, in a vacuum, can be re-written as a plane-wave solution to the time-  
<sup>214</sup> dependent Schrödinger equation,

$$|\nu_{\alpha}(t)\rangle = \sum_i U_{\alpha i}^{*} |\nu_i\rangle e^{-i\phi_i}. \quad (2.2)$$

<sup>215</sup> The probability of observing a neutrino of flavour eigenstate  $\beta$  from one which  
<sup>216</sup> originated as flavour  $\alpha$  can be calculated as,

$$P(\nu_\alpha \rightarrow \nu_\beta) = |\langle \nu_\beta | \nu_\alpha(t) \rangle|^2 = \sum_{i,j} U_{\alpha i}^* U_{\beta i} U_{\alpha j} U_{\beta j}^* e^{-i(\phi_j - \phi_i)} \quad (2.3)$$

<sup>217</sup> The  $\phi_i$  term can be expressed in terms of the energy,  $E_i$ , and magnitude of the  
<sup>218</sup> three momenta,  $p_i$ , of the neutrino,  $\phi_i = E_i t - p_i x$  ( $t$  and  $x$  being time and position  
<sup>219</sup> coordinates). Therefore,

$$\phi_j - \phi_i = E_j t - E_i t - p_j x + p_i x. \quad (2.4)$$

<sup>220</sup> For a relativistic particle,  $E_i \gg m_i$ ,

$$p_i = \sqrt{E_i^2 - m_i^2} \approx E_i - \frac{m_i^2}{2E_i}. \quad (2.5)$$

<sup>221</sup> Making the approximations that neutrinos are relativistic, the mass eigenstates  
<sup>222</sup> were created with the same energy and that  $x = L$ , where  $L$  is the distance traveled by  
<sup>223</sup> the neutrino, Equation 2.4 then becomes

$$\phi_j - \phi_i = \frac{\Delta m_{ij}^2 L}{2E}, \quad (2.6)$$

<sup>224</sup> where  $\Delta m_{ij}^2 = m_i^2 - m_j^2$ . This, **teamed combined** with further use of unitarity  
<sup>225</sup> relations results in Equation 2.3 becoming

$$P(\nu_\alpha \rightarrow \nu_\beta) = \delta_{\alpha\beta} - 4 \sum_{i>j} \Re \left( U_{\alpha i}^* U_{\beta i} U_{\alpha j} U_{\beta j}^* \right) \sin^2 \left( \frac{\Delta m_{ij}^2 L}{4E} \right) \quad (2.7)$$

$$+ (-) 2 \sum_{i>j} \Im \left( U_{\alpha i}^* U_{\beta i} U_{\alpha j} U_{\beta j}^* \right) \sin \left( \frac{\Delta m_{ij}^2 L}{2E} \right).$$

<sup>226</sup> Where  $\delta_{\alpha\beta}$  is the Kronecker delta function and the negative sign **on the last term** is  
<sup>227</sup> included for the oscillation probability of antineutrinos.

<sup>228</sup> Typically, the PMNS matrix is parameterised into three mixing angles, a charge  
<sup>229</sup> parity (CP) violating phase  $\delta_{CP}$ , and two Majorana phases  $\alpha_{1,2}$ ,

$$U = \underbrace{\begin{pmatrix} 1 & 0 & 0 \\ 0 & c_{23} & s_{23} \\ 0 & -s_{23} & c_{23} \end{pmatrix}}_{\text{Atmospheric, Accelerator}} \underbrace{\begin{pmatrix} c_{13} & 0 & s_{13}e^{-i\delta_{CP}} \\ 0 & 1 & 0 \\ -s_{13}e^{-i\delta_{CP}} & 0 & c_{13} \end{pmatrix}}_{\text{Reactor, Accelerator}} \underbrace{\begin{pmatrix} c_{12} & s_{12} & 0 \\ -s_{12} & c_{12} & 0 \\ 0 & 0 & 1 \end{pmatrix}}_{\text{Reactor, Solar}} \underbrace{\begin{pmatrix} e^{i\alpha_1/2} & 0 & 0 \\ 0 & e^{i\alpha_2/2} & 0 \\ 0 & 0 & 1 \end{pmatrix}}_{\text{Majorana}}. \quad (2.8)$$

<sup>230</sup> Where  $s_{ij} = \sin(\theta_{ij})$  and  $c_{ij} = \cos(\theta_{ij})$ . The oscillation parameters are often  
<sup>231</sup> grouped; (1,2) as “solar”, (2,3) as “atmospheric” and (1,3) as “reactor”. Many  
<sup>232</sup> neutrino experiments aim to measure the PMNS parameters from a wide array of  
<sup>233</sup> origins, as is the purpose of this thesis.

<sup>234</sup> The Majorana phase,  $\alpha_{1,2}$ , **containing matrix** included within **the fourth matrix**  
<sup>235</sup> **in** Equation 2.8 is only included for completeness. For an oscillation analysis ex-  
<sup>236</sup> periment, **any term in this oscillation probability calculation containing this phase**  
<sup>237</sup> **disappears any terms containing this phase disappear** due to taking the expectation

<sup>238</sup> value of the PMNS matrix. Measurements of these phases are typically performed  
<sup>239</sup> by experiments searching for neutrino-less double  $\beta$ -decay [17].

<sup>240</sup> A two flavour approximation can be attained obtained when one assumes the third  
<sup>241</sup> mass eigenstate is degenerate with another. As discussed in section 2.3, it is found  
<sup>242</sup> that  $\Delta m_{21}^2 \ll |\Delta m_{31}^2|$ . This results in the two flavour approximation being reasonable  
<sup>243</sup> for understanding the features of the oscillation. In this two flavour case, the mixing  
<sup>244</sup> matrix becomes,

$$U_{\text{2 Flav.}} = \begin{pmatrix} \cos(\theta) & \sin(\theta) \\ -\sin(\theta) & \cos(\theta) \end{pmatrix}. \quad (2.9)$$

<sup>245</sup> This culminates in the oscillation probability,

$$\begin{aligned} P(\nu_\alpha \rightarrow \nu_\alpha) &= 1 - \sin^2(2\theta) \sin^2\left(\frac{\Delta m^2 L}{4E}\right), \\ P(\nu_\alpha \rightarrow \nu_\beta) &= \sin^2(2\theta) \sin^2\left(\frac{\Delta m^2 L}{4E}\right). \end{aligned} \quad (2.10)$$

<sup>246</sup> For Where  $\alpha \neq \beta$ . For a fixed neutrino energy, the oscillation probability is a sinu-  
<sup>247</sup> soidal function depending upon the distance over which the neutrino propagates. The  
<sup>248</sup> frequency and amplitude of oscillation are dependent upon the ratio of the  $\Delta m^2 / 4E$   
<sup>249</sup> and  $\sin^2 2\theta$ , respectively. The oscillation probabilities presented thus far assume  
<sup>250</sup>  $c = 1$ , where  $c$  is the speed of light in vacuum. In more familiar units, the maxi-  
<sup>251</sup> mum oscillation probability for a fixed value of  $\theta$  is given at  $L[\text{km}] / E[\text{GeV}] \sim 1.27 / \Delta m^2$ .  
<sup>252</sup> It is this calculation that determines the best  $L/E$  value for a given experiment to be  
<sup>253</sup> designed around for measurements of a specific value of  $\Delta m^2$ .

## <sup>254</sup> 2.2.2 The MSW Effect

<sup>255</sup> The theory of neutrino oscillation in a vacuum **is has been** described in subsection 2.2.1.  
<sup>256</sup> However, the beam neutrinos and atmospheric neutrinos originating from below the  
<sup>257</sup> horizon propagate through matter in the Earth. The coherent scattering of neutrinos  
<sup>258</sup> from a material target modifies the Hamiltonian of the system. This results in a change  
<sup>259</sup> in the oscillation probability. Notably, charged current scattering ( $\nu_e + e^- \rightarrow \nu_e + e^-$ ,  
<sup>260</sup> propagated by a W boson) only affects electron neutrinos **compared to whereas** the  
<sup>261</sup> neutral current scattering ( $\nu_l + l^- \rightarrow \nu_l + l^-$ , propagated by a  $Z^0$  boson) interacts  
<sup>262</sup> through all neutrino flavours equally. In the two-flavour **limit approximation**, the  
<sup>263</sup> effective mixing parameter becomes

$$\sin^2(2\theta) \rightarrow \sin^2(2\theta_m) = \frac{\sin^2(2\theta)}{(A/\Delta m^2 - \cos(2\theta))^2 + \sin^2(2\theta)}, \quad (2.11)$$

<sup>264</sup> where  $A = 2\sqrt{2}G_F N_e E$ , **with**  $N_e$  is the electron density of the medium and  $G_F$  is  
<sup>265</sup> Fermi's constant. It is clear to see that there exists a value of  $A = \Delta m^2 \cos(2\theta)$  for  
<sup>266</sup>  $\Delta m^2 > 0$  which results in a divergent mixing parameter. This resonance is **due to**  
<sup>267</sup> **termed** the Mikheyev-Smirnov-Wolfenstein (MSW) effect (or more colloquially, the  
<sup>268</sup> matter resonance) which regenerates the electron neutrino component of the neutrino  
<sup>269</sup> flux [18–20]. The density at which the resonance occurs is given by

$$N_e = \frac{\Delta m^2 \cos(2\theta)}{2\sqrt{2}G_F E}. \quad (2.12)$$

270 At densities lower than this critical value, the oscillation probability will be much  
271 closer to that of vacuum oscillation. **For antineutrinos,  $N_e \rightarrow -N_e$**  [21]. The reso-  
272 nance occurring from the MSW effect depends on the sign of  $\Delta m^2$ . Therefore, any  
273 neutrino oscillation experiment which observes neutrinos and antineutrinos which  
274 have propagated through matter can have some sensitivity to the ordering of the  
275 neutrino mass eigenstates.

## 276 2.3 Neutrino Oscillation Measurements

277 As evidence of beyond standard model physics, the 2015 Nobel Prize in Physics was  
278 awarded to the Super-Kamiokande (SK) [22] and Sudbury Neutrino Observatory  
279 (SNO) [23] collaborations for the first definitive observation of solar and atmospheric  
280 neutrino oscillation [24]. Since then, the field has seen a wide array of oscillation  
281 measurements from a variety of neutrino sources. As seen in subsection 2.2.1, the  
282 neutrino oscillation probability is dependent on the ratio of the propagation baseline,  $L$ ,  
283 to the neutrino energy,  $E$ . It is this ratio that determines the type of neutrino oscillation  
284 a particular experiment is sensitive to.

285 As illustrated in Figure 2.1, there are many neutrino sources that span a wide  
286 range of energies. The least energetic neutrinos are from diffuse supernovae and  
287 terrestrial neutrinos at  $O(1)$ MeV whereas the most energetic neutrinos originate from  
288 atmospheric and galactic neutrinos of  $> O(1)$ TeV.

### 289 2.3.1 Solar Neutrinos

290 Solar neutrinos are emitted from fusion reaction chains at the center of the Sun. The  
291 solar neutrino flux, given as a function of neutrino energy for different fusion and

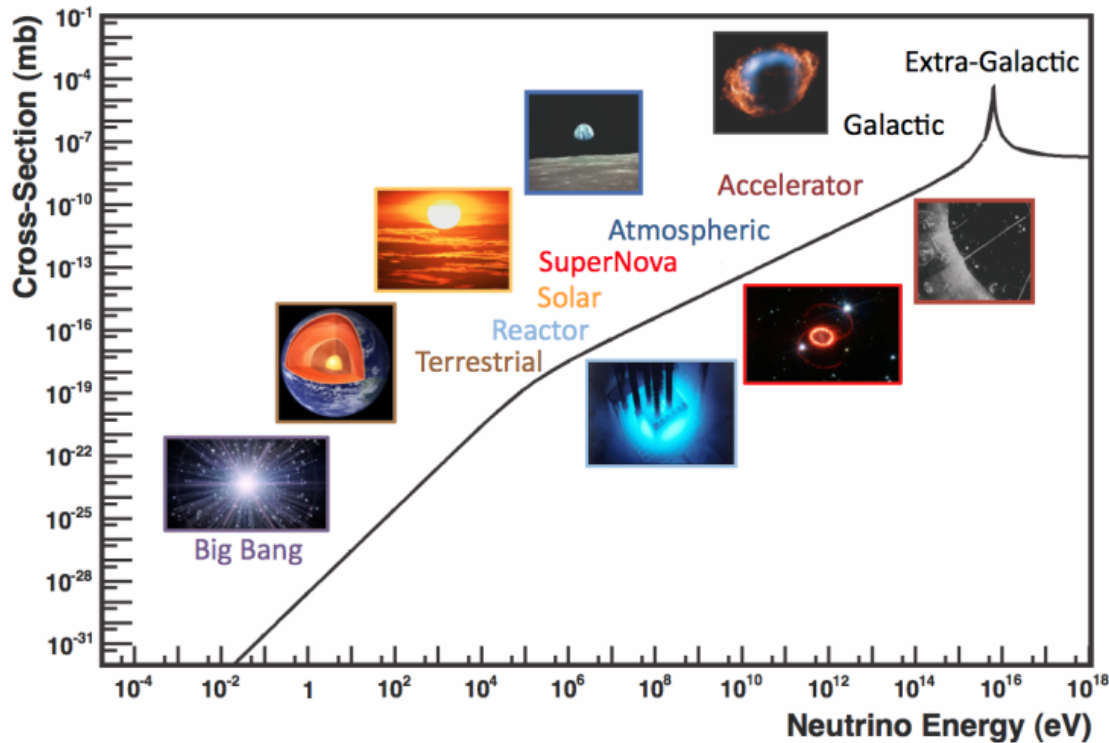


**Figure 2.1:** The cross-section of neutrinos from various natural and man-made sources as a function of neutrino energy. Taken from [25]

decay chains, is illustrated in Figure 2.2. Whilst proton-proton fusion generates the largest flux of neutrinos, the neutrinos are of low energy and are difficult to reconstruct due to the IBD interaction threshold of 1.8MeV. Consequently, most experiments focus on the neutrinos from the decay of  ${}^8B$  (via  ${}^8B \rightarrow {}^8Be^* + e^+ + \nu_e$ ), which are higher energy.

The first measurements of solar neutrinos observed a significant reduction in the event rate compared to predictions from the Standard Solar Model [27, 28]. The proposed solution to this “solar neutrino problem” was  $\nu_e \leftrightarrow \nu_\mu$  oscillations in a precursory version of the PMNS model [29]. The Kamiokande [30], Gallex [31] and Sage [32] experiments confirmed the  $\sim 0.5$  factor deficit of solar neutrinos.

The conclusive solution to this problem was determined by the SNO collaboration [33]. Using a deuterium water target to observe  ${}^8B$  neutrinos, the event rate of charged current (CC), neutral current (NC), and elastic scattering (ES) interactions

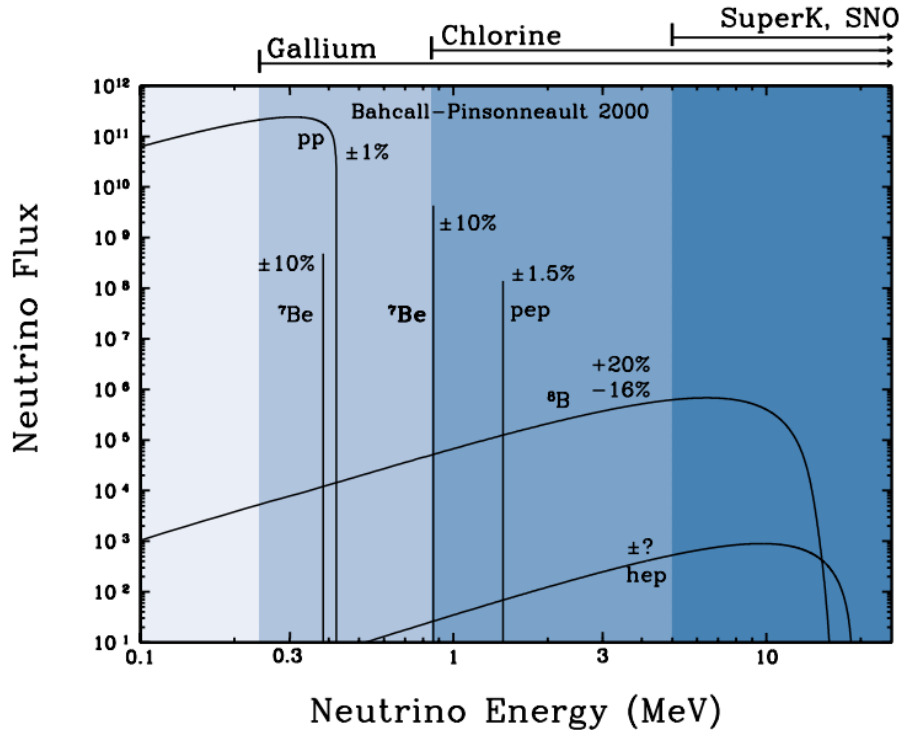
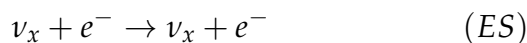
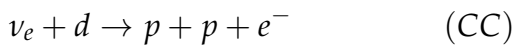


**Figure 2.2:** The solar neutrino flux as a function of neutrino energy for various fusion reactions and decay chains as predicted by the Standard Solar Model. Taken from [26].

(Given in Equation 2.13) was simultaneously measured. CC events can only occur for electron neutrinos, whereas the **other interaction NC channels are is** agnostic to neutrino flavour (**Although , and** the ES reaction **is more sensitive has a slight excess sensitivity** to electron neutrino interactions). This meant that there were direct measurements of the  $\nu_e$  and  $\nu_x$  neutrino flux. It was concluded that the CC and ES interaction rates were consistent with the deficit previously observed. Most importantly, the NC reaction rate was only consistent with the others under the hypothesis of flavour transformation.



<sup>313</sup> Many experiments have since measured the neutrino flux of different interaction  
<sup>314</sup> chains within the sun [34–36]. The most recent measurement was that of CNO neutrinos  
<sup>315</sup> which were recently observed with  $5\sigma$  significance by the Borexino collaboration.  
<sup>316</sup> Future neutrino experiments aim to further these spectroscopic measurements of  
<sup>317</sup> different fusion chains within the Sun [37–39]. Solar neutrinos act as an irreducible  
<sup>318</sup> background for dark matter experiments like DARWIN but oscillation parameter  
<sup>319</sup> measurements can be made [40].

### <sup>320</sup> 2.3.2 Atmospheric Neutrinos

<sup>321</sup> The interactions of primary cosmic ray protons in Earth’s upper atmosphere generate  
<sup>322</sup> showers of energetic hadrons. These are mostly pions and kaons which when they  
<sup>323</sup> decay produce a natural source of neutrinos spanning energies of MeV to TeV [41].  
<sup>324</sup> **This** The main decay is via

$$\begin{aligned} \pi^\pm &\rightarrow \mu^\pm + (\nu_\mu, \bar{\nu}_\mu) \\ \mu^\pm &\rightarrow e^\pm + (\nu_e, \bar{\nu}_e) + (\nu_\mu, \bar{\nu}_\mu) \end{aligned} \tag{2.14}$$

<sup>325</sup> such that for a single pion decay, three neutrinos are typically produced. The  
<sup>326</sup> atmospheric neutrino flux energy spectra as predicted by the Bartol [42], Honda  
<sup>327</sup> [43–45], and FLUKA [46] models are illustrated in Figure 2.3. The flux distribution  
<sup>328</sup> peaks at an energy of  $O(10)\text{GeV}$ . The uncertainties associated with these models  
<sup>329</sup> are dominated by the hadronic production of kaon and pions as well as the primary  
<sup>330</sup> cosmic flux.

<sup>331</sup> Unlike long-baseline experiments which have a fixed baseline, the distance at-  
<sup>332</sup> mospheric neutrinos propagate is dependent upon the zenith angle at which they

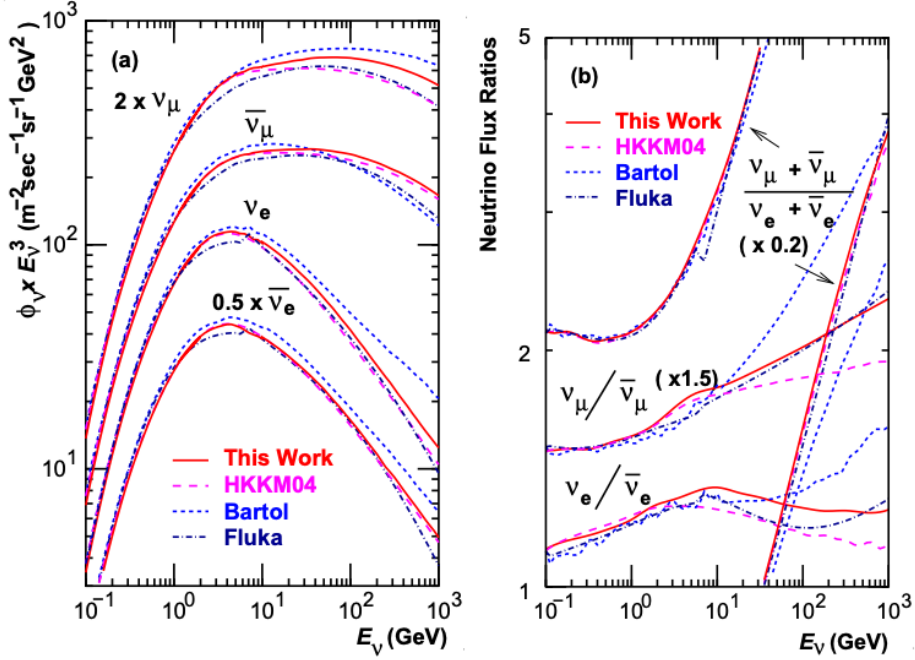


**Figure 2.3:** Left panel: The atmospheric neutrino flux for different neutrino flavours as a function of neutrino energy as predicted by the 2007 Honda model (“This work”) [43], the 2004 Honda model (“HKKM04”) [44], the Bartol model [42] and the FLUKA model [46]. Right panel: The ratio of the muon to electron neutrino flux as predicted by all the quoted models. Both figures taken from [43].

333 interact. This is illustrated in Figure 2.4. Neutrinos that are generated directly above  
 334 the detector ( $\cos(\theta) = 1.0$ ) have a baseline equivalent to the height of the atmosphere  
 335 whereas neutrinos that interact directly below the detector ( $\cos(\theta) = -1.0$ ) have to  
 336 travel a length equal to the diameter of the Earth. This means atmospheric neutrinos  
 337 have a baseline that varies from  $O(20)\text{km}$  to  $O(6 \times 10^3)\text{km}$ . Any neutrino generated  
 338 at or below the horizon will be subject to matter effects as they propagate through the  
 339 Earth.

340 Figure 2.5 highlights the neutrino flux as a function of the zenith angle for different  
 341 slices of neutrino energy. For medium to high-energy neutrinos (and to a lesser degree  
 342 for low-energy neutrinos), the flux is approximately symmetric around  $\cos(\theta) = 0$ .  
 343 To the accuracy of this approximation, the systematic uncertainties associated with  
 344 atmospheric flux for comparing upward-going and down-going neutrino cancels. This

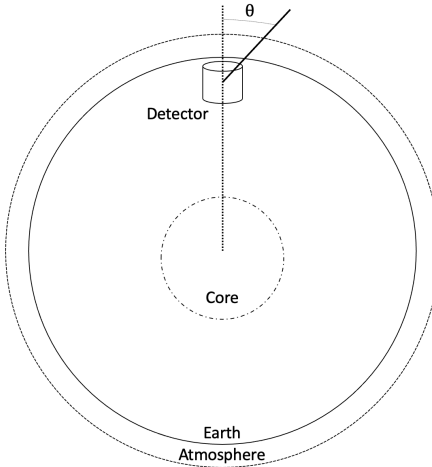


**Figure 2.4:** A diagram illustrating the definition of zenith angle as used in the Super Kamiokande experiment [47].

345 allows the down-going events, which are mostly insensitive to oscillation probabilities,  
 346 to act as an unoscillated prediction (similar to a near detector in an accelerator neutrino  
 347 experiment).

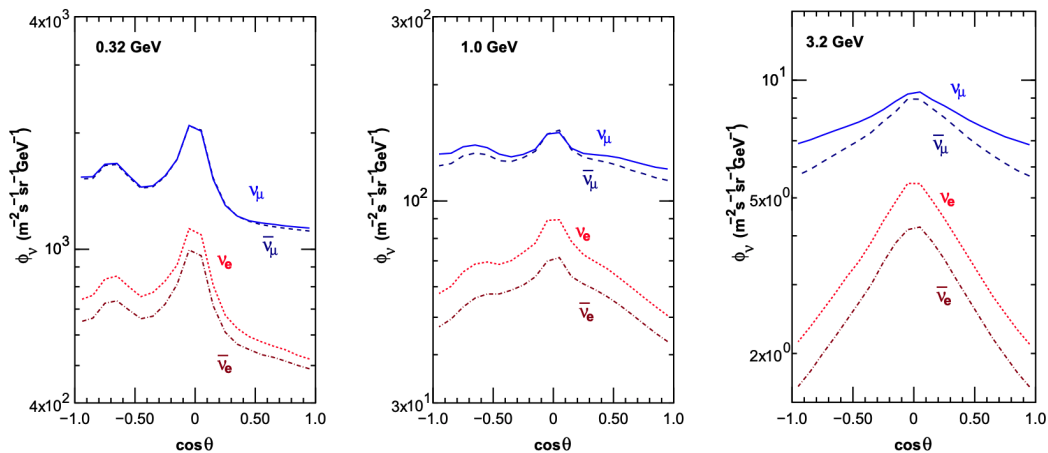


**Figure 2.5:** Prediction of  $\nu_e$ ,  $\bar{\nu}_e$ ,  $\nu_\mu$ ,  $\bar{\nu}_\mu$  fluxes as a function of zenith angle as calculated by the HKKM model [45]. The left, middle and right panels represent three values of neutrino energy, 0.32GeV, 1.0GeV and 3.2GeV respectively. Predictions for other models including Bartol [42], Honda [43] and FLUKA [46] are given in [47].

348 Precursory hints of atmospheric neutrinos were observed in the mid-1960s search-  
 349 ing for  $\nu_\mu^{(-)} + X \rightarrow X^* + \mu^\pm$  [48], although it was called an anomaly at the time of  
 350 measurement. This was succeeded with the IMB-3 [49] and Kamiokande [50] experi-

ments which measured the ratio of muon neutrinos compared to electron neutrinos  $R(\nu_\mu/\nu_e)$ . Both experiments were found to have a consistent deficit of muon neutrinos, with  $R(\nu_\mu/\nu_e) = 0.67 \pm 0.17$  and  $R(\nu_\mu/\nu_e) = 0.60^{+0.07}_{-0.06} \pm 0.05$ . Super-Kamiokande (SK) [47] extended this analysis by fitting oscillation parameters in  $P(\nu_\mu \rightarrow \nu_\tau)$  which found best fit parameters  $\sin^2(2\theta) > 0.92$  and  $1.5 \times 10^{-3} < \Delta m^2 < 3.4 \times 10^{-3} \text{ eV}^2$ .

Since then, atmospheric neutrino experiments have been making precision measurements of the  $\sin^2(\theta_{23})$  and  $\Delta m^2_{32}$  oscillation parameters. Atmospheric neutrino oscillation is dominated by  $P(\nu_\mu \rightarrow \nu_\tau)$ , where SK observed a  $4.6\sigma$  discovery of  $\nu_\tau$  appearance [51]. Figure 2.6 illustrates the current estimates on the atmospheric mixing parameters from a wide range of atmospheric and accelerator neutrino observatories.

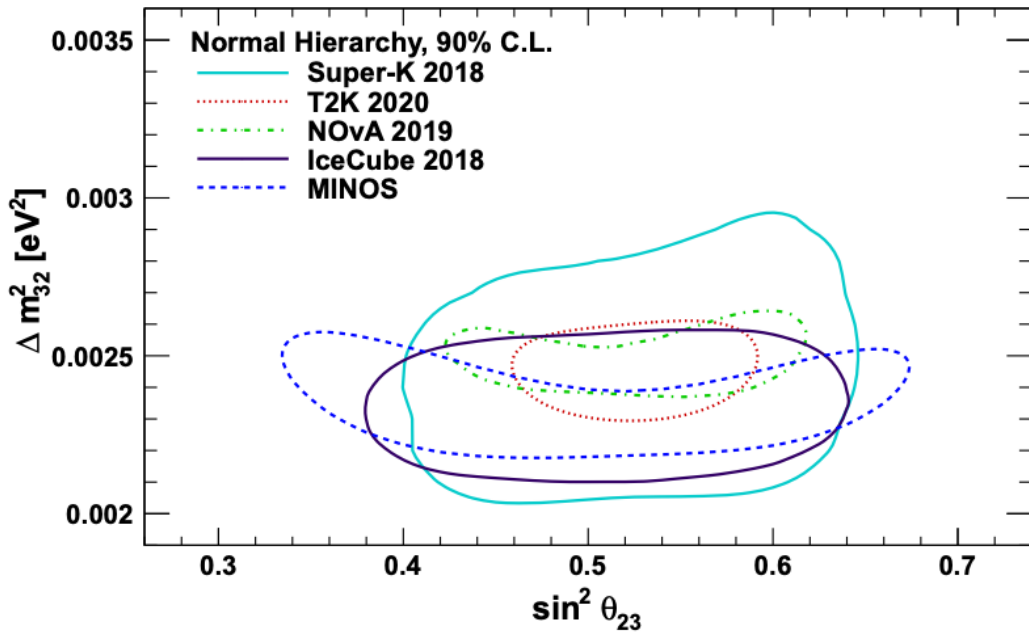


**Figure 2.6:** Constraints on the atmospheric oscillation parameters,  $\sin^2(\theta_{23})$  and  $\Delta m^2_{32}$ , from atmospheric and long baseline experiments: SK [52], T2K [53], NOvA [54], IceCube [55] and MINOS [56]. Figure taken from [57].

### <sup>361</sup> 2.3.3 Accelerator Neutrinos

<sup>362</sup> The concept of using a man-made “neutrino beam” was first realised in 1962 [58].  
<sup>363</sup> Since then, many experiments have followed which all use the same fundamental  
<sup>364</sup> concepts. Typically, a proton beam is aimed at a target producing charged mesons that  
<sup>365</sup> decay to neutrinos. The mesons can be sign-selected by the use of magnetic focusing  
<sup>366</sup> horns to generate a neutrino or antineutrino beam. Pions are the primary meson that  
<sup>367</sup> decay and depending on the orientation of the magnetic field, a muon (anti-)neutrino  
<sup>368</sup> beam is generated via  $\pi^+ \rightarrow \mu^+ + \nu_\mu$  or  $\pi^- \rightarrow \mu^- + \bar{\nu}_\mu$ . The decay of muons and  
<sup>369</sup> kaons does result in an irreducible intrinsic electron neutrino background. In T2K,  
<sup>370</sup> this background contamination is  $O(< 1\%)$  [59]. There is also an approximately  
<sup>371</sup>  $\sim 5\%$  “wrong-sign” neutrino background of  $\bar{\nu}_\mu$  generated via the same decays. **As**  
<sup>372</sup> **the beam is generated by proton interactions (rather than anti-proton interactions),**  
<sup>373</sup> **the wrong-sign component in the antineutrino beam is larger when operating in**  
<sup>374</sup> **neutrino mode.**

<sup>375</sup> **The energy of each neutrino in the beam is dependent on the energy of the**  
<sup>376</sup> **initial proton beam. Therefore, tuning the proton energy allows Tuning the proton**  
<sup>377</sup> **energy in the beam and using beam focusing techniques allows** the neutrino energy  
<sup>378</sup> to be set to a value that maximises the disappearance oscillation probability in the  $L/E$   
<sup>379</sup> term in Equation 2.10. This means that accelerator experiments are typically more  
<sup>380</sup> sensitive to the mixing parameters as compared to a natural neutrino source. However,  
<sup>381</sup> the disadvantage compared to atmospheric neutrino experiments is that the baseline  
<sup>382</sup> has to be shorter due to the lower flux. Consequently, there is typically less sensitivity  
<sup>383</sup> to matter effects and the ordering of the neutrino mass eigenstates.

<sup>384</sup> A neutrino experiment measures

$$R(\vec{x}) = \Phi(E_\nu) \times \sigma(E_\nu) \times \epsilon(\vec{x}) \times P(\nu_\alpha \rightarrow \nu_\beta), \quad (2.15)$$

385 where  $R(\vec{x})$  is the event rate of neutrinos at position  $\vec{x}$ ,  $\Phi(E_\nu)$  is the flux of neutrinos  
 386 with energy  $E_\nu$ ,  $\sigma(E_\nu)$  is the cross-section of the neutrino interaction and  $\epsilon(\vec{x})$  is the  
 387 efficiency **and resolution** of the detector. In order to leverage the most out of an  
 388 accelerator neutrino experiment, the flux and cross-section systematics need to be  
 389 constrained. This is typically done via the use of a “near detector”, situated at a baseline  
 390 of  $O(1)$ km. This detector observes the unoscillated neutrino flux and constrains the  
 391 parameters used within the flux and cross-section model.

392 The first accelerator experiments to precisely measure oscillation parameters were  
 393 MINOS [60] and K2K [61]. These experiments confirmed the  $\nu_\mu \rightarrow \nu_\mu$  **oscillations**  
 394  $\nu_\mu$  **disappearance** seen in atmospheric neutrino experiments by finding consistent  
 395 **mixing** parameter values for  $\sin^2(\theta_{23})$  and  $\Delta m_{23}^2$ . The current generation of accelera-  
 396 tor neutrino experiments, T2K and NO $\nu$ A extended this field by observing  $\bar{\nu}_\mu \rightarrow \bar{\nu}_e$   
 397 and lead the sensitivity to atmospheric mixing parameters as seen in Figure 2.6 [62].  
 398 The two experiments differ in their peak neutrino energy, baseline, and detection  
 399 technique. The NO $\nu$ A experiment is situated at a baseline of 810km from the NuMI  
 400 beamline which delivers 2GeV neutrinos. The T2K neutrino beam is peaked around  
 401 0.6GeV and propagates 295km. The NO $\nu$ A experiment also uses functionally iden-  
 402 tical detectors (near and far) which allow the approximate cancellation of detector  
 403 systematics whereas T2K uses a plastic scintillator technique at the near detector and  
 404 a water Cherenkov far detector. The future generation experiments DUNE [63] and  
 405 Hyper-Kamiokande [64] will succeed these experiments as the high-precision era of  
 406 neutrino oscillation parameter measurements develops.

<sup>407</sup> Several anomalous results have been observed in the LSND [9] and MiniBooNE [10]  
<sup>408</sup> detectors which were designed with purposefully short baselines. Parts of the neu-  
<sup>409</sup> trino community attributed these results to oscillations induced by a fourth “sterile”  
<sup>410</sup> neutrino [65] but several searches in other experiments, MicroBooNE [66] and KAR-  
<sup>411</sup> MEN [67], found no hints of additional neutrino species. The solution to the anomalous  
<sup>412</sup> results **are is** still being determined.

#### <sup>413</sup> 2.3.4 Reactor Neutrinos

<sup>414</sup> As illustrated in the first discovery of neutrinos (section 2.1), nuclear reactors are a very  
<sup>415</sup> useful man-made source of electron antineutrinos. For reactors that use low-enriched  
<sup>416</sup> uranium  $^{235}\text{U}$  as fuel, the antineutrino flux is dominated by the  $\beta$ -decay fission of  $^{235}\text{U}$ ,  
<sup>417</sup>  $^{238}\text{U}$ ,  $^{239}\text{Pu}$  and  $^{241}\text{Pu}$  [68] as illustrated in Figure 2.7.

<sup>418</sup> Due to their low energy, reactor electron antineutrinos predominantly interact  
<sup>419</sup> via the inverse  $\beta$ -decay (IBD) interaction. The typical signature contains two signals  
<sup>420</sup> delayed by  $O(200)\mu\text{s}$ ; firstly the prompt photons from positron annihilation, and  
<sup>421</sup> secondly the photons emitted ( $E_{tot}^\gamma = 2.2\text{MeV}$ ) from de-excitation after neutron capture  
<sup>422</sup> on hydrogen. Searching for both signals improves the detector’s ability to distinguish  
<sup>423</sup> between background and signal events [70]. Recently, SK included gadolinium dopants  
<sup>424</sup> into the ultra-pure water to increase the energy released from the photon cascade to  
<sup>425</sup>  $\sim 8\text{MeV}$  and reduce the time of the delayed signal to  $\sim 28\mu\text{s}$ .

<sup>426</sup> There are many short baseline experiments ( $L \sim O(1)\text{km}$ ) that have measured the  
<sup>427</sup>  $\sin^2(\theta_{13})$  and  $\Delta m_{23}^2$  oscillation parameters. Daya Bay [71], RENO [72] and Double  
<sup>428</sup> Chooz [73] have all provided precise measurements, with the first discovery of a  
<sup>429</sup> non-zero  $\theta_{13}$  made by Daya Bay and RENO (and **complimented complemented** by  
<sup>430</sup> T2K [73]). The constraints on  $\sin^2(\theta_{13})$  by the reactor experiments lead the field and

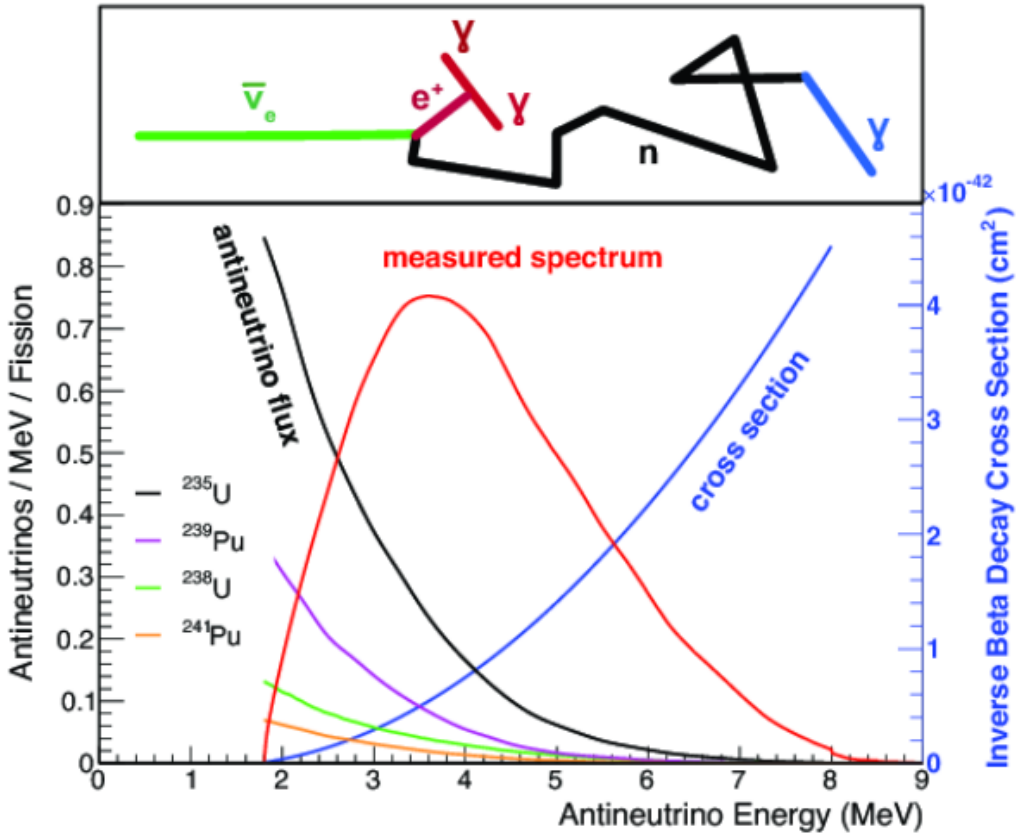


**Figure 2.7:** Reactor electron antineutrino fluxes for  $^{235}\text{U}$  (Black),  $^{238}\text{U}$  (Green),  $^{239}\text{Pu}$  (Purple), and  $^{241}\text{Pu}$  (Orange) isotopes. The inverse  $\beta$ -decay cross-section (Blue) and corresponding measurable neutrino spectrum (Red) are also given. Top panel: Schematic of Inverse  $\beta$ -decay interaction including the eventual capture of the emitted neutron. This capture emits a  $\gamma$ -ray which provides a second signal of the event. Taken from [69].

are often used as external inputs to accelerator neutrino experiments to improve their sensitivity to  $\delta_{CP}$  and mass hierarchy determination. JUNO-TAO [74], a small collaboration within the larger JUNO experiment, is a next-generation reactor experiment that aims to precisely measure the isotopic antineutrino yields from the different fission chains. Alongside this, it aims to explain the ‘5MeV excess’ [75–77] by conducting a search for sterile neutrinos with a mass scale of around 1eV.

Kamland [78] is the only experiment to have observed reactor neutrinos using a long baseline (flux weighted averaged baseline of  $L \sim 180\text{km}$ ) which allows it to have sensitivity to  $\Delta m_{12}^2$ . Combined with the SK solar neutrino experiment, the combined

<sup>440</sup> analysis puts the most stringent constraint on  $\Delta m_{12}^2$  [79] **which is used as a prior**  
<sup>441</sup> **uncertainty within accelerator neutrino experiments.**

## <sup>442</sup> 2.4 Summary

<sup>443</sup> Since observing the first evidence of neutrino oscillations in the late 1990's, numerous  
<sup>444</sup> measurements of the mixing parameters have been made. Many experiments use  
<sup>445</sup> neutrinos as a tool for discovery of new physics (diffuse supernova background,  
<sup>446</sup> neutrinoless double beta decay and others) so the PMNS parameters are summarised  
<sup>447</sup> in the Particle Data Group (PDG) review tables. The analysis presented in this thesis  
<sup>448</sup> focuses on the 2020 T2K oscillation analysis presented in [80] where the 2018 PDG  
<sup>449</sup> constraints [81] were used. These constraints are outlined in Table 2.1.

Parameter	2018 Constraint
$\sin^2(\theta_{12})$	$0.307 \pm 0.013$
$\Delta m_{21}^2$	$(7.53 \pm 0.18) \times 10^{-5} \text{ eV}^2$
$\sin^2(\theta_{13})$	$(2.12 \pm 0.08) \times 10^{-2}$
$\sin^2(\theta_{23})$ (I.H., Q1)	$0.421^{+0.033}_{-0.025}$
$\sin^2(\theta_{23})$ (I.H., Q2)	$0.592^{+0.023}_{-0.030}$
$\sin^2(\theta_{23})$ (N.H., Q1)	$0.417^{+0.025}_{-0.028}$
$\sin^2(\theta_{23})$ (N.H., Q2)	$0.597^{+0.024}_{-0.030}$
$\Delta m_{32}^2$ (I.H.)	$(-2.56 \pm 0.04) \times 10^{-3} \text{ eV}^2$
$\Delta m_{32}^2$ (N.H.)	$(2.51 \pm 0.05) \times 10^{-3} \text{ eV}^2$

**Table 2.1:** The 2018 Particle Data Group constraints of the oscillation parameters taken from [81]. The value of  $\Delta m_{23}^2$  is given for both normal hierarchy (N.H.) and inverted hierarchy (I.H.) and  $\sin^2(\theta_{23})$  is broken down by whether its value is below (Q1) or above (Q2) 0.5.

<sup>450</sup> The  $\sin^2(\theta_{13})$  measurement stems from the electron antineutrino disappearance,  
<sup>451</sup>  $P(\bar{\nu}_e \rightarrow \bar{\nu}_e)$ , and is take as the average best-fit from the combination of Daya Bay,  
<sup>452</sup> Reno and Double Chooz. It is often used as a prior uncertainty within other neu-

trino oscillation experiments, typically termed the reactor constraint. The  $\sin^2(\theta_{12})$  parameter is predominately measured through electron neutrino disappearance,  $P(\nu_e \rightarrow \nu_{\mu,\tau})$ , in solar neutrino experiments. The long-baseline reactor neutrino experiment Kamland also has sensitivity to this parameter and is used in a joint fit to solar data from SNO and SK, using the reactor constraint. Measurements of  $\sin^2(\theta_{23})$  are made by long-baseline and atmospheric neutrino experiments. The PDG value is a joint fit of T2K, NO $\nu$ A , MINOS and IceCube DeepCore experiments. The latest T2K-only measurement, provided at Neutrino2020 and is the basis of this thesis, is given as  $\sin^2(\theta_{23}) = 0.546^{+0.024}_{-0.046}$  [80]. The PDG constraint on  $\Delta m_{12}^2$  is provided by the KamLAND experiment using solar and geoneutrino data. This measurement utilised a  $\sin^2(\theta_{13})$  constraint from accelerator (T2K, MINOS) and reactor neutrino (Daya Bay, RENO, Double Chooz) experiments. Accelerator measurements make some of the most stringent constraints on  $\Delta m_{23}^2$  although atmospheric experiments have more sensitivity to the mass hierarchy determination. The PDG performs a joint fit of accelerator and atmospheric data, in both normal and inverted hierarchy separately. The latest T2K-only result is  $\Delta m_{32}^2 = 2.49^{+0.058}_{-0.082} \times 10^{-3} \text{ eV}^2$  favouring normal hierarchy [80]. The value of  $\delta_{CP}$  is largely undetermined. CP-conserving values of 0 and  $\pi$  were rejected with  $\sim 2\sigma$  intervals, as published in Nature, although more recent analysis have reduced the rejection intervals to 90%. Since the 2018 PDG publication, there has been a new measurement of  $\sin^2(\theta_{13}) = (2.20 \pm 0.07) \times 10^{-2}$  [82], alongside updated  $\Delta m_{23}^2$  and  $\sin^2(\theta_{23})$  measurements.

Throughout this thesis, several sample spectra predictions and contours are presented which require oscillation parameters to be assumed. Table 2.2 defines two sets of oscillation parameters, with “Asimov A” set being close to the preferred values from a previous T2K-only fit [83] and “Asimov B” being CP-conserving and further from maximal  $\theta_{23}$  mixing.

Parameter	Asimov A	Asimov B
$\Delta m_{12}^2$	$7.53 \times 10^{-5} \text{ eV}^2$	
$\Delta m_{32}^2$	$2.509 \times 10^{-3} \text{ eV}^2$	
$\sin^2(\theta_{12})$		0.304
$\sin^2(\theta_{13})$		0.0219
$\sin^2(\theta_{23})$	0.528	0.45
$\delta_{CP}$	-1.601	0.0

**Table 2.2:** Reference values of the neutrino oscillation parameters for two different oscillation parameter sets.

479

# Chapter 3

480

## T2K and SK Experiment Overview

481 As the successor of the Kamiokande experiment, the Super-Kamiokande (SK) collabora-  
482 ration has been leading atmospheric neutrino oscillation analyses for over two decades.  
483 The detector has provided some of the strongest constraints on proton decay **limits**  
484 and **as well as** the first precise measurements of the  $\Delta m_{23}^2$  and  $\sin^2(\theta_{23})$  neutrino  
485 oscillation parameters. **Despite this, the The** ability of the detector to low-energy  
486 neutrino events has been significantly improved with the recent gadolinium doping  
487 of the ultra-pure water target. **section 2.1 describes the history, detection technique,**  
488 **and operation of the SK detector. The history, detection technique, and operation**  
489 **of the SK detector is described in section 3.1.**

490 The Tokai-to-Kamioka (T2K) experiment was one of the first long-baseline ex-  
491 periments to use both neutrino and antineutrino beams to precisely measure the  
492 charge parity violation within the neutrino sector. With the SK detector observing  
493 the oscillated neutrino flux, the T2K experiment observed the first hints of a non-zero  
494  $\sin^2(\theta_{13})$  measurement and continues to lead the field with the constraints it provides  
495 on  $\sin^2(\theta_{13})$ ,  $\sin^2(\theta_{23})$ ,  $\Delta m_{23}^2$  and  $\delta_{CP}$ . **section 2.2 documents the The** techniques  
496 which T2K uses in generating its neutrino beam as well as the near-detector used  
497 to constrain the flux and cross-section parameters **invoked within the systematic**  
498 **models used in this analysis are documented in section 3.2.**

### <sup>499</sup> 3.1 The Super-Kamiokande Experiment

<sup>500</sup> The SK experiment began taking data in 1996 [84] and has had many modifications  
<sup>501</sup> throughout its lifespan. There have been seven defined periods of data taking as  
<sup>502</sup> noted in Table 3.1. Data taking began in SK-I which ran for five years. Between the  
<sup>503</sup> SK-I and SK-II periods, a significant proportion of the PMTs were damaged during  
<sup>504</sup> maintenance. Those that survived were equally distributed throughout the detector  
<sup>505</sup> in the SK-II era, which resulted in a reduced photo-coverage. From SK-III onwards,  
<sup>506</sup> repairs to the detector meant the full suite of PMTs was operational. Before the  
<sup>507</sup> start of SK-IV, the data acquisition and electronic systems were upgraded. Between  
<sup>508</sup> SK-IV and SK-V, a significant effort was placed into tank open maintenance and  
<sup>509</sup> repair/replacement of defective PMTs, a task for which the author of this thesis was  
<sup>510</sup> required. Consequently, the detector conditions were significantly different between  
<sup>511</sup> the two operational periods. SK-VI saw the start of the 0.01% gadolinium doped water.  
<sup>512</sup> SK-VII, which started during the writing of this thesis, has increased the gadolinium  
<sup>513</sup> concentration to 0.03% for continued operation [85].

Period	Start Date	End Date	Live-time (days)
I	April 1996	July 2001	1489.19
II	October 2002	October 2005	798.59
III	July 2006	September 2008	518.08
IV	September 2008	May 2018	3244.4
V	January 2019	July 2020	461.02
VI	July 2020	May 2022	583.3
VII	May 2022	Ongoing	N/A

**Table 3.1:** The various SK periods and respective live-time. The SK-VI live-time is calculated until 1<sup>st</sup> April 2022. SK-VII started during the writing of this thesis.

### <sup>514</sup> 3.1.1 The SK Detector

<sup>515</sup> The basic structure of the Super-Kamiokande (SK) detector is a cylindrical tank with a  
<sup>516</sup> diameter 39.3m and height 41.1m filled with ultrapure water [86]. A diagram of the  
<sup>517</sup> significant components of the SK detector is [illustrated given](#) in Figure 3.1. The SK  
<sup>518</sup> detector is situated in the Kamioka mine in Gifu, Japan. The mine is underground with  
<sup>519</sup> roughly 1km rock overburden (2.7km water equivalent overburden) [87]. At this depth,  
<sup>520</sup> the rate of cosmic ray muons is significantly decreased to a value of  $\sim 2\text{Hz}$ . The top of  
<sup>521</sup> the tank is covered with stainless steel which is designed as a working platform for  
<sup>522</sup> maintenance, calibration, and location for high voltage and data acquisition electronics.

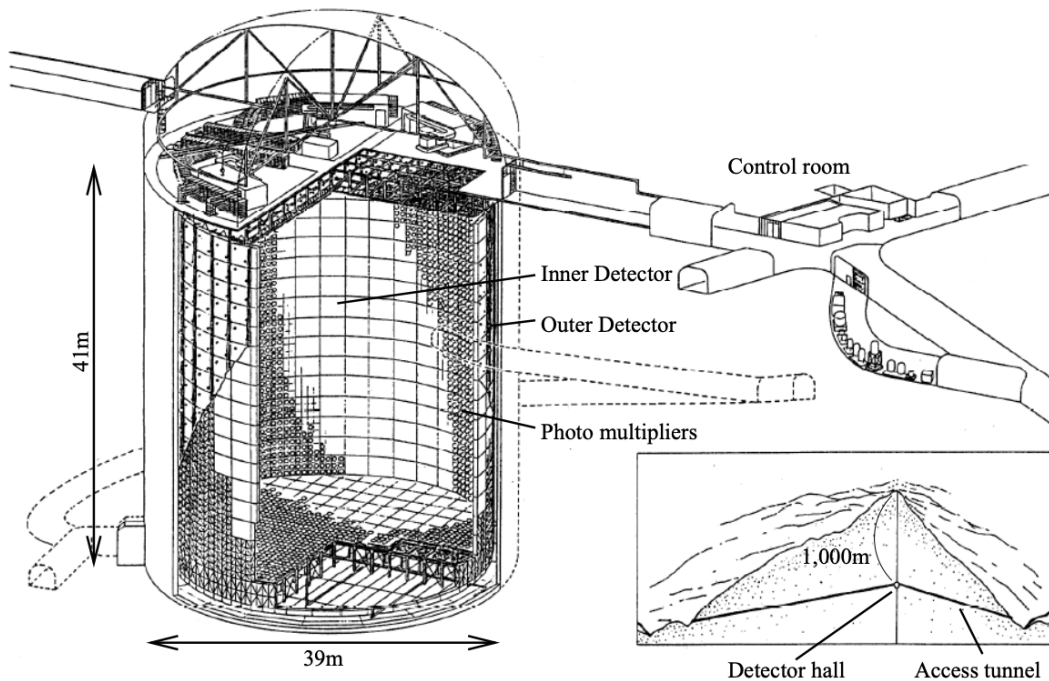


**Figure 3.1:** A schematic diagram of the Super-Kamiokande Detector. Taken from [88].

<sup>523</sup> A smaller cylindrical structure (36.2m diameter, 33.8m height) is situated inside the  
<sup>524</sup> tank, with an approximate 2m gap between this structure and the outer tank wall. The  
<sup>525</sup> purpose of this structure is to support the photomultiplier tubes (PMTs). The volume  
<sup>526</sup> inside and outside the support structure is referred to as the inner detector (ID) and

527 outer detector (OD), respectively. In the SK-IV era, the ID and OD are instrumented  
528 by 11,129 50cm and 1,885 20cm PMTs respectively [86]. The ID contains a 32kton  
529 mass of water. Many analyses performed at SK use a “fiducial volume” defined by the  
530 volume of water inside the ID excluding some distance to the ID wall. This reduces the  
531 volume of the detector which is sensitive to neutrino events but reduces radioactive  
532 backgrounds and allows for better reconstruction performance. The nominal fiducial  
533 volume is defined as the area contained inside 2m from the ID wall for a total of  
534 22.5kton water [89].

535 The two regions of the detector (ID and OD) are optically separated with opaque  
536 black plastic. The purpose of this is to determine whether a track entered or exited  
537 the ID. This allows cosmic ray muons and partially contained events to be tagged and  
538 separated from neutrino events entirely contained within the ID. This black plastic is  
539 also used to cover the area between the ID PMTs to reduce photon reflection from the  
540 ID walls. Opposite to this, the OD is lined with a reflective material to allow photons to  
541 reflect around inside the OD until collected by one of the PMTs. Furthermore, each OD  
542 PMT is backed with  $50 \times 50\text{cm}$  plates of wavelength shifting acrylic which increases  
543 the efficiency of light collection [87].

544 In the SK-IV data-taking period, the photocathode coverage of the detector, or the  
545 fraction of the ID wall instrumented with PMTs, is  $\sim 40\%$  [87]. The PMTs have a  
546 quantum efficiency (the ratio of detected electrons to incident photons) of  $\sim 21\%$  for  
547 photons with wavelengths of  $360\text{nm} < \lambda < 390\text{nm}$ . The proportion of photoelectrons  
548 that produce a signal in the dynode of a PMT, termed the collection efficiency, is  
549  $> 70\%$  [87]. The PMTs used within SK are most sensitive to photons with wavelength  
550  $300\text{nm} \leq \lambda \leq 600\text{nm}$  [87]. One disadvantage of using PMTs as the detection media  
551 is that the Earth’s geomagnetic field can modify its response. Therefore, a set of

compensation coils is built around the inner surface of the detector to mitigate this effect [90].

As mentioned, the SK detector is filled with ultrapure water, which in a perfect world would contain no impurities. However, bacteria and organic compounds can significantly degrade the water quality. This decreases the attenuation length, which reduces the total number of photons that hit a PMT. To combat this, a sophisticated water treatment system has been developed [87, 91]. UV lights, mechanical filters, and membrane degasifiers are used to reduce the bacteria, suspended particulates, and radioactive materials from the water. The flow of water within the tank is also critical as it can remove stagnant bacterial growth or build-up of dust on the surfaces within the tank. Gravity drifts impurities in the water towards the bottom of the tank which, if left uncontrolled, can create asymmetric water conditions between the top and bottom of the tank. Typically, the water entering the tank is cooled below the ambient temperature of the tank to control convection and inhibit bacteria growth. Furthermore, the **rate of** dark noise hits within PMTs is sensitive to the PMT temperature [92] so controlling the temperature gradients within the tank is beneficial for stable measurements.

SK-VI is the first phase of the SK experiment to use gadolinium dopants within the ultrapure water [85]. As such, the SK water system had to be replaced to avoid removing the gadolinium concentrate from the ultrapure water [93]. For an inverse  $\beta$ -decay (IBD) interaction in a water target, the emitted neutron is thermally captured on hydrogen. This process releases 2.2MeV  $\gamma$  rays which are difficult to detect **due to as the resulting** Compton scattered electrons ~~from a  $\gamma$  ray of this energy is are~~ very close to the Cherenkov threshold, limiting the number of photons produced. Thermal capture of neutrons on gadolinium generates  $\gamma$  rays with higher energy (8MeV [70]) meaning they are more easily detected. SK-VI has 0.01% Gd loading

578 (0.02% gadolinium sulphate by mass) which causes  $\approx 50\%$  of neutrons emitted by IBD  
579 to be captured on gadolinium [94, 95]. Whilst predominantly useful for low energy  
580 analyses, Gd loading allows better  $\nu/\bar{\nu}$  separation for atmospheric neutrino event  
581 selections [96]. Efforts are currently in place to increase the gadolinium concentrate  
582 to 0.03% for  $\approx 75\%$  neutron capture efficiency on gadolinium [97]. The final stage of  
583 loading targets 0.1% concentrate.

### 584 3.1.2 Calibration

585 The calibration of the SK detector is documented in [86] and summarised below. The  
586 analysis presented within this thesis is dependent upon ‘high energy events’ (Charged  
587 particles with  $O(> 100)\text{MeV}$  momenta). These are events that are expected to generate  
588 a larger number of photons such that each PMT will be hit with multiple photons.  
589 The reconstruction of these events depends upon the charge deposited within each  
590 PMT and the timing response of each individual PMT. Therefore, the most relevant  
591 calibration techniques to this thesis are outlined.

592 Before installation, 420 PMTs were calibrated to have identical charge responses  
593 and then distributed throughout the tank in a cross-shape pattern (As illustrated by  
594 Figure 3.2). These are used as a standardised measure for the rest of the PMTs installed  
595 at similar geometric positions within SK to be calibrated against. To perform this  
596 calibration, a xenon lamp is located at the center of the SK tank which flashes uniform  
597 light at 1Hz. This allows for geometrical effects, water quality variation, and timing  
598 effects to be measured in-situ throughout normal data-taking periods.

599 When specifically performing calibration of the detector (in out-of-data taking  
600 mode), the water in the tank was circulated to avoid top/bottom asymmetric water  
601 quality. Any non-uniformity within the tank significantly affects the PMT hit proba-

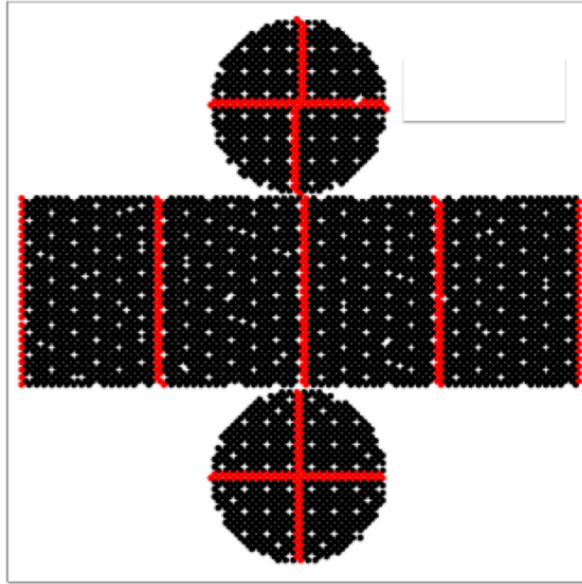


**Figure 3.2:** The location of “standard PMTs” (red) inside the SK detector. Taken from [86].

602     bility through scattering or absorption. This becomes a dominant effect for the very  
 603     low-intensity light sources discussed later which are designed such that only one  
 604     photon is incident upon a given PMT.

605       The “gain” of a PMT is defined as the ratio of the total charge of the signal produced  
 606     compared to the charge of photoelectrons emitted by the photocathodes within the  
 607     PMT. To calibrate the signal of each PMT, the “relative” and “absolute” gain values are  
 608     measured. The relative gain is the variation of gain among each of the PMTs whereas  
 609     the absolute gain is the average gain of all PMTs.

610       The relative gain is calibrated as follows. A laser is used to generate two measure-  
 611     ments: a high-intensity flash that illuminates every PMT with a sufficient number of  
 612     photons, and a low-intensity flash in which only a small number of PMTs collect light.  
 613       The first measurement creates an average charge,  $Q_{obs}(i)$  on PMT  $i$ , whereas the second  
 614     measurement ensures that each hit PMT only generates a single photoelectron. For the  
 615     low-intensity measurement, the number of times each PMT records a charge larger  
 616     than 1/4 photoelectrons,  $N_{obs}(i)$ , is counted. The values measured can be expressed as

$$\begin{aligned} Q_{obs}(i) &\propto I_H \times f(i) \times \epsilon(i) \times G(i), \\ N_{obs}(i) &\propto I_L \times f(i) \times \epsilon(i), \end{aligned} \quad (3.1)$$

617 Where  $I_H$  and  $I_L$  is the intensity of the high and low flashes,  $f(i)$  is the acceptance  
 618 efficiency of the  $i^{\text{th}}$  PMT,  $\epsilon(i)$  is the product of the quantum and collection efficiency  
 619 of the  $i^{\text{th}}$  PMT and  $G(i)$  is the gain of the  $i^{\text{th}}$  PMT. The relative gain for each PMT can  
 620 determined by taking the ratio of these quantities.

621 The absolute gain calibration is performed by observing fixed energy  $\gamma$ -rays of  
 622  $E_\gamma \sim 9\text{MeV}$  emitted isotropically from neutron capture on a NiCf source situated at  
 623 the center of the detector. This generates a photon yield of about 0.004 photoelec-  
 624 trons/PMT/event, meaning that  $> 99\%$  of PMT signals are generated from single  
 625 photoelectrons. A charge distribution is generated by performing this calibration over  
 626 all PMTs, and the average value of this distribution is taken to be the absolute gain  
 627 value.

628 As mentioned in subsection 3.1.1, the average quantum and collection efficiency  
 629 for the SK detector is  $\sim 21\%$  and  $> 70\%$  respectively. However, these values do differ  
 630 between each PMT and need to be calibrated accordingly. Consequently, the NiCf  
 631 source is also used to calibrate the “quantum  $\times$  collection” efficiency (denoted “QE”)  
 632 value of each PMT. The NiCf low-intensity source is used as the PMT hit probability  
 633 is proportional to the QE ( $N_{obs}(i) \propto \epsilon(i)$  in Equation 3.1). A Monte Carlo prediction  
 634 which includes photon absorption, scattering, and reflection is made to estimate the  
 635 number of photons incident on each PMT and the ratio of the number of predicted  
 636 to observed hits is calculated. The difference is attributed to the QE efficiency of that  
 637 PMT. This technique is extended to calculate the relative QE efficiency by normalizing  
 638 the average of all PMTs which removes the dependence on the light intensity.

639 Due to differing cable lengths and readout electronics, the timing response between  
640 a photon hitting the PMT and the signal being captured by the data acquisition can be  
641 different between each PMT. Due to threshold triggers (Described in subsection 3.1.3),  
642 the time at which a pulse reaches a threshold is dependent upon the size of the pulse.  
643 This is known as the ‘time-walk’ effect and also needs to be accounted for in each PMT.  
644 To calibrate the timing response, a pulse of light with width 0.2ns is emitted into the  
645 detector through a diffuser. Two-dimensional distributions of time and pulse height  
646 (or charge) are made for each PMT and are used to calibrate the timing response. This  
647 is performed in-situ **whilst during** data taking with the light source pulsing at 0.03Hz.

648 The top/bottom water quality asymmetry is measured using the NiCf calibration  
649 data and cross-referencing these results to the “standard PMTs”. The water attenuation  
650 length is continuously measured by the rate of vertically-downgoing cosmic-ray  
651 muons which enter via the top of the tank.

652 Dark noise is the phenomenon where a PMT registers a pulse that is consistent  
653 with a single photoelectron emitted from photon detection despite the PMT being in  
654 complete darkness. This is predominately caused by two processes. Firstly there is  
655 intrinsic dark noise which is where photoelectrons gain enough thermal energy to be  
656 emitted from the photocathode, and secondly, the radioactive decay of contaminants  
657 inside the structure of the PMT. Typical dark noise rate for PMTs used within SK are  
658  $O(3)$ kHz [87] **which equates to about 12 dark noise hits per 220ns**. This is lower than  
659 the expected number of photons generated for a ‘high energy event’ (As described in  
660 subsection 3.1.4) but instability in this value can cause biases in reconstruction. Dark  
661 noise is related to the gain of a PMT and is calibrated using hits inside a time window  
662 recorded before an event trigger [98].

### <sup>663</sup> 3.1.3 Data Acquisition and Triggering

<sup>664</sup> The analysis presented in this thesis only uses the SK-IV period of the SK experiment  
<sup>665</sup> so this subsection focuses on the relevant points of the data acquisition and triggering  
<sup>666</sup> systems to that SK period. The earlier data acquisition and triggering systems are  
<sup>667</sup> documented in [99, 100].

<sup>668</sup> Before the SK-IV period started, the existing front-end electronics were replaced  
<sup>669</sup> with “QTC-Based Electrons with Ethernet, QBEE” systems [101]. When the QBEE  
<sup>670</sup> observes a signal above a 1/4 photoelectron threshold, the charge-to-time (QTC)  
<sup>671</sup> converter generates a rectangular pulse. The start of the rectangular pulse indicates  
<sup>672</sup> the time at which the analog photoelectron signal was received and the width of the  
<sup>673</sup> pulse indicates the total charge integrated throughout the signal. This is then digitized  
<sup>674</sup> by time-to-digital converters and sent to the “front-end” PCs. The digitized signal  
<sup>675</sup> from every QBEE is then chronologically ordered and sent to the “merger” PCs. It is  
<sup>676</sup> the merger PCs that apply the software trigger. Any triggered events are passed to the  
<sup>677</sup> “organizer” PC. This sorts the data stream of multiple merger PCs into chronologically  
<sup>678</sup> ordered events which are then saved to disk. The schematic of data flow from PMTs to  
<sup>679</sup> disk is illustrated in Figure 3.3.

<sup>680</sup> The software trigger (described in [103]) operates by determining the number of  
<sup>681</sup> PMT hits within a 200ns sliding window,  $N_{200\text{-}}$ . **This window** coincides with the  
<sup>682</sup> maximum time that a Cherenkov photon would take to traverse the length of the SK  
<sup>683</sup> tank [100]. For lower energy events that generate fewer photons, this technique is  
<sup>684</sup> useful for eliminating background processes like dark noise and radioactive decay  
<sup>685</sup> which would be expected to separate in time. When the value of  $N_{200}$  exceeds some  
<sup>686</sup> threshold, a software trigger is issued. There are several trigger thresholds used within  
<sup>687</sup> the SK-IV period which are detailed in Table 3.2. If one of these thresholds is met, the

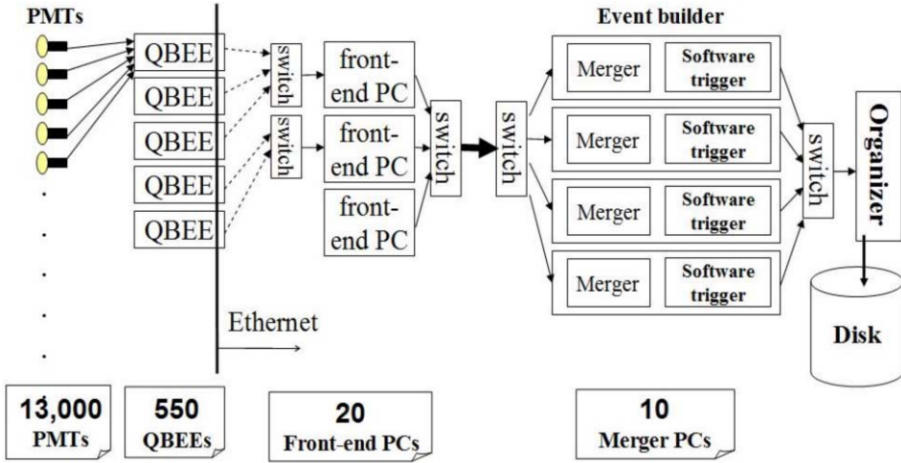


**Figure 3.3:** Schematic view of the data flow through the data acquisition and online system. Taken from [102].

688 PMT hits within an extended time window are also read out and saved to disk. In  
 689 the special case of an event that exceeds the SHE trigger but does not exceed the OD  
 690 trigger, the AFT trigger looks for delayed coincidences of 2.2MeV gamma rays emitted  
 691 from neutron capture in a  $535\mu\text{s}$  window after the SHE trigger. A similar but more  
 692 complex “Wideband Intelligent Trigger (WIT)” has been deployed and is described  
 693 in [104].

Trigger	Acronym	Condition	Extended time window ( $\mu\text{s}$ )
Super Low Energy	SLE	>34/31 hits	1.3
Low Energy	LE	>47 hits	40
High Energy	HE	>50 hits	40
Super High Energy	SHE	>70/58 hits	40
Outer Detector	OD	>22 hits in OD	N/A

**Table 3.2:** The trigger thresholds and extended time windows saved around an event which were utilised throughout the SK-IV period. The exact thresholds can change and the values listed here represent the thresholds at the start and end of the SK-IV period.

### <sup>694</sup> 3.1.4 Cherenkov Radiation

- <sup>695</sup> Cherenkov light is emitted from any highly energetic charged particle traveling  
<sup>696</sup> with relativistic velocity,  $\beta$ , greater than the local speed of light in a medium [105].  
<sup>697</sup> Cherenkov light is formed at the surface of a cone with characteristic pitch angle,

$$\cos(\theta) = \frac{1}{\beta n}. \quad (3.2)$$

<sup>698</sup> where  $n$  is the refractive index of the medium. Consequently, the Cherenkov  
<sup>699</sup> momentum threshold,  $P_{thres}$ , is dependent upon the mass,  $m$ , of the charged particle  
<sup>700</sup> moving through the **media medium**,

$$P_{thres} = \frac{m}{\sqrt{n^2 - 1}} \quad (3.3)$$

<sup>701</sup> For water, where  $n = 1.33$ , the Cherenkov threshold momentum and energy for  
<sup>702</sup> various particles are given in Table 3.3. In contrast,  $\gamma$ -rays are detected indirectly via  
<sup>703</sup> the combination of photons generated by Compton scattering and pair production.  
<sup>704</sup> The threshold for detection in the SK detector is typically higher than the threshold  
<sup>705</sup> for photon production. This is due to the fact that the attenuation of photons in the  
<sup>706</sup> water means that typically  $\sim 75\%$  of Cherenkov photons reach the ID PMTs. Then the  
<sup>707</sup> collection and quantum efficiencies described in subsection 3.1.1 result in the number  
<sup>708</sup> of detected photons being lower than the number of photons which reach the PMTs.

Particle	Threshold Momentum (MeV)	Threshold Energy (MeV)
Electron	0.5828	0.7751
Muon	120.5	160.3
Pion	159.2	211.7
Proton	1070.0	1423.1

**Table 3.3:** The threshold momentum and energy for a particle to generate Cherenkov light in ultrapure water, as calculated in Equation 3.2 in ultrapure water which has refractive index  $n = 1.33$ .

The Frank-Tamm equation [106] describes the relationship between the number of

Cherenkov photons generated per unit length,  $dN/dx$ , the wavelength of the photons

generated,  $\lambda$ , and the relativistic velocity of the charged particle,

$$\frac{d^2N}{dx d\lambda} = 2\pi\alpha \left(1 - \frac{1}{n^2\beta^2}\right) \frac{1}{\lambda^2}. \quad (3.4)$$

where  $\alpha$  is the fine structure constant. For a 100MeV momentum electron, approx-

imately 330 photons will be produced per centimeter in the  $300\text{nm} \leq \lambda \leq 700\text{nm}$

region which the ID PMTs are most sensitive to [87].

## 3.2 The Tokai to Kamioka Experiment

The Tokai to Kamioka (T2K) experiment is a long-baseline neutrino oscillation exper-

iment located in Japan. Proposed in the early 2000s [107, 108] to replace K2K [109],

T2K was designed to observe electron neutrino appearance whilst precisely measuring

the oscillation parameters associated with muon neutrino disappearance [110]. The

experiment consists of a neutrino beam generated at the Japan Proton Accelerator

Research Complex (J-PARC), a suite of near detectors situated 280m from the beam

<sup>722</sup> target, and the Super Kamiokande far detector positioned at a 295km baseline. The  
<sup>723</sup> cross-section view of the T2K experiment is drawn in Figure 3.4.

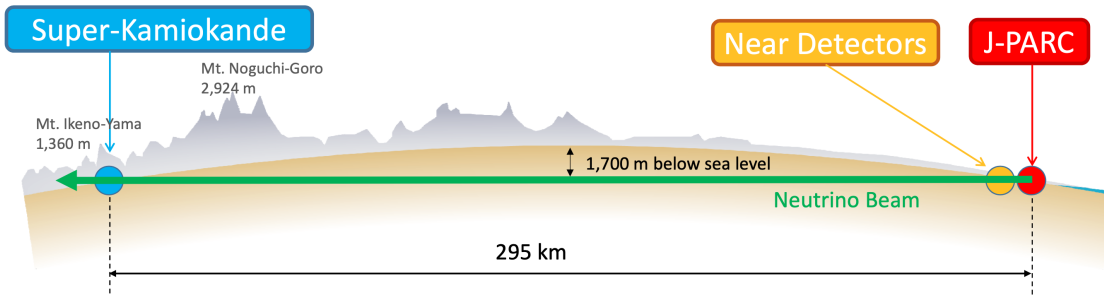


**Figure 3.4:** The cross-section view of the Tokai to Kamioka experiment illustrating the beam generation facility at J-PARC, the near detector situated at a baseline of 280m and the Super Kamiokande far detector situated 295km from the beam target.

<sup>724</sup> The T2K collaboration makes world-leading measurements of the  $\sin^2(\theta_{23})$ ,  $\Delta m_{23}^2$ ,  
<sup>725</sup> and  $\delta_{CP}$  oscillation parameters. Improvements in the precision and accuracy of param-  
<sup>726</sup> eter estimates are still being made by including new data samples and developing the  
<sup>727</sup> models which describe the neutrino interactions and detector responses [111]. Electron  
<sup>728</sup> neutrino appearance was first observed at T2K in 2014 [112] ~~which accompanied a~~  
<sup>729</sup> **7.3 $\sigma$  significance of a non-zero  $\sin^2(\theta_{13})$  measurement with 7.3 $\sigma$  significance.**

<sup>730</sup> The near detectors provide constraints on the beam flux and cross-section model  
<sup>731</sup> parameters used within the **fit oscillation analysis** by observing the unoscillated  
<sup>732</sup> neutrino beam. There are a host of detectors situated in the near detector hall (As  
<sup>733</sup> illustrated in Figure 3.5): ND280 (subsection 3.2.2), INGRID (subsection 3.2.3), NINJA  
<sup>734</sup> [113], WAGASCI [114], and Baby-MIND [115]. The latter three are not currently used  
<sup>735</sup> within the oscillation analysis presented within this thesis.

<sup>736</sup> Whilst this thesis presents the ND280 in terms of its purpose for the oscillation  
<sup>737</sup> analysis, the detector can also make many cross-section measurements at neutrino  
<sup>738</sup> energies of  $O(1)$ GeV for the different targets within the detector [116, 117]. These  
<sup>739</sup> measurements are of equal importance as they can lead the way in determining the

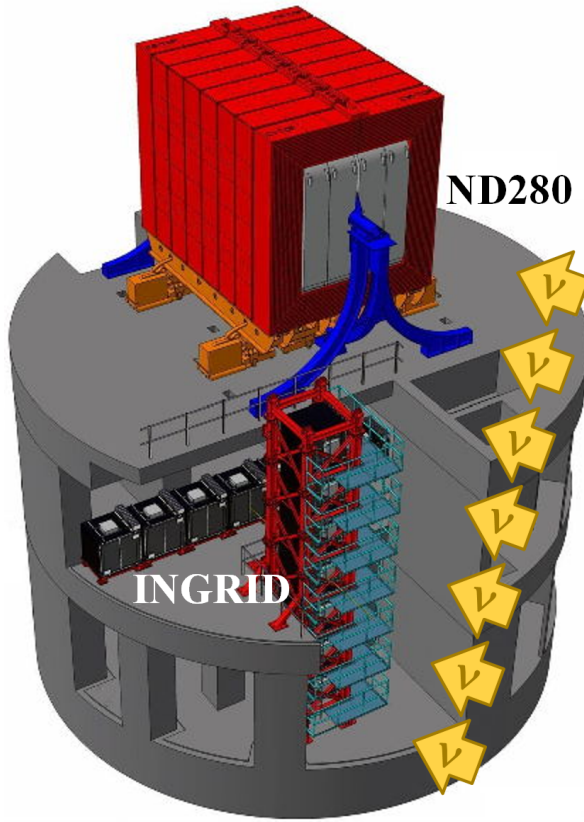


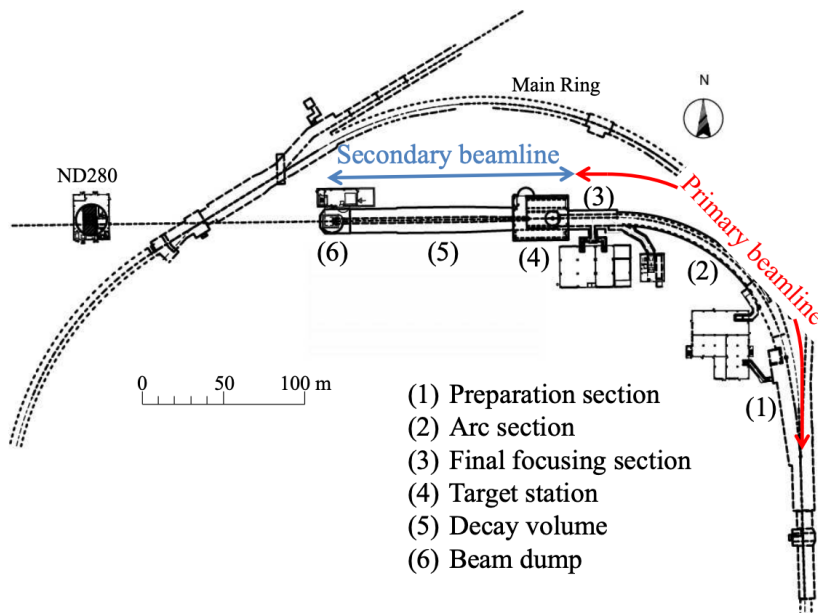
**Figure 3.5:** The near detector suite for the T2K experiment showing the ND280 and INGRID detectors. The distance between the detectors and the beam target is 280m.

<sup>740</sup> model parameters used in the interaction models for the future high-precision era of  
<sup>741</sup> neutrino physics.

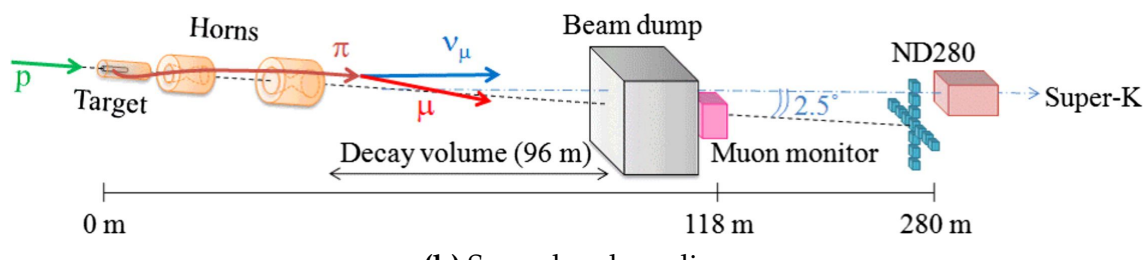
### <sup>742</sup> 3.2.1 The Neutrino Beam

<sup>743</sup> The neutrino beam used within the T2K experiment is described in [59, 118] and  
<sup>744</sup> summarised below. The accelerating facility at J-PARC is composed of two sections; the  
<sup>745</sup> primary and secondary beamlines. Figure 3.6 illustrates a schematic of the beamline,  
<sup>746</sup> focusing mostly on the components of the secondary beamline. The primary beamline  
<sup>747</sup> has three accelerators that progressively accelerate protons; a linear accelerator, a rapid-  
<sup>748</sup> cycling synchrotron, and the main-ring (MR) synchrotron. Once fully accelerated by  
<sup>749</sup> the MR, the protons have a kinetic energy of 30GeV. Eight bunches of these protons,

separated by 500ns, are extracted per “spill” from the MR and directed towards a graphite target (a rod of length 91.4cm and diameter 2.6cm). Spills are extracted at 0.5Hz with  $\sim 3 \times 10^{14}$  protons contained per spill.



(a) Primary and secondary beamline

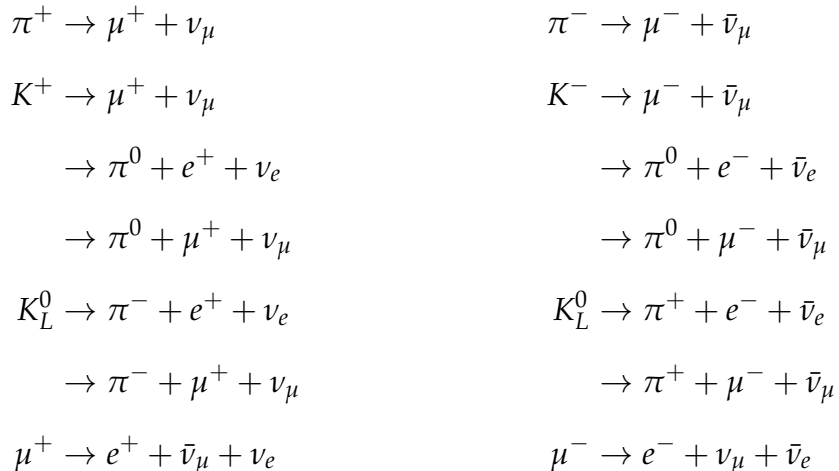


(b) Secondary beamline

**Figure 3.6:** Top panel: Bird's eye view of the most relevant part of primary and secondary beamline used within the T2K experiment. The primary beamline is the main-ring proton synchrotron, kicker magnet, and graphite target. The secondary beamline consists of the three focusing horns, decay volume, and beam dump. Figure taken from [118]. Bottom panel: The side-view of the secondary beamline including the focusing horns, beam dump and neutrino detectors. Figure taken from [119].

The secondary beamline consists of three main components: the target station, the decay volume, and the beam dump. The target station is comprised of the target, beam monitors, and three magnetic focusing horns. The proton beam interacts with the

<sup>756</sup> graphite target to form a secondary beam of mostly pions and kaons. The secondary  
<sup>757</sup> beam travels through a 96m long decay volume, generating neutrinos through the  
<sup>758</sup> following decays [59],



<sup>760</sup> The electrically charged component of the secondary beam is focused towards the  
<sup>761</sup> far detector by the three magnetic horns. These horns direct charged particles of a  
<sup>762</sup> particular polarity towards SK whilst defocusing the oppositely charged particles.  
<sup>763</sup> This allows a mostly neutrino or mostly antineutrino beam to be used within the  
<sup>764</sup> experiment, denoted as “forward horn current (FHC)” or “reverse horn current (RHC)”  
<sup>765</sup> respectively.

<sup>766</sup> Figure 3.7 illustrates the different contributions to the FHC and RHC neutrino flux.  
<sup>767</sup> The low energy flux is dominated by the decay of pions whereas kaon decay becomes  
<sup>768</sup> the dominant source of neutrinos for  $E_\nu > 3\text{GeV}$ . The “wrong-sign” component,  
<sup>769</sup> which is the  $\bar{\nu}_\mu$  background in a  $\nu_\mu$  beam, and the intrinsic irreducible  $\nu_e$  background,  
<sup>770</sup> are predominantly due to muon decay for  $E_\nu < 2\text{GeV}$ . As the antineutrino **production**  
<sup>771</sup> cross-section is smaller than the neutrino cross-section, the wrong-sign component is  
<sup>772</sup> more dominant in the RHC beam as compared to that in the FHC beam.

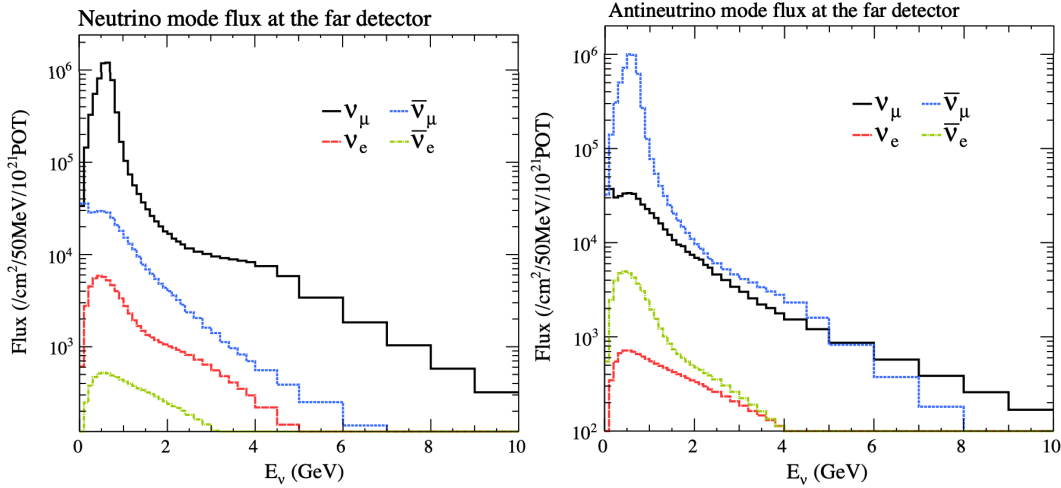


**Figure 3.7:** The Monte Carlo prediction of the energy spectrum for each flavour of neutrino ( $\nu_e$ ,  $\bar{\nu}_e$ ,  $\nu_\mu$  and  $\bar{\nu}_\mu$ ) in the neutrino dominated beam FHC mode (Left) and antineutrino dominated beam RHC mode (Right) expected at SK. Taken from [120].

The beam dump, situated at the end of the decay volume, stops all charged particles

other than highly energetic muons ( $p_\mu > 5\text{GeV}$ ). The MuMon detector monitors the penetrating muons to determine the beam direction and intensity which is used to constrain some of the beam flux systematics within the analysis [119, 121].

The T2K experiment uses an off-axis beam to narrow the neutrino energy distribution.

This was the first implementation of this technique in a long-baseline neutrino oscillation experiment after its original proposal [122]. Pion decay,  $\pi \rightarrow \mu + \nu_\mu$ , is a two-body decay. Consequently, the neutrino energy,  $E_\nu$ , can be determined based on the pion energy,  $E_\pi$ , and the angle at which the neutrino is emitted,  $\theta$ ,

$$E_\nu = \frac{m_\pi^2 - m_\mu^2}{2(E_\pi - p_\pi \cos(\theta))}, \quad (3.5)$$

where  $m_\pi$  and  $m_\mu$  are the mass of the pion and muon respectively. For a fixed

energy pion, the neutrino energy distribution is dependent upon the angle at which the neutrinos are observed from the initial pion beam direction. For the 295km baseline at

<sup>785</sup> T2K,  $E_\nu = 0.6\text{GeV}$  maximises the electron neutrino appearance probability,  $P(\nu_\mu \rightarrow \nu_e)$ ,  
<sup>786</sup> whilst minimising the muon disappearance probability,  $P(\nu_\mu \rightarrow \nu_\mu)$ . Figure 3.8  
<sup>787</sup> illustrates the neutrino energy distribution for a range of off-axis angles, as well as the  
<sup>788</sup> oscillation probabilities most relevant to T2K.

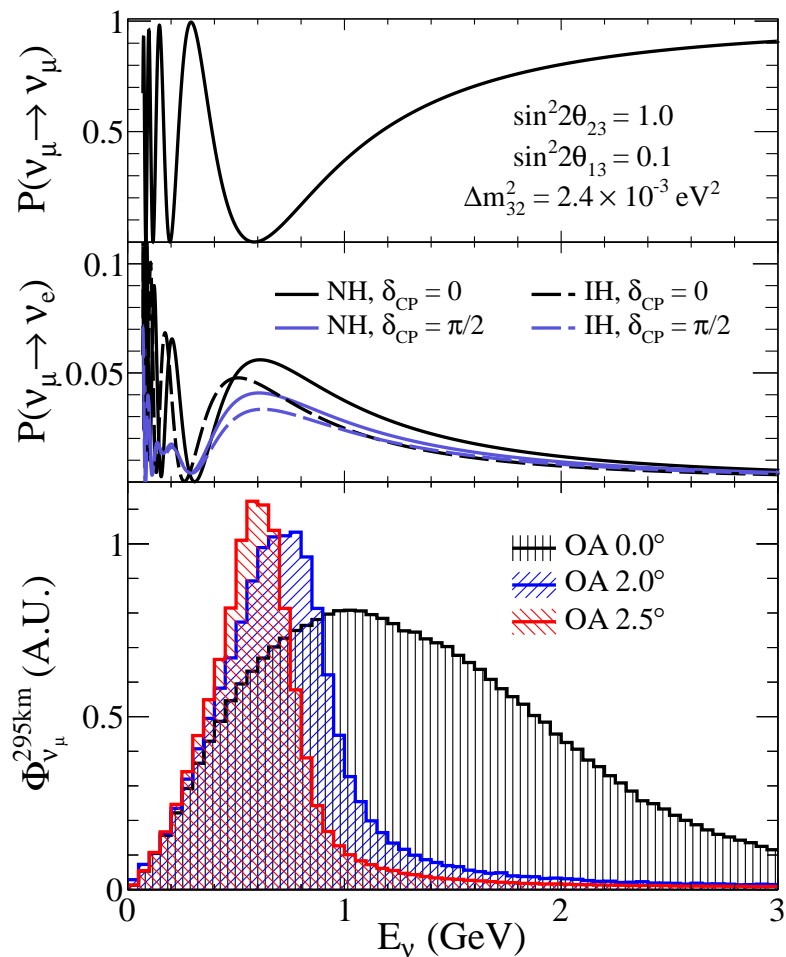


**Figure 3.8:** Top panel: T2K muon neutrino disappearance probability as a function of neutrino energy. Middle panel: T2K electron neutrino appearance probability as a function of neutrino energy. Bottom panel: The neutrino flux distribution for three different off-axis angles (Arbitrary units) as a function of neutrino energy.

### <sup>789</sup> 3.2.2 The Near Detector at 280m

<sup>790</sup> Whilst all the near detectors are situated in the same “pit” located at 280m from the  
<sup>791</sup> beamline, the “ND280” detector is the off-axis detector which is situated at the same

<sup>792</sup> off-axis angle as the Super-Kamiokande far detector. It has two primary functions;  
<sup>793</sup> firstly it measures the neutrino flux and secondly it counts the event rates of different  
<sup>794</sup> types of neutrino interactions. Both of these constrain the flux and cross-section  
<sup>795</sup> systematics invoked within the model for a more accurate prediction of the expected  
<sup>796</sup> event rate at the far detector.

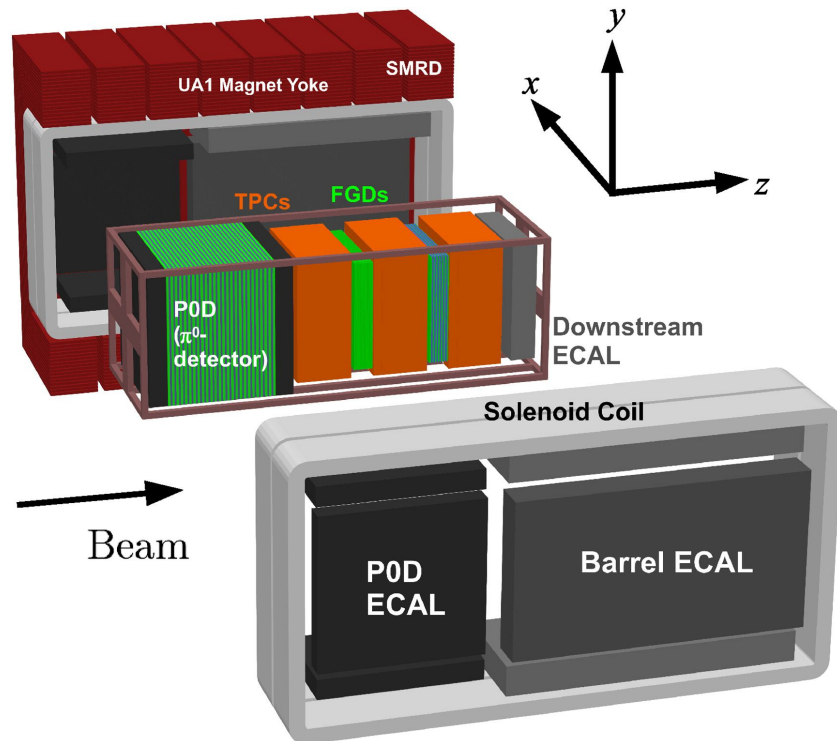


**Figure 3.9:** The components of the ND280 detector. The neutrino beam travels from left to right. Taken from [118].

<sup>797</sup> As illustrated in Figure 3.9, the ND280 detector consists of several sub-detectors.  
<sup>798</sup> The most important part of the detector for this analysis is the tracker region. This is  
<sup>799</sup> comprised of two time projection chambers (TPCs) sandwiched between three fine  
<sup>800</sup> grain detectors (FGDs). The FGDs contain both hydrocarbon plastics and water tar-  
<sup>801</sup> gets for neutrino interactions and provide track reconstruction near the interaction  
<sup>802</sup> vertex. The emitted charged particles can then propagate into the TPCs which pro-  
<sup>803</sup> vide particle identification and momentum reconstruction. The FGDs and TPCs are  
<sup>804</sup> further described in subsubsection 3.2.2.1 and subsubsection 3.2.2.2 respectively. The

805 electromagnetic calorimeter (ECAL) encapsulates the tracker region alongside the  $\pi^0$   
806 detector (P0D). The ECAL measures the deposited energy from photons emitted from  
807 interactions within the FGD. The P0D constrains the cross-section of neutral current  
808 interactions which generate neutral pions, which is one of the largest backgrounds in  
809 the electron neutrino appearance oscillation channel. The P0D and ECAL detectors  
810 are detailed in subsubsection 3.2.2.3 and subsubsection 3.2.2.4 respectively. The entire  
811 detector is located within a large **yolk yoke** magnet which produces a 0.2T magnetic  
812 field. This design of the magnet also includes a scintillating detector called the side  
813 muon range detector (SMRD) which is used to track high-angle muons as well as  
814 acting as a cosmic veto. The SMRD is described in subsubsection 3.2.2.5.

### 815 3.2.2.1 Fine Grained Detectors

816 The T2K tracker region is comprised of two fine grained detectors (FGD) and three  
817 Time Projection Chambers (TPC). A detailed description of the FGD design, construc-  
818 tion, and assembly is found in [123] and summarised below. The FGDs are the primary  
819 target for neutrino interactions with a mass of 1.1 tonnes per FGD. Alongside this,  
820 the FGDs are designed to be able to track short-range particles which do not exit the  
821 FGD. Typically, short-range particles are low momentum and are observed as tracks  
822 that deposit a large amount of energy per unit length. This means the FGD needs  
823 good granularity to resolve these particles. The FGDs have the best timing resolution  
824 ( $\sim 3\text{ns}$ ) of any of the sub-detectors of the ND280 detector. As such, the FGDs are used  
825 for time of flight measurements to **determine distinguish** forward going positively  
826 charged particles from backward going negatively charged particles. Finally, any  
827 tracks which pass through multiple sub-detectors are required to be track matched to  
828 the FGD.

Both FGDs are made from square scintillator planes of side length 186cm and width 2.02cm. Each plane consists of two layers of 192 scintillator bars in an X or Y orientation. A wavelength shifting fiber is threaded through the center of each bar and is read out by a multi-pixel photon counter (MPPC). FGD1 is the most upstream of the two FGDs and contains 15 planes of carbon plastic scintillator which is a common target in external neutrino scattering data. As the far detector is a pure water target, 7 of the 15 scintillator planes in FGD2 have been replaced with a hybrid water-scintillator target. Due to the complexity of the nucleus, nuclear effects can not be extrapolated between different nuclei. Therefore having the ability to take data on one target which is the same as external data and another target which is the same as the far detector target is beneficial for reliable model parameter estimates.

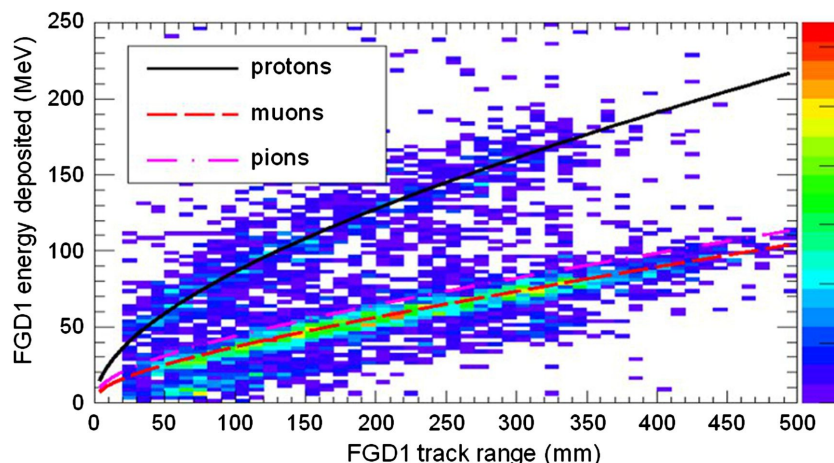


**Figure 3.10:** Comparison of data to Monte Carlo prediction of integrated deposited energy as a function of track length for particles that stopped in FGD1. Taken from [123].

The integrated deposited energy is used for particle identification. The FGD can distinguish protons from other charged particles by comparing the integrated deposited energy from data to Monte Carlo prediction as seen in Figure 3.10.

<sup>843</sup> **3.2.2.2 Time Projection Chambers**

<sup>844</sup> The majority of particle identification and momentum measurements within ND280  
<sup>845</sup> are provided by three Time Projection Chambers (TPCs) [124]. The TPCs are located  
<sup>846</sup> on either side of the FGDs. They are located inside of the magnetic field meaning the  
<sup>847</sup> momentum of a charged particle can be determined from the bending of the track.

<sup>848</sup> Each TPC module consists of two gas-tight boxes, as shown in Figure 3.11, which  
<sup>849</sup> are made of non-magnetic material. The outer box is filled with CO<sub>2</sub> which acts as  
<sup>850</sup> an electrical insulator between the inner box and the ground. The inner box forms  
<sup>851</sup> the field cage which produces a uniform electric drift field of  $\sim 275\text{V/cm}$  and **is filled**  
<sup>852</sup> **with** an argon gas mixture. Charged particles moving through this gas mixture ionize  
<sup>853</sup> the gas **mixture**. The and the ionised charge is drifted towards micromegas detectors  
<sup>854</sup> which measure the ionization charge. The time and position information in the readout  
<sup>855</sup> allows a three-dimensional image of the neutrino interaction.

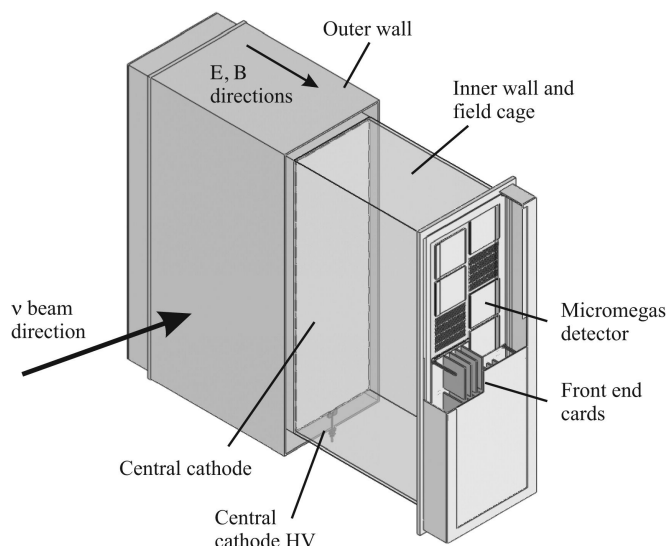


**Figure 3.11:** Schematic design of a Time Projection Chamber detector. Taken from [124].

<sup>856</sup> The particle identification of tracks that pass through the TPCs is performed using  
<sup>857</sup> dE/dx measurements. Figure 3.12 illustrates the data to Monte Carlo distributions

858 of the energy lost by a charged particle passing through the TPC as a function of the  
 859 reconstructed particle momentum. The resolution is  $7.8 \pm 0.2\%$  meaning that electrons  
 860 and muons can be distinguished. This allows reliable measurements of the intrinsic  $\nu_e$   
 861 component of the beam.

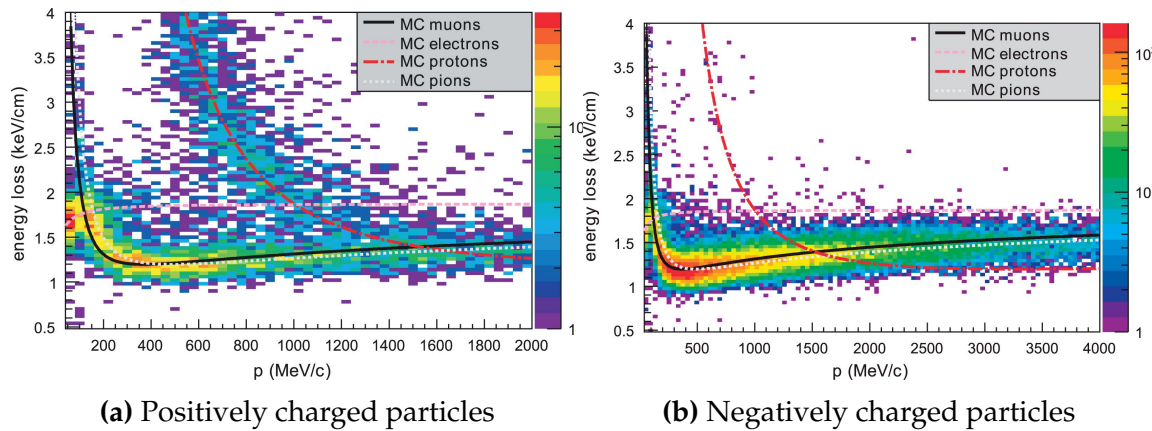


Figure 3.12: The distribution of energy loss as a function of reconstructed momentum for charged particles passing through the TPC, comparing data to Monte Carlo prediction. Taken from [124].

### 862 3.2.2.3 $\pi^0$ Detector

863 If one of the  $\gamma$ -rays from a  $\pi^0 \rightarrow 2\gamma$  decay is missed at the far detector, the reconstruc-  
 864 tion will determine that event to be **electron-like a charge current  $\nu_e$ -like event**. This  
 865 is one of the main backgrounds hindering the electron neutrino appearance searches.  
 866 **Therefore, the The**  $\pi^0$  detector (P0D) measures the cross-section of the neutral current  
 867 induced neutral pion production on a water target **to constrain this background**.

868 The P0D is a cube of approximately 2.5m length **.The P0D consists consisting**  
 869 of layers of scintillating bars, brass and lead sheets, and water bags as illustrated in  
 870 Figure 3.13. Two electromagnetic calorimeters are positioned at the most upstream  
 871 and most downstream position in the sub-detector and the water target is situated in  
 872 between them. The scintillator layers are built from two triangular bars orientated  
 873 in opposite directions to form a rectangular layer. Each triangular scintillator bar is

<sup>874</sup> threaded with optical fiber which is read out by MPPCs. The high-Z brass and lead  
<sup>875</sup> regions produce electron showers from the photons emitted in  $\pi^0$  decay.

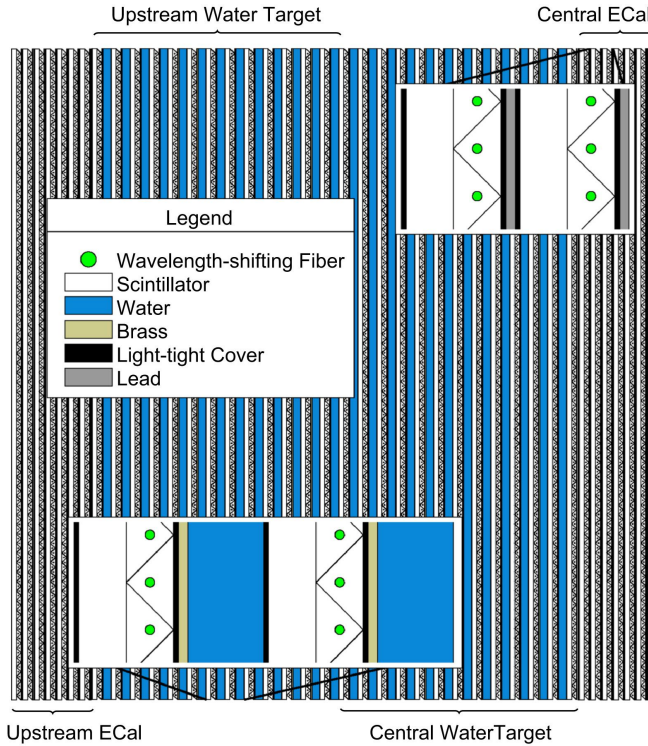


**Figure 3.13:** A schematic of the P0D side-view. Taken from [125].

<sup>876</sup> The sub-detector can generate measurements of NC1 $\pi^0$  cross-sections on a water  
<sup>877</sup> target by measuring the event rate both with and without the water target, with the  
<sup>878</sup> cross-section on a water target being determined as the difference. The total active  
<sup>879</sup> mass is 16.1 tonnes when filled with water and 13.3 tonnes when empty.

#### <sup>880</sup> 3.2.2.4 Electromagnetic Calorimeter

<sup>881</sup> The electromagnetic calorimeter [126] (ECal) encapsulates the P0D and tracking sub-  
<sup>882</sup> detectors. Its primary purpose is to aid  $\pi^0$  reconstruction from any interaction in  
<sup>883</sup> the tracker. To do this, it measures the energy and direction of photon showers from  
<sup>884</sup>  $\pi^0 \rightarrow 2\gamma$  decay. It can also distinguish pion and muon tracks depending on the shape  
<sup>885</sup> of the photon shower deposited.

886        The ECal is comprised of three sections; the P0D ECal which surrounds the P0D,  
887        the barrel ECal which encompasses the tracking region, and the downstream ECal  
888        which is situated downstream of the tracker region. The barrel and downstream  
889        ECals are tracking calorimeters that focus on electromagnetic showers from high-angle  
890        particles emitted from the tracking sub-detectors. Particularly in the TPC, high-angle  
891        tracks (those which travel perpendicularly to the beam-axis) can travel along a single  
892        scintillator bar resulting in very few hits. The width of the barrel and downstream  
893        ECal corresponds to  $\sim 11$  electron radiation lengths to ensure ~~~50% of the energy~~  
894        ~~of the  $\pi^0$  is contained a significant amount of the  $\pi^0$  energy is contained~~. As the  
895        P0D has its own calorimetry which reconstructs showers, the P0D ECal determines  
896        the energy which escapes the P0D.

897        Each ECal is constructed of multiple layers of scintillating bars sandwiched between  
898        lead sheets. The scintillating bars are threaded with optical fiber and read out by  
899        MPPCs. Each sequential layer of the scintillator is orientated perpendicular to the  
900        previous which allows a ~~two-dimensional readout, which when temporal, information is included results in three-dimension event displays three dimensional event displays~~. The target mass of the P0D ECal, barrel ECal, and downstream ECal are 1.50,  
901        4.80 and 6.62 tonnes respectively.

### 904      3.2.2.5 Side Muon Range Detector

905        As illustrated in Figure 3.9, the ECal, FGDs, P0D, and TPCs are enclosed within the  
906        UA1 magnet. Originally designed for the NOMAD [127] experiment and reconditioned  
907        for use in the T2K experiment [128], the UA1 magnet provides a uniform horizontal  
908        magnetic field of ~~0.2 ± 2 × 10<sup>-4</sup>T~~ 0.2T with an uncertainty of  $2 \times 10^{-4}$ T.

909     Built into the UA1 magnet, the side muon range detector (SMRD) [129] monitors  
910    high-energy muons which leave the tracking region and permeate through the ECal.  
911    It additionally acts as a cosmic muon veto and trigger.

912    **3.2.3 The Interactive Neutrino GRID**

913    The Interactive Neutrino GRID (INGRID) detector is situated within the same “pit” as  
914    the other near detectors. It is aligned with the beam in the “on-axis” position and mea-  
915    sures the beam direction, spread, and intensity. The detector was originally designed  
916    with 16 identical modules [118] (two modules have since been decommissioned) and a  
917    “proton” module. The design of the detector is cross-shaped with length and height  
918    10m × 10m as illustrated in Figure 3.14.

919    Each module is composed of iron sheets interlaced with eleven tracking scintillator  
920    planes for a total target mass of 7.1 tonnes per module. The scintillator design is an X-Y  
921    pattern of 24 bars in both orientations, where each bar contains wave-length shifting  
922    fibers which are connected to multi-pixel photon counters (MPPCs). ~~The MPPCs con-~~  
923 ~~vert detected photons into electrical signals via photodiodes. This is then read out~~  
924 ~~by Trip-T front-end electronics and passed to the readout merging modules along~~  
925 ~~with timing information from the clock module.~~ Each module is encapsulated inside  
926    veto planes to aid the rejection of charged particles entering the module.

927    The proton module is different from the other modules in that it consists of entirely  
928    scintillator planes with no iron target. The scintillator bars are also smaller than those  
929    used in the other modules to increase the granularity of the detector and improve  
930    tracking capabilities. The module sits in the center of the beamline and is designed to  
931    give precise measurements of quasi-elastic charged current interactions to evaluate  
932    the performance of the Monte Carlo simulation of the beamline.

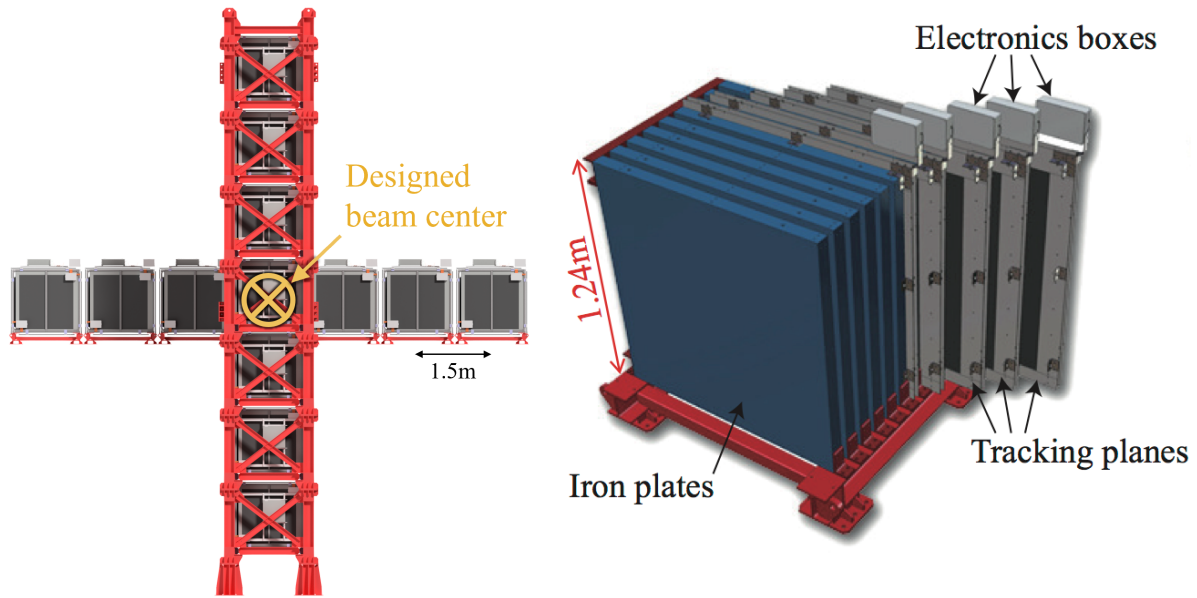


**Figure 3.14:** Left panel: The Interactive Neutrino GRID on-axis Detector. 14 modules are arranged in a cross-shape configuration, with the center modules being directly aligned with the on-axis beam. Right panel: The layout of a single module of the INGRID detector. Both figures are recreated from [118].

933        The INGRID detector can measure the beam direction to an uncertainty of 0.4mrad

934        and the beam center within a resolution of 10cm [118]. The beam direction in both the

935        vertical and horizontal directions is discussed in [130] and it is found to be in good

936        agreement with the MUMON monitor described in subsection 3.2.1.

<sub>937</sub> **Chapter 4**

<sub>938</sub> **Bayesian Statistics and Markov Chain  
Monte Carlo Techniques**

<sub>940</sub> ~~The analysis throughout this thesis is based upon~~ This thesis presents a Bayesian  
<sub>941</sub> oscillation analysis. To extract the oscillation parameters, a Markov Chain Monte  
<sub>942</sub> Carlo (MCMC) method is used. This chapter explains the theory of how parameter  
<sub>943</sub> estimates can be determined using this technique and condenses the material found in  
<sub>944</sub> the literature [131–134].

<sub>945</sub> The oscillation parameter determination presented within this thesis is built upon  
<sub>946</sub> a ~~a simultaneous fit to the near detector, far detector beam, and atmospheric neutrino data~~  
<sub>947</sub> ~~a simultaneous fit to neutrino beam data in the near detector, beam data~~  
<sub>948</sub> ~~at SK and atmospheric data at SK~~. In total, there are four oscillation parameters of  
<sub>949</sub> interest ( $\sin^2(\theta_{23})$ ,  $\sin^2(\theta_{13})$ ,  $\Delta m_{23}^2$ , and  $\delta_{CP}$ ), two oscillation parameters to which  
<sub>950</sub> this study will not be sensitive ( $\sin^2(\theta_{12})$ ,  $\Delta m_{12}^2$ ) and many nuisance parameters  
<sub>951</sub> that control the systematic uncertainty models invoked within this study. ~~The systematic~~  
<sub>952</sub> ~~uncertainties can be grouped into categories depending on how they are~~  
<sub>953</sub> ~~defined: 574 bin-normalisations due to the near detector response, 45 bin-normali-~~  
<sub>954</sub> ~~sations to describe the far detector response to neutrino beam events, 27 parameters~~  
<sub>955</sub> ~~to describe the detector response to atmospheric neutrino events, 100 to model the~~  
<sub>956</sub> ~~bin-normalisation due to beam flux uncertainties, 18 which model the atmospheric~~  
<sub>957</sub> ~~flux uncertainties, and 87 to describe the correlated cross-section model. An alter-~~  
<sub>958</sub> ~~native parameterisation, where the far detector response is correlated between the~~

959 ~~beam and atmospheric samples, replaces the bin normalisation parameters with~~  
 960 ~~224 shift and smear systematics. Section Link to Systematics Chapter describes the~~  
 961 ~~systematic model in more depth.~~

962 The MCMC technique generates a multi-dimensional probability distribution across  
 963 all of the model parameters used in the fit. To determine the parameter estimate of a  
 964 single parameter, this multi-dimensional object is integrated over all other parameters.  
 965 This process is called Marginalisation and is further described in subsection 4.3.1.  
 966 Monte Carlo techniques approximate the probability distribution of each parameter  
 967 within the limit of generating infinite samples. As ever, generating a large number of  
 968 samples is time and resource-dependent. Therefore, an MCMC technique is utilised  
 969 within this analysis to reduce the required number of steps to sufficiently sample the  
 970 parameter space. This technique is described in further detail in subsection 4.2.1.

## 971 4.1 Bayesian Statistics

972 ~~According to Bayesian Inference, observables and parameters of a statistical model~~  
 973 ~~are treated on an equal footing. To estimate model parameters  $\vec{\theta}$  from some data~~  
 974  ~~$D$ , one needs to define the joint probability distribution  $P(D|\vec{\theta})$  which Bayesian~~  
 975 ~~inference treats observable data,  $D$ , and model parameters,  $\vec{\theta}$ , on equal footing such~~  
 976 ~~that a probability model of both data and parameters is required. This is the joint~~  
 977 ~~probability distribution  $P(D, \vec{\theta})$  and~~ can be described ~~as by~~ the prior distribution for  
 978 model parameters  $P(\vec{\theta})$  and the likelihood of the data given the model parameters  
 979  $P(D|\vec{\theta})$ ,

$$P(D, \vec{\theta}) = P(D|\vec{\theta})P(\vec{\theta}). \quad (4.1)$$

980     The prior distribution,  $P(\vec{\theta})$ , describes all previous knowledge about the parameters  
 981    within the model. For example, if the risk of developing health problems is known  
 982    to increase with age, the prior distribution would describe the increase. For the  
 983    purpose of this analysis, the prior distribution is typically the best-fit values taken  
 984    from external data measurements with a Gaussian uncertainty. The prior distribution  
 985    can also contain correlations between model parameters. In an analysis using Monte  
 986    Carlo techniques, the likelihood of measuring some data assuming some set of model  
 987    parameters is calculated by comparing the Monte Carlo prediction generated at that  
 988    particular set of model parameters to the data.

989     It is parameter estimation that is important for this analysis and as such, we apply  
 990    Bayes' theorem [135] to calculate the probability for each parameter to have a certain  
 991    value given the observed data,  $P(\vec{\theta}|D)$ , which is known as the posterior distribution  
 992    (often termed the posterior). This can be expressed as

$$P(\vec{\theta}|D) = \frac{P(D|\vec{\theta})P(\vec{\theta})}{\int P(D|\vec{\theta})P(\vec{\theta})d\vec{\theta}}. \quad (4.2)$$

993     The denominator in Equation 4.2 is the integral of the joint probability distribution  
 994    over all values of all parameters used within the fit. For brevity, we say that the  
 995    posterior distribution is

$$P(\vec{\theta}|D) \propto P(D|\vec{\theta})P(\vec{\theta}). \quad (4.3)$$

996     In subsection 4.3.1, we see that for the cases used within this analysis, it is reason-  
 997    able to know the posterior to some normalisation constant.

## 998 4.2 Monte Carlo Simulation

999 Monte Carlo techniques are used to numerically solve a complex problem that does  
1000 not necessarily have an analytical solution. These techniques rely on building a large  
1001 ensemble of samples from an unknown distribution and then using the ensemble to  
1002 approximate the properties of the distribution.

1003 An example that uses Monte Carlo techniques is to calculate the area underneath  
1004 a curve. For example, take the problem of calculating the area under a straight line  
1005 with gradient  $M = 0.4$  and intercept  $C = 1.0$ . Analytically, one can calculate the area  
1006 under the line is equal to 30 units for  $0 \leq x \leq 10$ . Using Monte Carlo techniques,  
1007 one can calculate the area under this line by throwing many random values for the  $x$   
1008 and  $y$  components of each sample and then calculating whether that point falls below  
1009 the line. The area can then be calculated by the ratio of points below the line to the  
1010 total number of samples thrown multiplied by the total area in which samples were  
1011 scattered. The study is shown in Figure 4.1 highlights this technique and finds the area  
1012 under the curve to be 29.9 compared to an analytical solution of 30.0. The deviation  
1013 of the numerical to analytical solution can be attributed to the number of samples  
1014 used in the study. The accuracy of the approximation in which the properties of the  
1015 Monte Carlo samples replicate those of the desired distribution is dependent on the  
1016 number of samples used. Replicating this study with a differing number of Monte  
1017 Carlo samples used in each study (As shown in Figure 4.2) highlights how the Monte  
1018 Carlo techniques are only accurate within the limit of a high number of samples.

1019 Whilst the above example has an analytical solution, these techniques are just as  
1020 applicable to complex solutions. Clearly, any numerical solution is only as useful as its  
1021 efficiency. As discussed, the accuracy of the Monte Carlo technique is dependent upon  
1022 the number of samples generated to approximate the properties of the distribution.

Furthermore, if the positions at which the samples are evaluated are not ‘cleverly’ picked, the efficiency of the Monte Carlo technique significantly drops. Given the example in Figure 4.1, if the region in which the samples are scattered significantly extends passed the region of interest, many calculations will be calculated but do not add to the ability of the Monte Carlo technique to achieve the correct result. For instance, any sample evaluated at a  $y \geq 5$  could be removed without affecting the final result. This does bring in an aspect of the ‘chicken and egg’ problem in that to achieve efficient sampling, one needs to know the distribution beforehand.

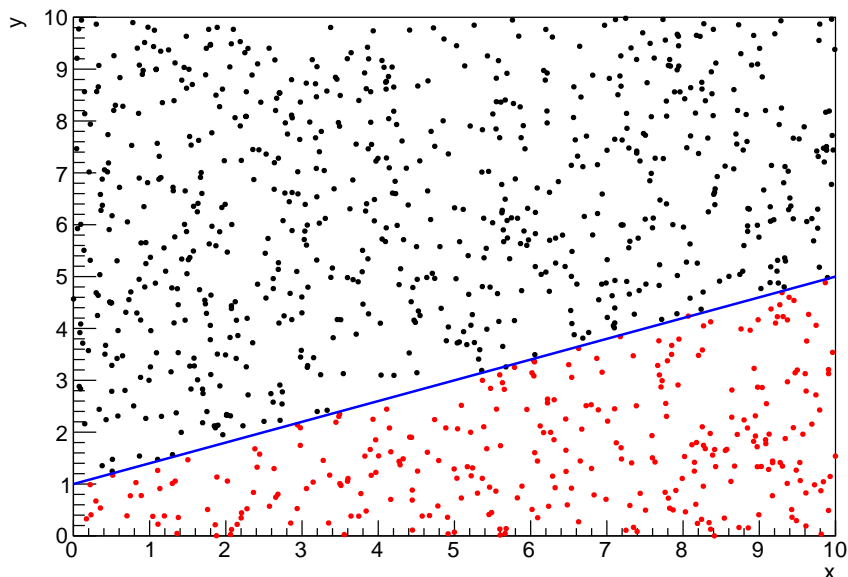


**Figure 4.1:** Example of using Monte Carlo techniques to find the area under the blue line. The gradient and intercept of the line are 0.4 and 1.0 respectively. The area found to be under the curve using one thousand samples is 29.9 units.

### 4.2.1 Markov Chain Monte Carlo

This analysis utilises a multi-dimensional probability distribution, with some dimensions being significantly more constrained than others. This could be from prior knowledge of parameter distributions from external data or un-physical regions in

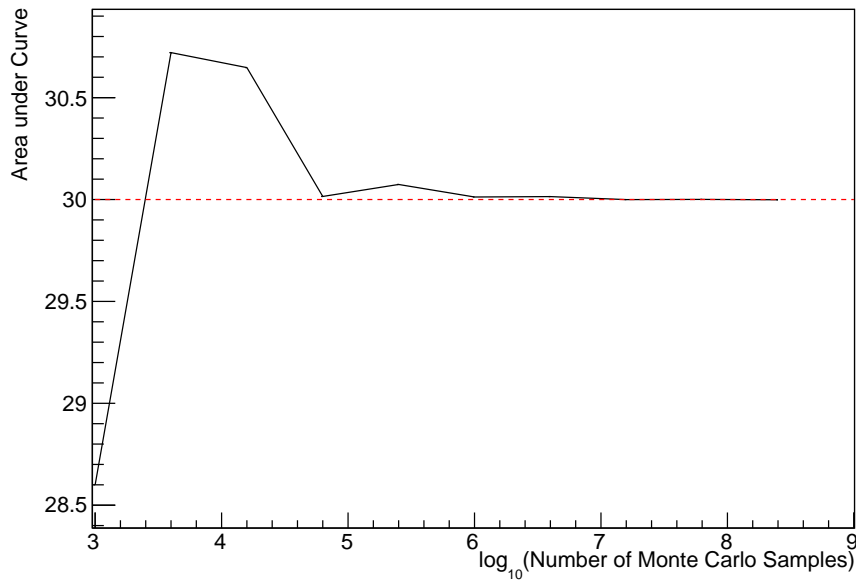


**Figure 4.2:** The area under a line of gradient 0.4 and intercept 1.0 for the range  $0 \leq x \leq 10$  as calculated using Monte Carlo techniques as a function of the number of samples used in each repetition. The analytical solution to the area is 30 units as given by the red line.

which parameters can not exist. Consequently, the Monte Carlo techniques used need to be as efficient as possible. For this analysis, the Markov Chain Monte Carlo (MCMC) technique is chosen. An MCMC technique is a Monte Carlo technique that uses a Markov chain to select which points at which to sample the parameter distribution. This technique performs a semi-random stochastic walk through the allowable parameter space. This builds a posterior distribution which has the property that the density of sampled points is proportional to the probability density of that parameter. This does mean that the samples produced by this technique are not statistically independent but they will cover the space of the distribution.

A Markov chain functions by selecting the position of step  $\vec{x}_{i+1}$  based on the position of  $\vec{x}_i$ . The space in which the Markov chain selects samples is dependent upon the total number of parameters utilised within the fit, where a discrete point in this space is described by the N-dimensional space  $\vec{x}$ . In a perfectly operating Markov chain, the position of the next step depends solely on the previous step and not on the

1049 further history of the chain ( $\vec{x}_0, \vec{x}_1$ , etc.). However, in solving the multi-dimensionality  
 1050 of the fit used within this analysis, each step becomes correlated with several of  
 1051 the steps preceding itself. This behaviour is further explained in subsection 4.2.3.  
 1052 Providing the MCMC chain is well optimised, it will begin to converge towards a  
 1053 unique stationary distribution. The period between the chain's initial starting point  
 1054 and the convergence to the unique stationary distribution is colloquially known as the  
 1055 burn-in period. This is discussed further in subsection 4.2.3. Once the chain reaches  
 1056 the stationary distribution, all points sampled after that point will look like samples  
 1057 from that distribution.

1058 Further details of the theories underpinning MCMC techniques are discussed  
 1059 in [132] but can be summarised by the requirement that the chain satisfies the three  
 1060 'regularity conditions':

- 1061     • Irreducibility: From every position in the parameter space  $\vec{x}$ , there must exist a  
     1062       non-zero probability for every other position in the parameter space to be reached.
- 1063     • Recurrence: Once the chain arrives at the stationary distribution, every step fol-  
     1064       lowing from that position must be samples from the same stationary distribution.
- 1065     • Aperiodicity: The chain must not repeat the same sequence of steps at any point  
     1066       throughout the sampling period.

1067 The output of the chain after burn-in (ie. the sampled points after the chain  
 1068 has reached the stationary distribution) can be used to approximate the posterior  
 1069 distribution and model parameters  $\vec{\theta}$ . To achieve the requirement that the unique  
 1070 stationary distribution found by the chain be the posterior distribution, one can use  
 1071 the Metropolis-Hastings algorithm. This guides the stochastic process depending on  
 1072 the likelihood of the current proposed step compared to that of the previous step.  
 1073 Implementation and other details of this technique are discussed in subsection 4.2.2.

## <sup>1074</sup> 4.2.2 Metropolis-Hastings Algorithm

<sup>1075</sup> As a requirement for MCMCs, the Markov chain implemented in this technique must  
<sup>1076</sup> have a unique stationary distribution that is equivalent to the posterior distribution.  
<sup>1077</sup> To ensure this requirement and that the regularity conditions are met, this analysis  
<sup>1078</sup> utilises the Metropolis-Hastings (MH) algorithm [136,137]. For the  $i^{th}$  step in the chain,  
<sup>1079</sup> the MH algorithm determines the position in the parameter space to which the chain  
<sup>1080</sup> moves to based on the current step,  $\vec{x}_i$ , and the proposed step,  $\vec{y}_{i+1}$ . The proposed step  
<sup>1081</sup> is randomly selected from some proposal function  $f(\vec{x}_{i+1}|\vec{x}_i)$ , which depends solely  
<sup>1082</sup> on the current step (ie. not the further history of the chain). The next step in the chain  
<sup>1083</sup>  $\vec{x}_{i+1}$  can be either the current step or the proposed step determined by whether the  
<sup>1084</sup> proposed step is accepted or rejected. To decide if the proposed step is selected, the  
<sup>1085</sup> acceptance probability,  $\alpha(\vec{x}_i, \vec{y}_i)$ , is calculated as

$$\alpha(\vec{x}_i, \vec{y}_{i+1}) = \min\left(1, \frac{P(\vec{y}_{i+1}|D)f(\vec{x}_i|\vec{y}_{i+1})}{P(\vec{x}_i|D)f(\vec{y}_{i+1}|\vec{x}_i)}\right). \quad (4.4)$$

<sup>1086</sup> Where  $P(\vec{y}_{i+1}|D)$  is the posterior distribution as introduced in section 4.1. To  
<sup>1087</sup> simplify this calculation, the proposal function is required to be symmetric such that  
<sup>1088</sup>  $f(\vec{x}_i|\vec{y}_{i+1}) = f(\vec{y}_{i+1}|\vec{x}_i)$ . In practice, a multi-variate Gaussian distribution is used to  
<sup>1089</sup> throw parameter proposals from. This reduces Equation 4.4 to

$$\alpha(\vec{x}_i, \vec{y}_{i+1}) = \min\left(1, \frac{P(\vec{y}_{i+1}|D)}{P(\vec{x}_i|D)}\right). \quad (4.5)$$

After calculating this quantity, a random number,  $\beta$ , is generated uniformly between 0 and 1. If  $\beta \leq \alpha(\vec{x}_i, \vec{y}_{i+1})$ , the proposed step is accepted. Otherwise, the chain sets the next step equal to the current step and this procedure is repeated. This can be interpreted as if the posterior probability of the proposed step is greater than that of the current step, ( $P(\vec{y}_{i+1}|D) \geq P(\vec{x}_i|D)$ ), the proposed step will always be accepted. If the opposite is true, ( $P(\vec{y}_{i+1}|D) \leq P(\vec{x}_i|D)$ ), the proposed step will be accepted with probability  $P(\vec{x}_i|D)/P(\vec{y}_{i+1}|D)$ . This ensures that the Markov chain does not get trapped in any local minima in the potentially non-Gaussian posterior distribution. The outcome of this technique is that the density of steps taken in a discrete region is directly proportional to the probability density in that region.

### **4.2.3 MCMC Optimisation**

As discussed in subsection 4.2.2, the proposal function invoked within the MH algorithm can take any form and the chain will still converge to the stationary distribution. ~~As discussed in Link to Analysis Strategy Section, this analysis performs the Monte Carlo reweighting on an event-by-event basis. This requires significant computational resources to perform a parameter fit At each set of proposed parameter values, a prediction of the same spectra has to be generated which requires significant computational resources.~~ Therefore, the number of steps taken before the unique stationary distribution is found should be minimised as only steps after convergence add information to the **fit oscillation analysis**. Furthermore, the chain should entirely cover the allowable parameter space to ensure that all values have been considered. Tuning the distance that the proposal function jumps between steps on a parameter-by-parameter basis can both minimise the length of the burn-in period and ensure that the correlation between step  $\vec{x}_i$  and  $\vec{x}_j$  is sufficiently small.

1114        The effect of changing the width of the proposal function is highlighted in Figure 4.3.  
1115        Three scenarios, each with the same underlying stationary distribution (A Gaussian of  
1116        width 1.0 and mean 0.), are presented. The only difference between the three scenarios  
1117        is the width of the proposal function, colloquially known as the ‘step size  $\sigma$ ’. Each  
1118        scenario starts at an initial parameter value of 10.0 which would be considered an  
1119        extreme variation. For the case where  $\sigma = 0.1$ , it is clear to see that the chain takes  
1120        a long time to reach the expected region of the parameter. This indicates that this  
1121        chain would have a large burn-in period and does not converge to the stationary  
1122        distribution until step  $\sim 500$ . Furthermore, whilst the chain does move towards the  
1123        expected region, each step is significantly correlated with the previous. Considering  
1124        the case where  $\sigma = 5.0$ , the chain approaches the expected parameter region almost  
1125        instantly meaning that the burn-in period is not significant. However, there are clearly  
1126        large regions of steps where the chain does not move. This is likely due to the chain  
1127        proposing steps in the tails of the distribution which have a low probability of being  
1128        accepted. Consequently, this chain would take a significant number of steps to fully  
1129        span the allowable parameter region. For the final scenario, where  $\sigma = 0.5$ , you can see  
1130        a relatively small burn-in period of approximately 100 steps. Once the chain reaches  
1131        the stationary distribution, it moves throughout the expected region of parameter  
1132        values many times, sufficiently sampling the full parameter region. This example is a  
1133        single parameter varying across a continuous distribution and does not fully reflect  
1134        the difficulties in the many-hundred multi-variate parameter distribution used within  
1135        this analysis. However, it does give a conceptual idea of the importance of selecting  
1136        the proposal function and associated step size.

1137        As discussed, step size tuning directly correlates to the average step acceptance  
1138        rate. If the step size is too small, many steps will be accepted but the chain moves  
1139        slowly. If the opposite is true, many steps will be rejected as the chain proposes steps  
1140        in the tails of the distribution. Discussion in [138] suggests that the ‘ideal’ acceptance

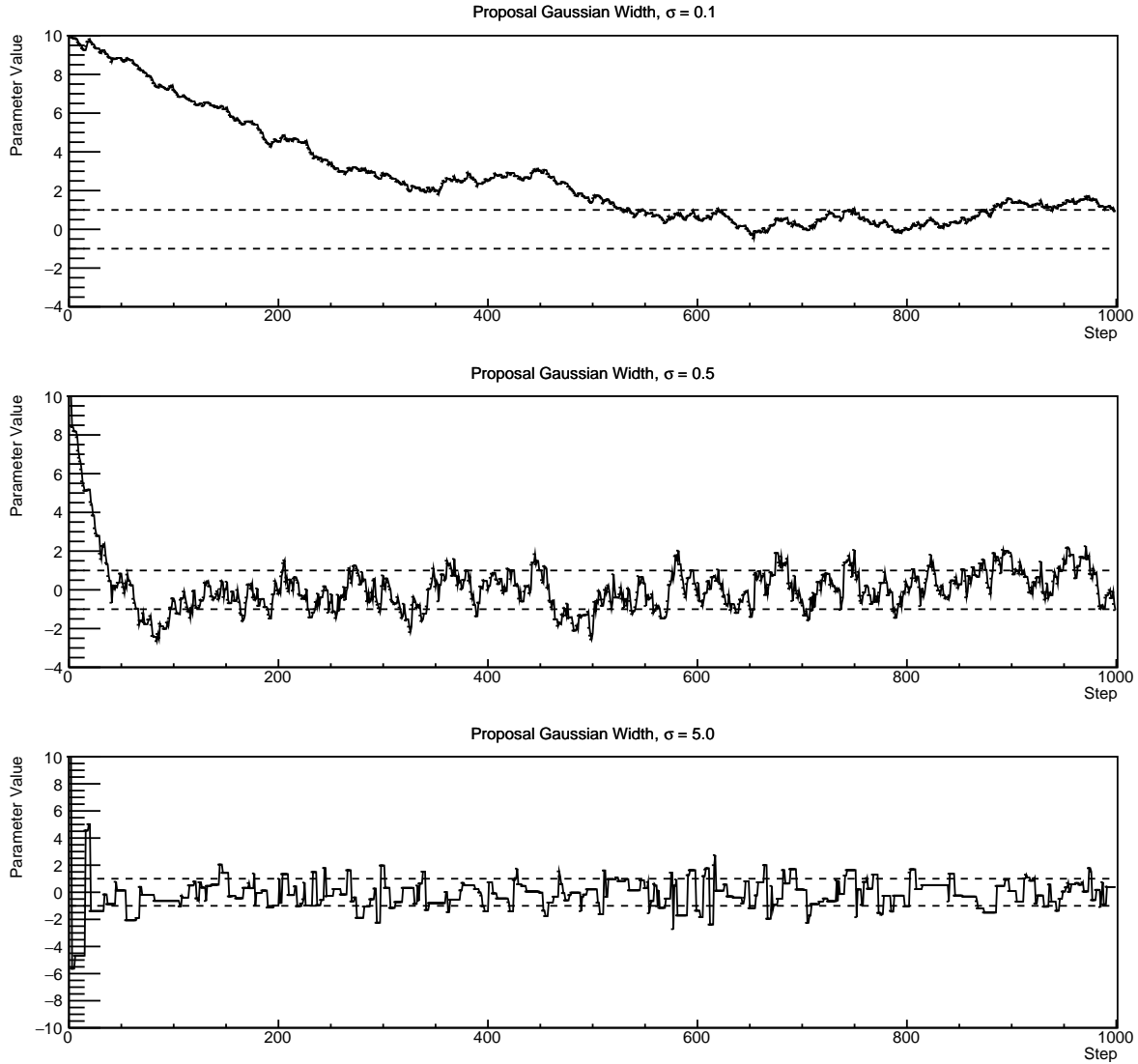


**Figure 4.3:** Three MCMC chains, each with a stationary distribution equal to a Gaussian centered at 0 and width 1 (As indicated by the black dotted lines). All of the chains use a Gaussian proposal function but have different widths (or ‘step size  $\sigma$ ’). The top panel has  $\sigma = 0.1$ , middle panel has  $\sigma = 0.5$  and the bottom panel has  $\sigma = 5.0$ .

<sup>1141</sup> rate of a high dimension MCMC chain should be approximately  $\sim 25\%$ . An “ideal”

<sup>1142</sup> step size [138] of

$$\sigma = \frac{2.4}{N_p}, \quad (4.6)$$

1143 where  $N_p$  is the number of parameters included in the MCMC fit. However, the  
 1144 complex correlations between systematics mean that some parameters have to be hand  
 1145 tuned and many efforts have been taken to select a set of parameter-by-parameter step  
 1146 sizes to approximately reach the ideal acceptance rate.

1147 Figure 4.3 highlights the likelihood as calculated by the fit in [DB: Link to AsimovA](#)  
 1148 [Sensitivity Section](#) as a function of the number of steps in each chain. In practice,  
 1149 many independent MCMC chains are run simultaneously to parallelise the task of  
 1150 performing the fit. This figure overlays the distribution found in each chain. As seen,  
 1151 the likelihood decreases from its initial value and converges towards a stationary  
 1152 distribution after  $\sim 1 \times 10^5$  steps. ~~Each fit (whether it be different asimov fits or data~~  
~~fit) will have a different set of preferred parameter values which results in a differ-~~  
~~ent stationary distribution. For each fit presented in this thesis, a burn-in period of~~  
~~1  $\times 10^5$  steps was found to be sufficient.~~

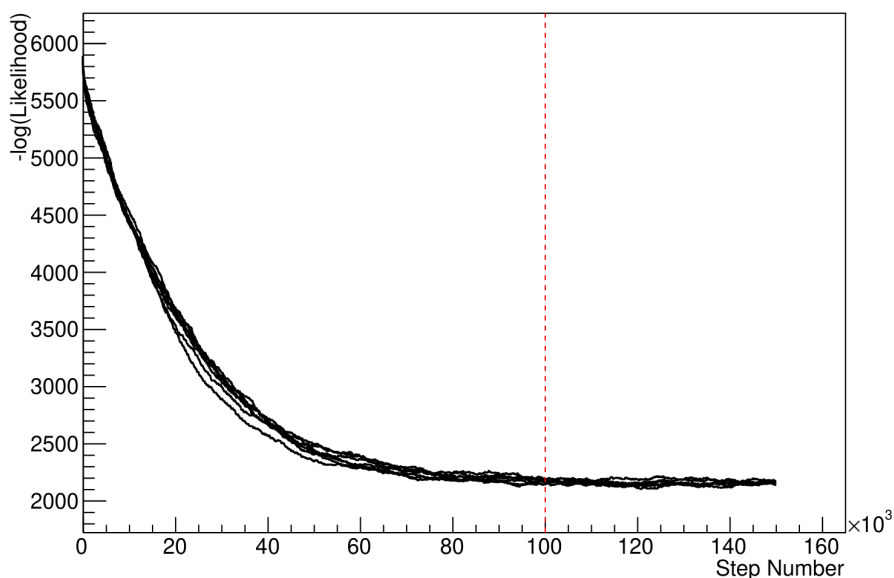


**Figure 4.4:** The log-likelihood from the fit detailed in [DB: Link to AsimovA](#) [Sensitivity Section](#) as a function of the number of steps accumulated in each fit. Many independent MCMC chains were run in parallel and overlaid on this plot. The red line indicates the  $1 \times 10^5$  step burn-in period after which the log-likelihood becomes stable.

1156     Multiple configurations of this analysis have been performed throughout this  
1157     thesis where different samples or systematics have been used. For all of these  
1158     configurations, it was found that a burnin period of  $1 \times 10^5$  was sufficient in all  
1159     cases.

## 1160   4.3 Understanding the MCMC Results

1161   Whilst [Link](#) and [Link](#) describe how to interpret Bayesian statistics and explains the  
1162   MCMC techniques used within this analysis, there is no mention of how to inter-  
1163   pret the output of the chain. The previous sections have described how to generate  
1164   the posterior probability distribution using Bayesian MCMC techniques. How-  
1165   ever, this analysis focuses on oscillation parameter determination. The posterior  
1166   distribution output from the chain is a high dimension object, with as many dimen-  
1167   sions as there are parameters included in the [fit oscillation analysis](#). However, this  
1168   multi-dimensional object is difficult to conceptualize so parameter estimations are  
1169   often presented in one or two-dimensional projections of this probability distribution.  
1170   To do this, we invoke the marginalisation technique highlighted in subsection 4.3.1.

### 1171   4.3.1 Marginalisation

1172   The output of the MCMC chain is a highly dimensional probability distribution  
1173   which is very difficult to interpret. From the standpoint of an oscillation analysis  
1174   experiment, the one or two-dimensional ‘projections’ of the oscillation parameters of  
1175   interest are most relevant. Despite this, the best fit values and uncertainties on the  
1176   oscillation parameters of interest should correctly encapsulate the correlations to the  
1177   other systematic uncertainties (colloquially called ‘nuisance’ parameters). For this joint  
1178   beam and atmospheric analysis, the oscillation parameters of interest are  $\sin^2(\theta_{23})$ ,

1179  $\sin^2(\theta_{13})$ ,  $\Delta m_{23}^2$ , and  $\delta_{CP}$ . All other parameters (Including the oscillation parameter  
 1180 this fit is insensitive to) are deemed nuisance parameters. To generate these projections,  
 1181 we rely upon integrating the posterior distribution over all nuisance parameters. This  
 1182 is called marginalisation. A simple example of this technique is to imagine the scenario  
 1183 where two coins are flipped. To determine the probability that the first coin returned  
 1184 a ‘head’, the exact result of the second coin flip is disregarded and simply integrated  
 1185 over. For the parameters of interest,  $\vec{\theta}_i$ , we can calculate the marginalised posterior by  
 1186 integrating over the nuisance parameters,  $\vec{\theta}_n$ . In this case, Equation 4.2 becomes

$$P(\vec{\theta}_i|D) = \frac{\int P(D|\vec{\theta}_i, \vec{\theta}_n)P(\vec{\theta}_i, \vec{\theta}_n)d\vec{\theta}_n}{\int P(D|\vec{\theta})P(\vec{\theta})d\vec{\theta}} \quad (4.7)$$

1187 Where  $P(\vec{\theta}_i, \vec{\theta}_n)$  encodes the prior knowledge about the uncertainty and correlations  
 1188 between the parameters of interest and the nuisance parameters. In practice, this  
 1189 is simply taking the one or two-dimensional projection of the multi-dimensional  
 1190 probability distribution.

1191 Whilst in principle an easy solution to a complex problem, correlations between the  
 1192 interesting and nuisance parameters can bias the marginalised results. A similar effect  
 1193 is found when the parameters being marginalised over have non-Gaussian probability  
 1194 distributions. For example, Figure 4.5 highlights the marginalisation bias in the  
 1195 probability distribution found for a parameter when requiring a correlated parameter  
 1196 to have a positive parameter value. Due to the complex nature of this oscillation  
 1197 parameter fit presented in this thesis, there are **certainly** correlations occurring between  
 1198 the oscillation parameters of interest and the other nuisance parameters included in  
 1199 the fit.

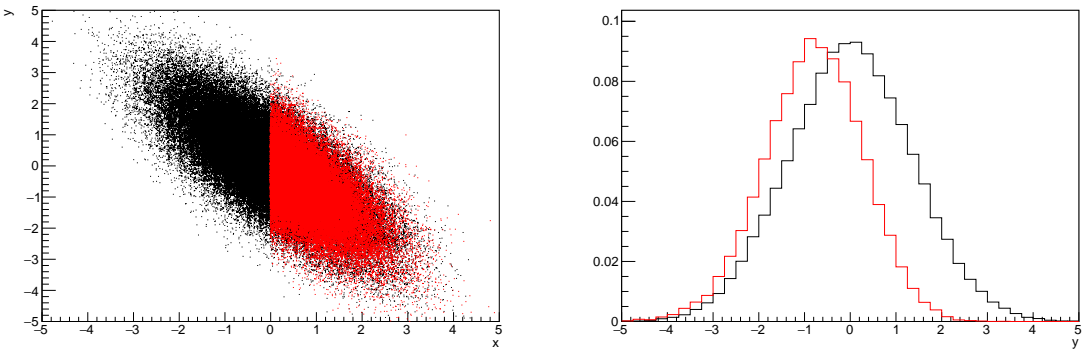


**Figure 4.5:** Left: The two dimensional probability distribution for two correlated parameters  $x$  and  $y$ . The red distribution shows the two dimensional probability distribution when  $0 \leq x \leq 5$ . Right: The marginalised probability distribution for the  $y$  parameter found when requiring the  $x$  to be bound between  $-5 \leq x \leq 5$  for the black and red distribution, respectively.

### 1200 4.3.2 Parameter Estimation and Credible Intervals

1201 The purpose of this analysis is to determine the best fit values for the oscillation  
 1202 parameters that the beam and atmospheric samples are sensitive to:  $\sin^2(\theta_{23})$ ,  $\sin^2(\theta_{13})$   
 1203 ,  $\Delta m_{23}^2$ , and  $\delta_{CP}$ . Typically, the results presented take the form of one or two-dimension  
 1204 marginalised probability distributions for the appearance ( $\sin^2(\theta_{13})$  and  $\delta_{CP}$ ) and  
 1205 disappearance ( $\sin^2(\theta_{23})$  and  $\Delta m_{23}^2$ ) parameters. The posterior probability density  
 1206 taken from the output MCMC chain is binned in these parameters. The parameter  
 1207 best-fit point is then taken to be the value that has the highest posterior probability.  
 1208 This is performed in both one and two-dimensional projections.

1209 However, the single best-fit point in a given parameter is not of much use on its  
 1210 own. We would also like to determine the uncertainty, or credible interval, on that  
 1211 best-fit point. The definition of the  $1\sigma$  credible interval is that we have 68% belief that  
 1212 the parameter is within those bounds. For a more generalised definition, the credible  
 1213 interval is the region,  $R$ , of the posterior distribution that contains a specific fraction of  
 1214 the total probability, such that

$$\int_R P(\theta|D)d\theta = \alpha \quad (4.8)$$

<sub>1215</sub> Where  $\theta$  is the parameter on which we calculate the credible interval. This technique  
<sub>1216</sub> then calculates the  $\alpha \times 100\%$  credible interval.

<sub>1217</sub> In practice, this analysis uses the highest posterior density (HPD) credible intervals  
<sub>1218</sub> which are calculated through the following method. First, the probability distribution  
<sub>1219</sub> is area-normalised such that it has an integrated area equal to 1.0. The bins of proba-  
<sub>1220</sub> bility are then summed from the highest to lowest until the sum exceeds the  $1\sigma$  level  
<sub>1221</sub> ( $0.68$  in this example). This process is repeated for a range of credible intervals, notably  
<sub>1222</sub> the  $1\sigma$ ,  $2\sigma$  and  $3\sigma$  along with other levels where the critical values for each level can  
<sub>1223</sub> be found in [139]. This process can be repeated for the two-dimensional probability  
<sub>1224</sub> distributions by creating two-dimensional contours of credible intervals rather than a  
<sub>1225</sub> one-dimensional result.

### <sub>1226</sub> 4.3.3 Bayesian Model Comparisons

<sub>1227</sub> Due to the matter resonance, this analysis has some sensitivity to the mass hierarchy  
<sub>1228</sub> of neutrino states (whether  $\Delta m_{23}^2$  is positive or negative) and the octant of  $\sin^2(\theta_{23})$   
<sub>1229</sub> . The Bayesian approach utilised within this analysis gives an intuitive method of  
<sub>1230</sub> model comparison by determining which hypothesis is most favourable. Taking the  
<sub>1231</sub> ratio of Equation 4.3 for the two hypotheses of normal hierarchy,  $NH$ , and inverted  
<sub>1232</sub> hierarchy,  $IH$ , gives

$$\frac{P(\vec{\theta}_{NH}|D)}{P(\vec{\theta}_{IH}|D)} = \frac{P(D|\vec{\theta}_{NH})}{P(D|\vec{\theta}_{IH})} \times \frac{P(\vec{\theta}_{NH})}{P(\vec{\theta}_{IH})}. \quad (4.9)$$

1233     The middle term defines the Bayes factor which is a data-driven interpretation of  
 1234     how strong the data prefers one hierarchy to the other. For this analysis, equal priors  
 1235     on both mass hierarchy hypotheses are chosen ( $P(\vec{\theta}_{NH}) = P(\vec{\theta}_{IH}) = 0.5$ ). In practice,  
 1236     the MCMC chain proposes a value of  $|\Delta m_{23}^2|$  and then applies a 50% probability  
 1237     that the value is sign flipped. Consequently, the Bayes factor can be calculated from  
 1238     the ratio of the probability density in either hypothesis. This equates to counting the  
 1239     number of steps taken in the normal and inverted hierarchies and taking the ratio. The  
 1240     same approach can be taken to compare the upper octant (UO) compared to the lower  
 1241     octant (LO) hypothesis of  $\sin^2(\theta_{23})$ .

1242     Whilst the value of the Bayes factor should always be shown, the Jeffreys scale [140]  
 1243     (highlighted in Table 4.1) gives an indication of the strength of preference for one model  
 1244     compared to the other. Other interpretations of the strength of preference of a model  
 1245     exist, e.g. the Kass and Raferty Scale [141].

$\log_{10}(B_{AB})$	$B_{AB}$	Strength of Preference
$< 0.0$	$< 1$	No preference for hypothesis A (Supports hypothesis B)
$0.0 - 0.5$	$1.0 - 3.16$	Preference for hypothesis A is weak
$0.5 - 1.0$	$3.16 - 10.0$	Preference for hypothesis A is substantial
$1.0 - 1.5$	$10.0 - 31.6$	Preference for hypothesis A is strong
$1.5 - 2.0$	$31.6 - 100.0$	Preference for hypothesis A is very strong
$> 2.0$	$> 100.0$	Decisive preference for hypothesis A

**Table 4.1:** Jeffreys scale for strength of preference for two models  $A$  and  $B$  as a function of the calculated Bayes factor ( $B_{AB} = B(A/B)$ ) between the two models [140]. The original scale is given in terms of  $\log_{10}(B(A/B))$  but converted to linear scale for easy comparison throughout this thesis.

#### 1246 4.3.4 Comparison of MCMC Output to Expectation

1247 ~~Whilst not important for the extraction of oscillation parameters, understanding~~  
1248 ~~how the data constrains the model parameters is important to the understanding~~  
1249 ~~of this analysis. To ensure the fit is performing well, a best-fit spectra is produced~~  
1250 ~~using the posterior probability distribution and compared with the data, allowing~~  
1251 ~~easy by-eye comparisons to be made.~~ A simple method of doing this is to perform a  
1252 comparison in the fitting parameters (For instance, the reconstructed neutrino energy  
1253 and lepton direction for T2K far detector beam samples) of the spectra generated by  
1254 the MCMC chain to ‘data’. This ‘data’ could be true data or some variation of Monte  
1255 Carlo prediction. This allows easy comparison of the MCMC probability distribution  
1256 to the data. To perform this,  $N$  steps from the post burn-in MCMC chain are randomly  
1257 selected (Where for all plots of this style in this thesis,  $N = 3000$ ). From these, the  
1258 Monte Carlo prediction at each step is generated by reweighting the model parameters  
1259 to the values specified at that step. Due to the probability density being directly  
1260 correlated with the density of steps in a certain region, parameter values close to the  
1261 best fit value are most likely to be selected.

1262 In practice, for each bin of the fitting parameters has a probability distribution  
1263 of event rates, with one entry per sampled MCMC step. This distribution is binned  
1264 where the bin with the highest probability is selected as the mean and an error on  
1265 the width of this probability distribution is calculated using the approach highlighted  
1266 in subsection 4.3.2. Consequently, the best fit distribution in the fit parameter is not  
1267 necessarily that which would be attained by reweighting the Monte Carlo prediction  
1268 to the most probable parameter values.

1269 A similar study can be performed to illustrate the freedom of the model parameter  
1270 space prior to the fit. This can be done by throwing parameter values from the prior

<sub>1271</sub> uncertainty of each parameter. This becomes troublesome for parameters with no  
<sub>1272</sub> prior uncertainty as the range is technically infinite. Where applicable solutions to  
<sub>1273</sub> remove these have been addressed.

1274 **Chapter 5**

1275 **Simulation, Reconstruction, and Event  
1276 Selections**

1277 As a crucial part of the oscillation analysis, an accurate prediction of the expected  
1278 neutrino spectrum at the far detector is required. This includes modeling the flux  
1279 generation, neutrino interactions, and detector effects. All of the simulation packages  
1280 required to do this are briefly described in section 5.1. The reconstruction of neutrino  
1281 events inside the far detector, including the `fitQun` algorithm, is documented in  
1282 section 5.2. This also includes data quality checks of the SK-V data which the author  
1283 performed for the T2K oscillation analysis presented at Neutrino 2020 [80]. Finally,  
1284 section 5.3 describes the steps taken in the SK detector to trigger on events of interest  
1285 whilst removing the comparatively large rate of cosmic ray muon events.

1286 **5.1 Simulation**

1287 In order to generate a Monte Carlo prediction of the expected event rate at the far  
1288 detector, all the processes in the beam and atmospheric flux, neutrino interaction, and  
1289 detector need to be modeled. Each of these parts is individually modeled and each of  
1290 them is detailed below.

1291 The beamline simulation consists of three distinct parts: the initial hadron inter-  
1292 action modeled by FLUKA [142], the target station geometry and particle tracking

1293 performed by JNUBEAM, [143, 144] and any hadronic re-interactions simulated by  
 1294 GCALOR [145]. The primary hadronic interactions are  $O(10)\text{GeV}$ , where FLUKA  
 1295 matches external cross-section data better than GCALOR [146]. However, FLUKA  
 1296 is not very adaptable so a small simulation is built to model the interactions in the  
 1297 target and the output is then passed to JNUBEAM and GCALOR for propagation.  
 1298 The hadronic interactions are tuned to data from the NA61/SHINE [147–149] and  
 1299 HARP [150] experiments. The tuning is done by reweighting the FLUKA and GCALOR  
 1300 predictions to match the external data multiplicity and cross-section measurements,  
 1301 based on final state particle kinematics [146]. The culmination of this simulation  
 1302 package generates the predicted flux for neutrino and antineutrino beam modes which  
 1303 are illustrated in Figure 3.7.

1304 The atmospheric neutrino flux predictions are simulated by the HKKM model  
 1305 [43, 45]. The primary cosmic ray flux is tuned to AMS [151] and BESS [152] data assum-  
 1306 ing the US-standard atmosphere '76 [153] density profile and includes geomagnetic  
 1307 field effects. The primary cosmic rays interact to generate pions and muons. The  
 1308 interaction of these secondary particles to generate neutrinos is handled by DPMJET-  
 1309 III [154] for energies above 32GeV and JAM [45, 155] for energies below that value **DB:**  
 1310 **Question for Giles: Why different generators for above/below 32GeV?** These hadronic  
 1311 interactions are tuned to BESS and L3 data [156, 157] using the same methodology  
 1312 as the tuning of the beamline simulation. The energy and cosine zenith predictions  
 1313 of  $\nu_e, \bar{\nu}_e, \nu_\mu, \bar{\nu}_\mu$  flux are given in Figure 2.3 and Figure 2.5, respectively. The flux is  
 1314 approximately symmetrical and peaked around the horizon ( $\cos(\theta_Z) = 0.0$ ). This is be-  
 1315 cause horizontally-going pions and kaons can travel further than their vertically-going  
 1316 counterparts resulting in a larger probability of decaying to neutrinos. The symmetry  
 1317 is broken in low-energy neutrinos due to geomagnetic effects, which modify the track  
 1318 of the primary cosmic rays. Updates to the HKKM model are currently ongoing [158].

Once a flux prediction has been made for all three detectors, NEUT 5.4.0 [159, 160] models the interactions of the neutrinos in the detectors. For the purposes of this analysis, quasi-elastic (QE), meson exchange (MEC), single meson production (PROD), coherent pion production (COH), and deep inelastic scattering (DIS) interactions are simulated. These interaction categories can be further broken down by whether they were propagated via a  $W^\pm$  boson in Charged Current (CC) interactions or via a  $Z^0$  boson in Neutral Current (NC) interactions. CC interactions have a charged lepton in the final state, which can be flavour-tagged in reconstruction to determine the flavour of the neutrino. In contrast, NC interactions have a neutrino in the final state so no flavour information can be determined from the observables left in the detector after an interaction. This is the reason why NC events are assumed to not oscillate within this analysis. Both CC and NC interactions are modeled for all the above interaction categories, other than MEC interactions which are only modeled for CC events. The SK detector is only sensitive to charged particles, so all charged current interactions are simulated whilst only neutral current processes that produce charged mesons (NCDIS, NCCOH, and NCProd) are modeled. NC MEC interactions can only produce charged particles through secondary re-interactions which is a low cross-section process.

As illustrated in Figure 5.1, CC QE interactions dominate the low-energy cross-section of neutrino interactions. The NEUT implementation adopts the Llewellyn Smith [161] model for neutrino-nucleus interactions, where the nuclear ground state of any bound nucleons (neutrino-oxygen interactions) is approximated by a spectral-function [162] model that simulates the effects of Fermi momentum and Pauli blocking. The cross-section of QE interactions are controlled by vector and axial-vector form factors parameterised by the BBBA05 [163] model and a dipole form factor with  $M_A^{QE} = 1.21\text{GeV}$  fit to external data [164], respectively. NEUT implements the Valencia [165] model to simulate MEC events, where two nucleons and two holes in the nuclear target are produced (Often called 2p2h interactions).

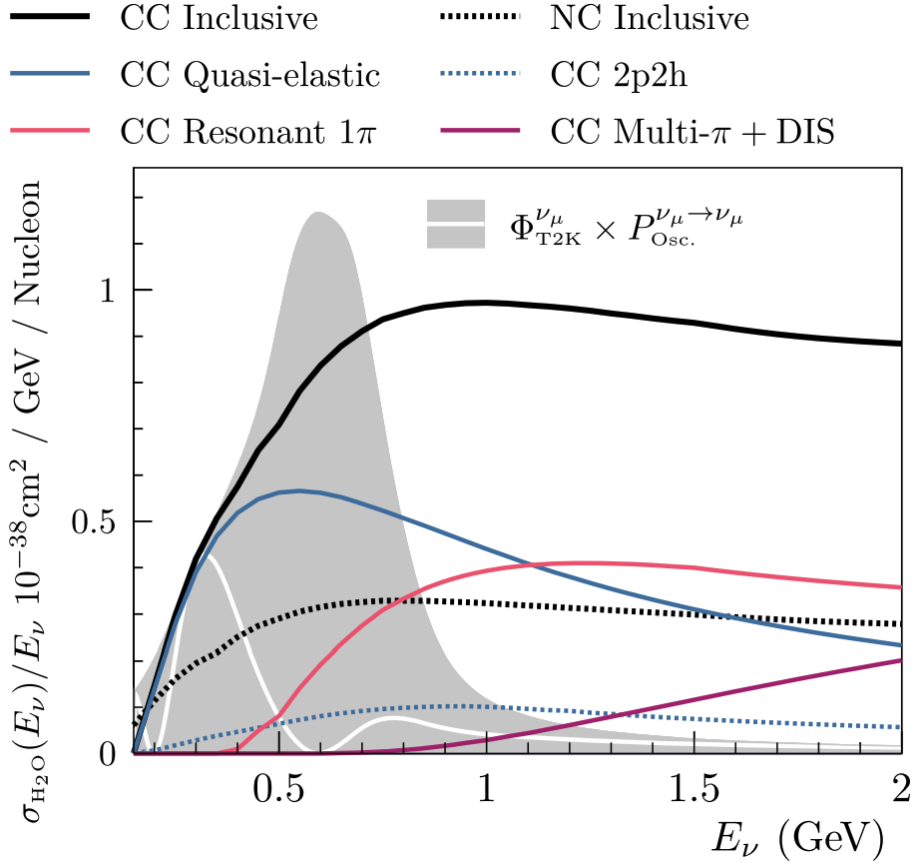


**Figure 5.1:** The NEUT prediction of the  $\nu_\mu$ -H<sub>2</sub>O cross-section overlaid on the T2K  $\nu_\mu$  flux. The charged current (black, solid) and neutral current (black, dashed) inclusive, charged current quasi-elastic (blue, solid), charged current 2p2h (blue, dashed), charged current single pion production (pink), and charged current multi- $\pi$  and DIS (Purple) cross-sections are illustrated. Figure taken from [159].

For neutrinos of energy  $O(1)\text{GeV}$ , PROD interactions become dominant. These predominantly produce charged and neutral pions although  $\gamma$ , kaon, and  $\eta$  production is also considered. To simulate these interactions, the Berger-Sehgal [166] model is implemented within NEUT. It simulates the excitation of a nucleon from a neutrino interaction, production of an intermediate baryon, and the consequential decay to a single meson or  $\gamma$ . Pions can also be produced through COH interactions, which occur when the incoming neutrino interacts with the entire oxygen nuclei target leaving a single pion outside of the nucleus. NEUT utilises the Berger-Sehgal [167] model to simulate these COH interactions.

<sub>1355</sub> DIS and multi- $\pi$  producing interactions become the most dominant for energies  
<sub>1356</sub>  $> O(5)\text{GeV}$ . PYTHIA [168] is used to simulate any interaction with invariant mass,  
<sub>1357</sub>  $W > 2\text{GeV}/c^2$ , which produces at least one meson. For any interaction which produces  
<sub>1358</sub> at least two mesons but has  $W < 2\text{GeV}/c^2$ , the Bronner model is invoked [169].  
<sub>1359</sub> Both of these models use Parton distribution functions based on the Bodek-Yang  
<sub>1360</sub> model [170–172].

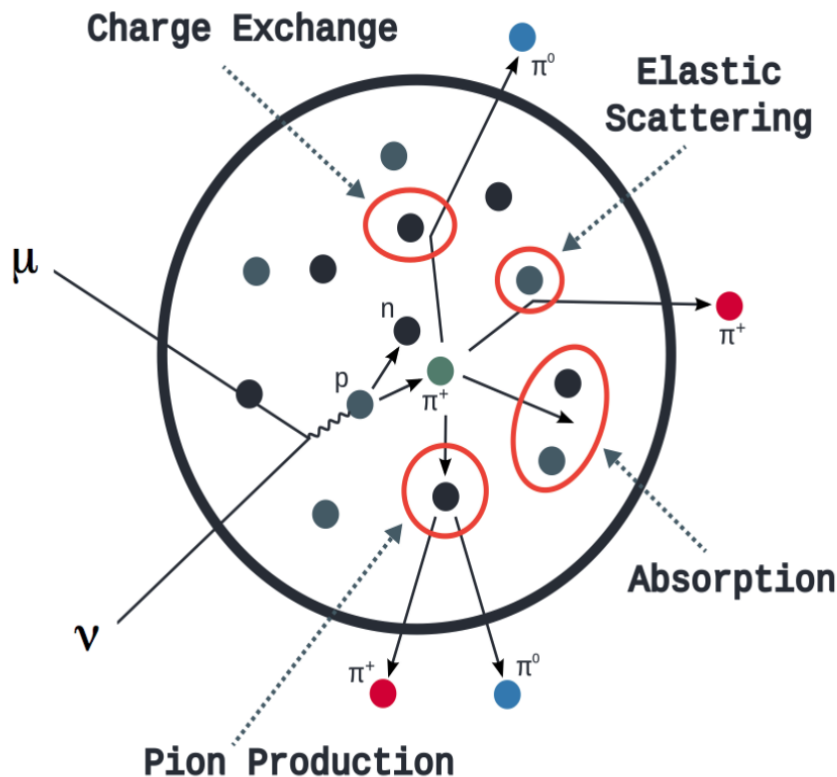


**Figure 5.2:** Illustration of the various processes which a pion can undergo before exiting the nucleus. Taken from [173].

<sub>1361</sub> Any pion which is produced within the nucleus can re-interact through final state  
<sub>1362</sub> interactions before it exits, as illustrated by the scattering, absorption, production, and  
<sub>1363</sub> exchange interactions in Figure 5.2. These re-interactions alter the observable particles  
<sub>1364</sub> within the detector. For instance, if the charged pion from a CC PROD interaction is  
<sub>1365</sub> absorbed, the observables would mimic a CC QE interaction. To simulate these effects,

1366 NEUT uses a semi-classical intranuclear cascade model [159]. This cascade functions by  
1367 stepping the pion through the nucleus in fixed-length steps equivalent to  $dx = R_N/100$ ,  
1368 where  $R_N$  is the radius of the nucleus. At each step, the simulation allows the pion  
1369 to interact through scattering, charged exchange, absorption, or production with an  
1370 interaction-dependent probability calculated from a fit to external data [174]. This  
1371 cascade continues until the pion is absorbed or exits the nucleus.

1372 Once the final state particle kinematics have been determined from NEUT, they  
1373 are passed into the detector simulation. The near detectors, ND280 and INGRID, are  
1374 simulated using a GEANT4 package [118,175] to simulate the detector geometry, particle  
1375 tracking, and energy deposition. The response of the detectors is simulated using  
1376 the elecSim package [118]. The far detector simulation is based upon the original  
1377 Kamiokande experiment software which uses the GEANT3-based SKDETSIM [118,176]  
1378 package. This controls the interactions of particles in the water as well as Cherenkov  
1379 light production. The water quality and PMT calibration measurements detailed in  
1380 subsection 3.1.2 are also used within this simulation to make accurate predictions of  
1381 the detector response.

## 1382 5.2 Event Reconstruction at SK

1383 Any above Cherenkov threshold event which occurs in SK will be recorded by the  
1384 PMT array, where each PMT records the time and accumulated charge. This recorded  
1385 information is shown in event displays similar to those illustrated in Figure 5.3. To  
1386 be useful for physics analyses, this series of PMT hit information needs to be recon-  
1387 structed to determine the particle's identity and kinematics (or track parameters):  
1388 four-vertex, direction, and momenta. This is because the charge and timing distribu-  
1389 tion of photons generated by a particular particle in an event is dependent upon its

1390 initial kinematics. The concept of distinguishing electron and muon events is from the  
1391 “fuzziness” of the ring. Muons are heavier and less affected by scattering or showering  
1392 meaning they typically produce “crisp” rings. Electrons are more likely to interact  
1393 via electromagnetic showering or scattering which results in larger variations of their  
1394 direction from the initial direction. Consequently, electrons typically produce “fuzzier”  
1395 rings compared to muons.

1396 For the purposes of this analysis, the `fitQun` reconstruction algorithm is utilised.  
1397 Its core function is to compare a prediction of the accumulated charge and timing  
1398 distribution from each PMT, generated for a particular particle identity and track  
1399 parameters, to that observed in the neutrino event. It determines the preferred values  
1400 by minimising a likelihood function which includes information from PMTs which  
1401 were hit and those that were not hit. The `fitQun` algorithm improves upon the APFit  
1402 reconstruction algorithm which has been used for many previous SK analyses. APFit  
1403 fits the vertex from timing information and then fits the momentum and direction  
1404 of the particle from PMT hits within a 43 deg Cherenkov cone (which assumes an  
1405 ultra-relativistic particle). It then fits the particle identity once the track parameters  
1406 have been fit. Conversely, `fitQun` performs a simultaneous fit of particle kinematics  
1407 and identity, improving both the accuracy of the fit parameters and the rejection of  
1408 neutral current  $\pi^0$  events [177,178]. The `fitQun` algorithm is based on the key concepts  
1409 of the MiniBooNE reconstruction algorithm [179] and is described in [180] which is  
1410 summarised below.

1411 An event in SK can consist of multiple particles. For example, a charge current  
1412 muon neutrino interaction can generate two particles that have the potential of gen-  
1413 erating Cherenkov photons: the primary muon, and the secondary decay-electron  
1414 from the muon. To ensure both subevents are reconstructed separately, each event is  
1415 divided into time clusters which are called “subevents”. The number of subevents is

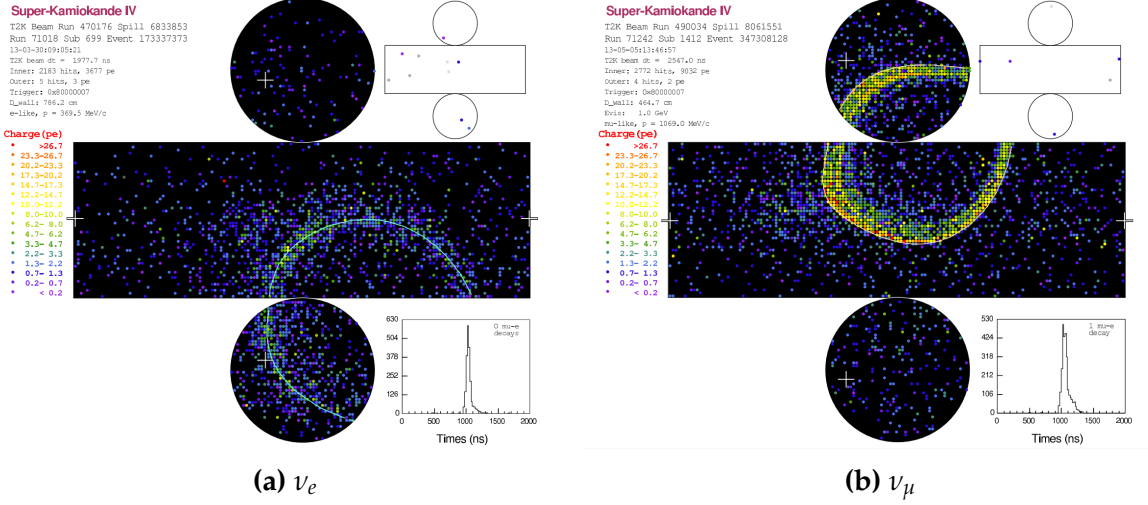


**Figure 5.3:** Event displays from Super Kamiokande illustrating the “crisp” ring from a muon and the typically “fuzzy” electron ring. Each pixel represents a PMT and the color scheme denotes the accumulated charge deposited on that PMT. Figures taken from [181].

<sup>1416</sup> equal to the number of decay electrons minus one (the primary event). To find all the  
<sup>1417</sup> subevents in an event, a vertex goodness metric is calculated for some vertex position  
<sup>1418</sup>  $\vec{x}$  and time  $t$ ,

$$G(\vec{x}, t) = \sum_i^{\text{hit PMTs}} \exp \left( -\frac{1}{2} \left( \frac{T_{Res}^i(\vec{x}, t)}{\sigma} \right)^2 \right) \quad (5.1)$$

<sup>1419</sup> where

$$T_{Res}^i(\vec{x}, t) = t^i - t - |R_{PMT}^i - \vec{x}| / c_n \quad (5.2)$$

<sup>1420</sup> is the residual hit time. It is the difference in time between the PMT hit time,  $t^i$ ,  
<sup>1421</sup> of the  $i^{th}$  PMT and the expected time of the PMT hit if the photon was emitted at  
<sup>1422</sup> the start of the vertex.  $R_{PMT}^i$  is the position of the  $i^{th}$  PMT,  $c_n$  is the speed of light in

1423 water and  $\sigma = 4\text{ns}$  which is comparable to the time resolution of the PMT. When the  
1424 proposed fit values of time and vertex are close to the true values,  $T_{Res}^i(\vec{x}, t)$  tends to  
1425 zero resulting in subevents appearing as spikes in the goodness metric. The proposed  
1426 fit vertex and time are grid-scanned, and the values which maximise the goodness  
1427 metric are selected as the “pre-fit vertex”. Whilst this predicts a vertex for use in  
1428 the clustering algorithm, the final vertex is fit using the higher-precision maximum  
1429 likelihood method described below.

1430 Once the pre-fit vertex has been determined, the goodness metric is scanned as  
1431 a function of  $t$  to determine the number of subevents. A peak-finding algorithm is  
1432 then used on the goodness metric, requiring the goodness metric to exceed some  
1433 threshold and drop below a reduced threshold before any subsequent additional  
1434 peaks are considered. The thresholds are set such that the rate of false peak finding  
1435 is minimised while still attaining good data to Monte Carlo agreement. To improve  
1436 performance, the pre-fit vertex for each delayed subevent is re-calculated after PMT  
1437 hits from the previous subevent are masked. This improves the decay-electron tagging  
1438 performance. Once all subevents have been determined, the time window around  
1439 each subevent is then defined by the earliest and latest time which satisfies  $-180 <$   
1440  $T_{Res}^i < 800\text{ns}$ . The subevents and associated time windows are then used as seeds for  
1441 further reconstruction.

1442 For a given subevent, the `fitQun` algorithm constructs a likelihood based on the  
1443 accumulated charge  $q_i$  and time information  $t_i$  from the  $i^{th}$  PMT,

$$L(\Gamma, \vec{\theta}) = \prod_j^{\text{unhit}} P_j(\text{unhit}|\Gamma, \vec{\theta}) \prod_i^{\text{hit}} \{1 - P_i(\text{unhit}|\Gamma, \vec{\theta})\} f_q(q_i|\Gamma, \vec{\theta}) f_t(t_i|\Gamma, \vec{\theta}), \quad (5.3)$$

where  $\vec{\theta}$  defines the track parameters; vertex position, direction vector and momenta, and  $\Gamma$  represents the particle hypothesis.  $P_i(\text{unhit}|\Gamma, \vec{\theta})$  defines the probability of the  $i^{\text{th}}$  tube to not register a hit given the track parameters and particle hypothesis. The charge likelihood,  $f_q(q_i|\Gamma, \vec{\theta})$ , and time likelihood,  $f_t(t_i|\Gamma, \vec{\theta})$ , represent the probability density function of observing charge  $q_i$  and time  $t_i$  on the  $i^{\text{th}}$  PMT given the specified track parameters and particle hypothesis.

As the generation and propagation of the optical photons are independent of the PMT and electronics response, it is natural to split the calculation into two. Firstly, the expected number of photoelectrons (or predicted charge),  $\mu_i = \mu_i(\vec{\theta}, \Gamma)$ , at the  $i^{\text{th}}$  PMT is calculated. This value is then substituted into the likelihood function. This allows the charge likelihood density  $f_q(q_i|\mu_i)$  and unhit probability  $P_i(\text{unhit}|\mu_i)$  to be expressed via quantities that are only dependent on the response of the PMT.

The predicted charge is calculated based on contributions from both the direct light and the scattered light. The direct light contribution is determined based on the integration of the Cherenkov photon profile along the track. PMT angular acceptance, water quality, and calibration measurements discussed in subsection 3.1.2 are included to accurately predict the charge probability density at each PMT. The scattered light is calculated in a similar way, although it includes a scattering function that depends on the vertex of the particle and the position of the PMT. The charge likelihood is calculated by comparing the prediction to the observed charge in the PMT.

The time likelihood is approximated to depend on the vertex  $\vec{x}$ , direction  $\vec{d}$ , and time  $t$  of the track parameters as well as the particle hypothesis. The expected time for PMT hits is calculated by assuming unscattered photons being emitted from the midpoint of the track,  $S_{\text{mid}}$ ,

$$t_{exp}^i = t + S_{mid}/c + |R_{PMT}^i - \vec{x} - S_{mid}\vec{d}|/c_n, \quad (5.4)$$

where  $c$  is the speed of light in a vacuum. The time likelihood is then expressed in terms of the residual difference between the PMT hit time and the expected hit time,  $t_{Res}^i = t^i - t_{exp}^i$ . The particle hypothesis and momentum also affect the Cherenkov photon distribution. These parameters modify the shape of the time likelihood density since in reality not all photons are emitted at the midpoint of the track. As with the charge likelihood, the contributions from both the direct and scattered light to the time likelihood density are calculated separately, which are both calculated from particle gun studies.

The track parameters and particle identity which maximise  $L(\Gamma, \vec{\theta})$  are defined as the best-fit parameters. In practice MINUIT [182] is used to minimise the value of  $-\ln L(\Gamma, \vec{\theta})$ . The `fitQun` algorithm considers an electron-like, muon-like, and charged pion-like hypothesis for events with a single final state particle, denoted “single-ring events”. The particle’s identity is determined by taking the ratio of the likelihood of each of the hypotheses. For instance, electrons and muons are distinguished by considering the value of  $\ln(L(e, \vec{\theta}_e)/L(\mu, \vec{\theta}_\mu))$  in comparison to the reconstructed momentum of the electron hypothesis [180]. This distance from this criteria is termed the PID parameter and is illustrated in Figure 5.4.

The `fitQun` algorithm also considers a  $\pi^0$  hypothesis. To do this, it performs a fit looking for two standard electron-hypothesis tracks which point to the same four-vertex. This assumes the electron tracks are generated from photon-conversion so the electron tracks actually appear offset from the proposed  $\pi^0$  vertex. For these fits, the conversion length, direction, and momenta of each photon are also considered as track

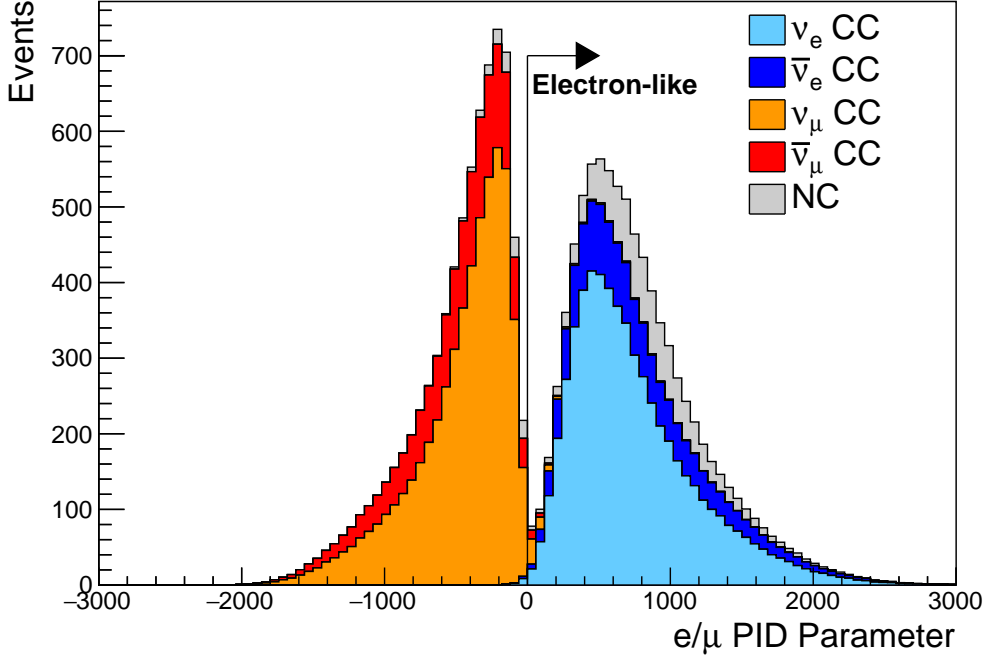


**Figure 5.4:** The electron/muon PID separation parameter for all sub-GeV single-ring events in SK-IV. The charged current (CC) component is broken down in four flavours of neutrino ( $\nu_\mu$ ,  $\bar{\nu}_\mu$ ,  $\nu_e$  and  $\bar{\nu}_e$ ). Events with positive values of the parameter are determined to be electron-like.

parameters which are then fit in the same methodology as the standard single-ring hypotheses.

Whilst low energy events are predominately single-ring events, higher energy neutrino events can generate final states with multiple particles which generate Cherenkov photons. These “multi-ring” hypotheses are also considered in the `fitQun` algorithm. When calculating the charge likelihood density, the predicted charge associated with each ring is calculated separately and then merged to calculate the total accumulated charge on each PMT. Similarly, the time likelihood for the multi-ring hypothesis is calculated assuming each ring is independent. Each track is time-ordered based on the time of flight from the center of the track to the PMT and the direct light from any ring incident on the PMT is assumed to arrive before any scattered light. To reduce computational resources, the multi-ring fits only consider electron-like and

1502 charged pion-like rings as the pion fit can be used as a proxy for a muon fit due to  
1503 their similar mass.

1504 Multi-ring fits proceed by proposing another ring to the previous fit and then  
1505 fitting the parameters in the method described above. Typically, multi-ring fits have  
1506 the largest likelihood because of the additional degrees of freedom introduced. Conse-  
1507 quently, the additional ring is only added if the ratio of likelihoods passes a criterion,  
1508 which is determined by Monte Carlo studies.

1509 As an example of how the reconstruction depends on the detector conditions, the  
1510 author of this thesis assessed the quality of event reconstruction for SK-V data. The  
1511 detector systematics invoked within the T2K-only oscillation analysis are determined  
1512 using data to Monte Carlo comparisons using the SK-IV data [183]. Due to tank-open  
1513 maintenance occurring between SK-IV and SK-V, the dark rate of each PMT was  
1514 observed to increase in SK-V due to light exposure for a significant time during the  
1515 repairs. This increase can be seen in Figure 5.5. Run-10 of the T2K experiment was  
1516 conducted in the SK-V period, so the consistency of SK-IV and SK-V data needs to  
1517 be studied to determine whether the SK-IV-defined systematics can be applied to the  
1518 run-10 data. This comparison study was performed using the stopping muon data set  
1519 for both the SK-IV and SK-V periods. This data sample is used due to the high rate of  
1520 interactions ( $O(200)$  events per hour) as well as having similar energies to muons from  
1521 CCQE  $\nu_\mu$  interactions from beam interactions. The rate of cosmic muons does depend  
1522 on the solar activity cycle [184] but has been neglected in this comparison study. This  
1523 is because the shape of the distributions is most important for the purposes of being  
1524 compared to the detector systematics. The SK-IV and SK-V data samples consist of  
1525 2398.42 and 626.719 hours of data which equates to 686k and 192k events respectively.

1526 The predicted charge calculated in the `fitQun` charge likelihood prediction includes  
1527 a contribution from the photoelectron emission due to dark noise. Therefore, the

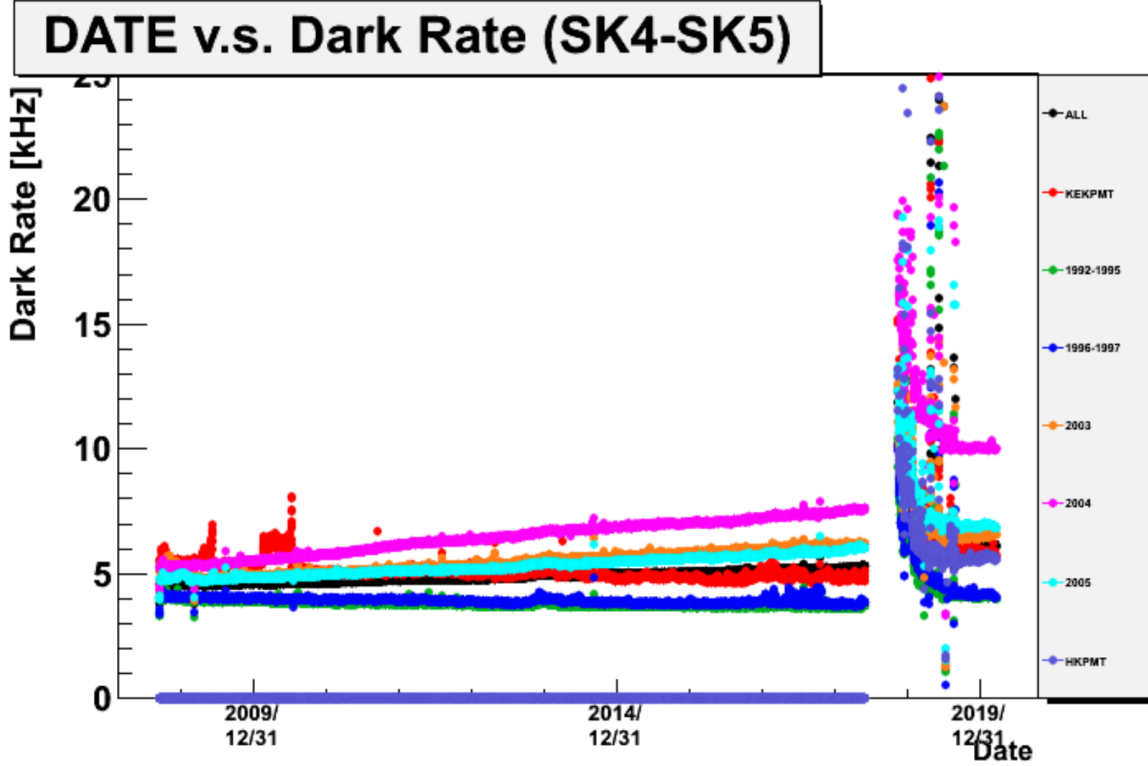


**Figure 5.5:** The variation of the measured dark rate as a function of date, broken down by PMT type. The SK-IV and SK-V periods span September 2008 to May 2018 and January 2019 to July 2020, respectively. The break in measurement in 2018 corresponds to the period of tank repair and refurbishment. Figure adapted from [183].

increase in the SK-V dark rate needs to be accounted for. In practice, the average dark rate in each SK period is calculated and used as an input in the reconstruction. This is calculated by averaging the dark rate per run for each period separately, using the calibration measurements detailed in subsection 3.1.2. The average dark rate from SK-IV and SK-V were found to be 4.57kHz and 6.30kHz, respectively. The associated charge with the muon and decay electron subevents are illustrated in Figure 5.6. The photoelectron emission from dark noise will be more noticeable for events that have lower energy. This is because this contribution becomes more comparable to the number of photoelectrons emitted from incident photons in low-energy events. This behaviour is observed in the data, where the charge deposited by the muon subevent

1538 is mostly unaffected by the increase in dark rate, whilst the charge associated with the  
 1539 decay-electron is clearly affected.

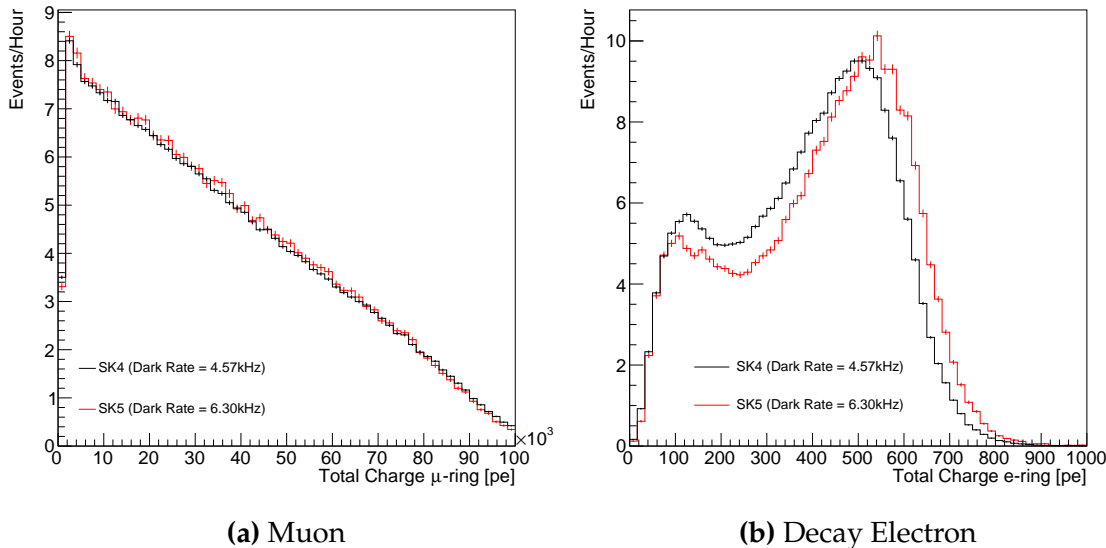


**Figure 5.6:** Comparison of the measured raw charge deposited per event from the stopping muon data samples between SK-IV (Blue) and SK-V (Red), split by the primary muon subevent and the associated decay electron subevent.

1540 The energy scale systematic for the SK-IV period was determined to be 2.1% [185].  
 1541 It is defined to be equal to the difference between data and Monte Carlo prediction  
 1542 in the stopping muon data sample. To determine the consistency of the SK-IV and  
 1543 SK-V with respect to the energy scale systematic, the muon momentum distribution is  
 1544 compared between the two SK periods. As the total number of Cherenkov photons  
 1545 is integrated across the track length, the reconstructed momentum divided by track  
 1546 length (or range) is compared between SK-IV and SK-V as illustrated in Figure 5.7.

1547 The consistency between these distributions has been computed in two ways.  
 1548 Firstly, a Gaussian is fit to each distribution separately. The mean of which is found to  
 1549 be  $(2.272 \pm 0.003)\text{MeV/cm}$  and  $(2.267 \pm 0.006)\text{MeV/cm}$  for SK-IV and SK-V respec-  
 1550 tively. The ratio of these is equal to  $1.002 \pm 0.003$ . The mean of the Gaussian fits are  
 1551 consistent with the expected stopping power of a minimum ionising muon for a target

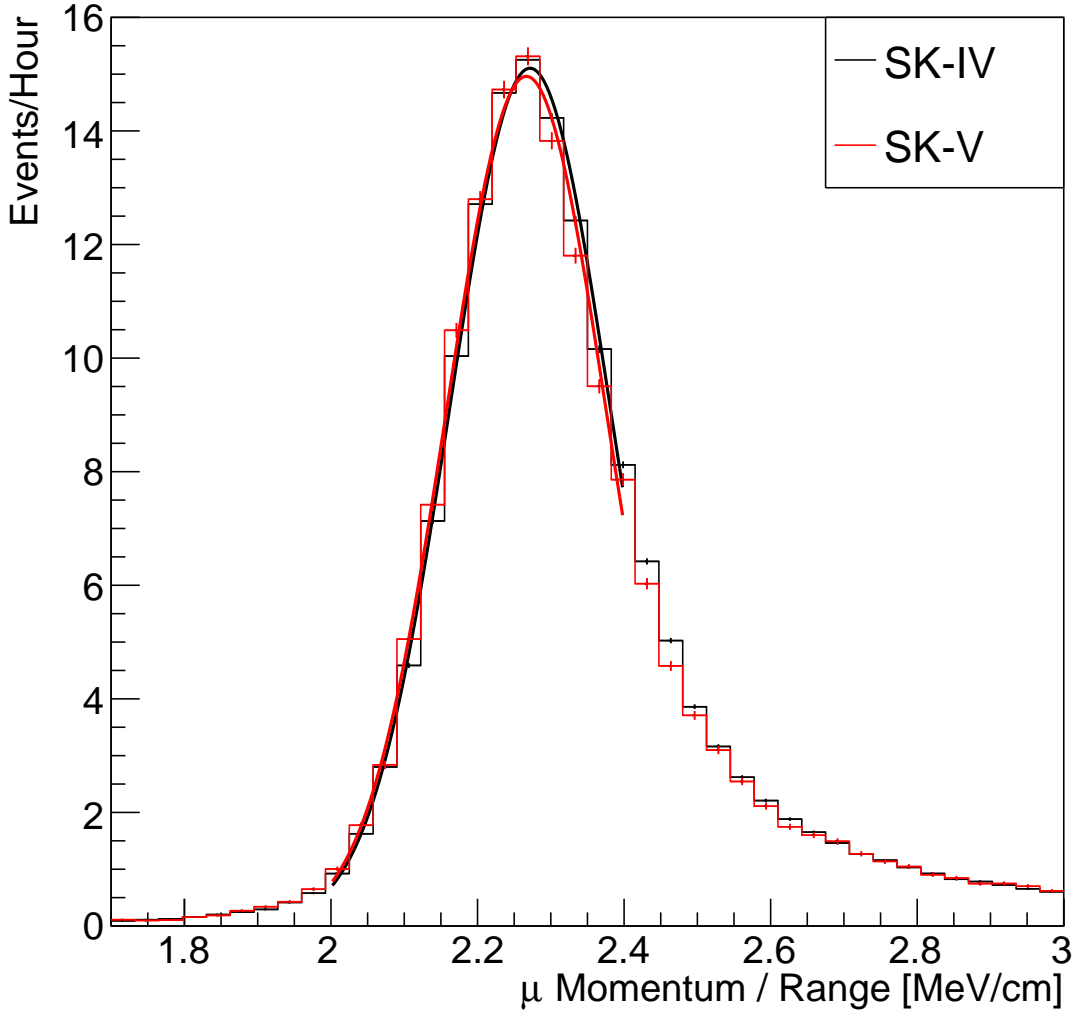


**Figure 5.7:** The distribution of the reconstructed momentum from the muon ring divided by the distance between the reconstructed muon and decay electron vertices as found in the stopping muon data sets of SK-IV (Black) and SK-IV (Red). Only events with one tagged decay electron are considered. A Gaussian fit is considered in the range [2.0, 2.4] MeV/cm and illustrated as the solid curve.

material (water) with  $Z/A \sim 0.5$  [186]. The second consistency check is performed by introducing a nuisance parameter,  $\alpha$ , which modifies the SK-V distribution. The value of  $\alpha$  which minimises the  $\chi^2$  value between the SK-IV and SK-V is determined by scanning across a range of values. This is repeated by applying the nuisance parameter as both a multiplicative factor and an additive shift. The  $\chi^2$  distributions for different values of  $\alpha$  is illustrated in Figure 5.8. The values which minimise the  $\chi^2$  are found to

- <sub>1558</sub> be 0.0052 and 1.0024 for the additive and multiplicative implementations, respectively.  
<sub>1559</sub> No evidence of shifts larger than the 2.1% uncertainty on the energy scale systematic  
<sub>1560</sub> has been found in the reconstructed momentum distribution of SK-IV and SK-V.

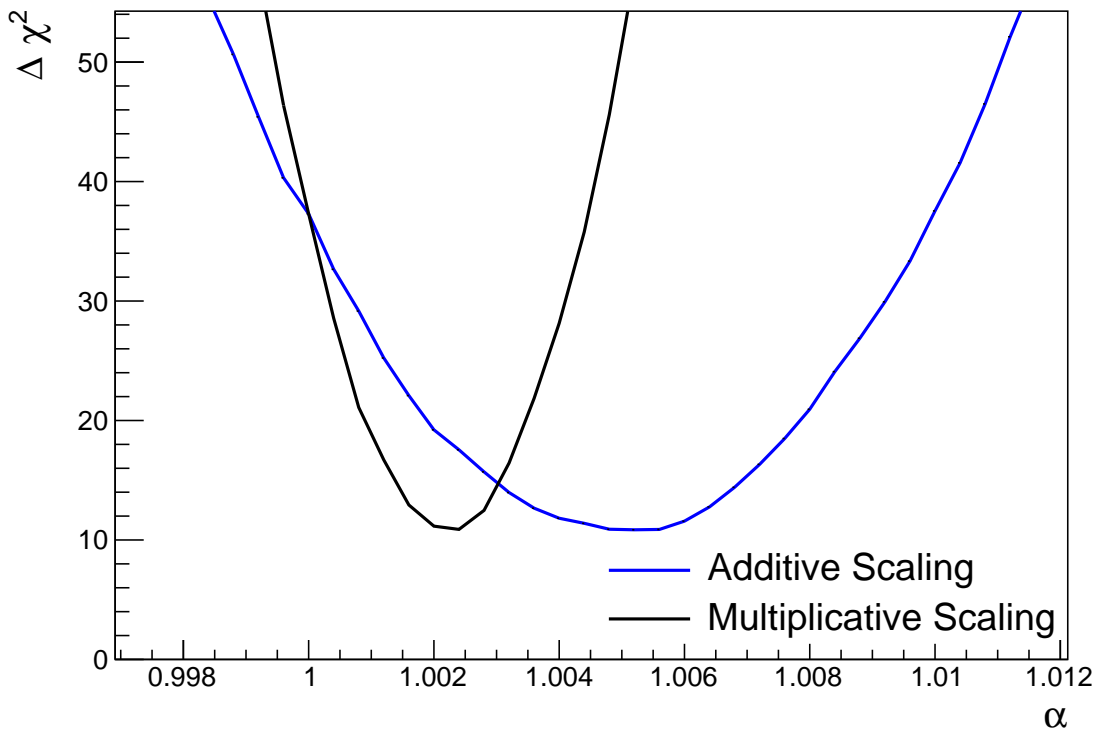


**Figure 5.8:** The  $\chi^2$  difference between the SK-IV and SK-V reconstructed muon momentum divided by range when the SK-V is modified by the scaling parameter  $\alpha$ . Both additive (Blue) and multiplicative (Black) scaling factors have been considered. In practice, the additive scaling factor actually uses the value of  $(\alpha - 1.0)$  but is illustrated like this so the results can be shown on the same axis range.

### <sub>1561</sub> 5.3 Event Reduction at SK

- <sub>1562</sub> Atmospheric neutrino events observed in the SK detector are categorised into three  
<sub>1563</sub> different types of samples: fully contained (FC), partially contained (PC) and up-  
<sub>1564</sub> going muon (Up- $\mu$ ), using PMT hit signatures in the inner and outer detector (ID  
<sub>1565</sub> and OD, respectively). To identify FC neutrino events, it is required that the neutrino

1566 interacts inside the fiducial volume of the ID such that no significant OD activity is  
 1567 observed. For this analysis, an event is defined to be in the fiducial volume providing  
 1568 the event vertex is at least 0.5m away from the ID walls. PC events have the same  
 1569 ID requirements but can have a larger signal present inside the OD. Typically these  
 1570 events are higher energy muon interactions that penetrate the ID walls. The Up- $\mu$   
 1571 sample contains events where muons are created from neutrino interactions in the  
 1572 OD water or rock below the tank. They then propagate upwards through the detector.  
 1573 The reason downward-going muons generated from neutrino interactions above the  
 1574 tank are neglected is due to the difficulty in separating their signature from the cosmic  
 1575 muon shower background. The sample categories are visually depicted in Figure 5.9.

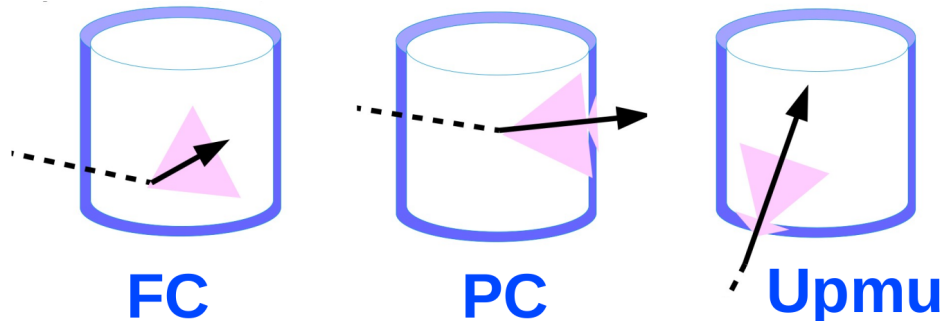


**Figure 5.9:** A depiction of the topology patterns for fully-contained (FC), partially-contained (PC) and up-going muon (Up- $\mu$ ) samples included in this analysis.

1576 Based on the event characteristics, as defined by the `fitQun` event reconstruction  
 1577 software, the FC events are categorised by

- 1578     • **Visible Energy:** equal to the sum of the reconstructed kinetic energy above the  
 1579       Cerenkov threshold for all rings present in the event. The purpose is to separate  
 1580       events into sub-GeV and multi-GeV categories.
- 1581     • **Number of observed Cerenkov rings.** The purpose is to separate single-ring and  
 1582       multi-ring events, where single-ring events predominantly consist of quasi-elastic  
 1583       interactions and multi-ring events are typically resonant pion production or deep  
 1584       inelastic scattering events.

- 1585     • **Particle identification parameter of the most energetic ring:** A value deter-  
1586         mined from the maximum likelihood value based on `fitQun`'s electron, muon, or  
1587         pion hypothesis. The purpose is to separate electron-like and muon-like events.
  
- 1588     • **Number of decay electrons:** The purpose is to separate quasi-elastic events  
1589         (which have one decay electron emitted from the muon decay) and resonant pion  
1590         production events (which have two decay electrons emitted from the muon and  
1591         pion).

1592     The PC and Up- $\mu$  categories are broken down into “through-going” and “stopping”  
1593     samples depending on whether the muon left the detector. This is because the stopping  
1594     events deposit the entire energy of the interaction into the detector, resulting in better  
1595     reconstruction. The energy of events that exit the detector has to be estimated which  
1596     introduces much larger systematic uncertainties. Through-going Up- $\mu$  samples are  
1597     further broken down by whether any hadronic showering was observed in the event  
1598     which typically indicates DIS interactions. The expected neutrino energy for the  
1599     different categories is given in Figure 5.10. FC sub-GeV and multi-GeV events peak  
1600     around 0.7GeV and 3GeV respectively, with slightly different peak energies for  $\nu_x \rightarrow \nu_e$   
1601     and  $\nu_x \rightarrow \nu_\mu$  oscillation channels. PC and Up- $\mu$  are almost entirely comprised of  
1602      $\nu_x \rightarrow \nu_\mu$  events and peak around 7GeV and 100GeV, respectively.

1603     In normal data-taking operations, the SK detector observes many background  
1604     events alongside the beam and atmospheric neutrino signal events of physics interest.  
1605     Cosmic ray muons and flasher events, which are the spontaneous discharge of a given  
1606     PMT, contribute the largest amount of background events in the energy range relevant  
1607     to any analysis searching for neutrino events. Lower energy analyses like DSNB  
1608     searches are also subject to radioactive backgrounds [187]. Therefore the data recorded  
1609     is reduced with the aim of removing these background events. The reduction process  
1610     is detailed in [47, 89] and briefly summarised below.

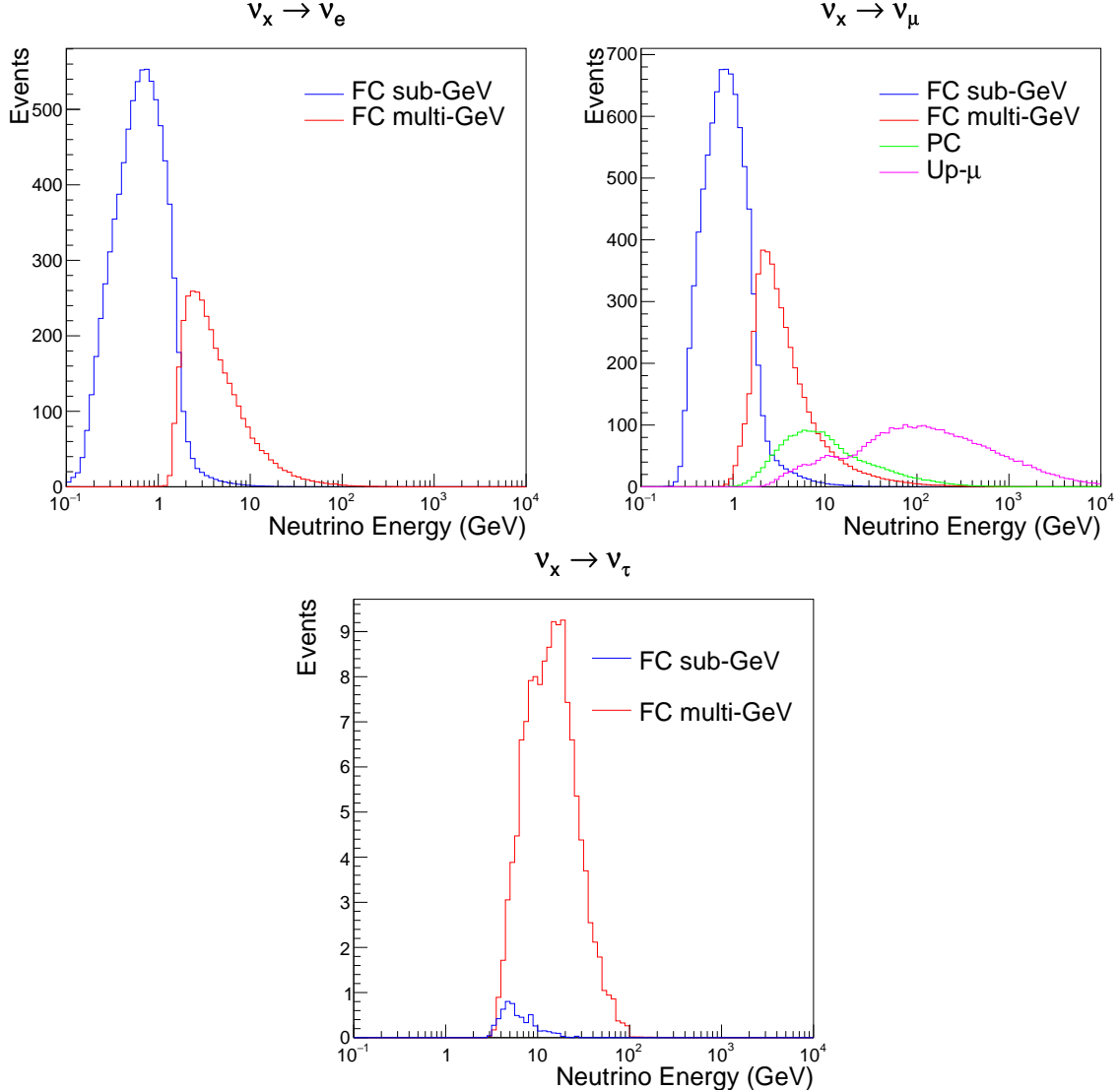


**Figure 5.10:** The predicted neutrino flux of the fully contained (FC) sub-GeV and multi-GeV, partially contained (PC), and upward-going muon (Up- $\mu$ ) events. The prediction is broken down by the  $\nu_x \rightarrow \nu_e$  prediction (top left),  $\nu_x \rightarrow \nu_\mu$  prediction (top right) and  $\nu_x \rightarrow \nu_\tau$  prediction (bottom). All systematic dials are set to their nominal values and the Asimov A oscillation parameters are assumed.

1611        The first two steps in the FC reconstruction remove the majority of cosmic ray  
 1612        muons by requiring a significant amount of ID activity compared to that measured in  
 1613        the OD. Events that pass this cut are typically very high momentum muons or events  
 1614        that leave very little activity in the OD. Consequently, a third reduction step is then  
 1615        applied to select cosmic-ray muons that pass the initial reduction step. A purpose-built  
 1616        cosmic muon fitter is used to determine the entrance (or exit) position of the muon and

1617 a cut is applied to OD activity contained within 8m of this position. Flasher events are  
1618 removed in the fourth reduction step which is based on the close proximity of PMT  
1619 hits surrounding the PMT producing the flash. Events that pass all these reduction  
1620 steps are reconstructed with the APFit algorithm. The fifth step of the reduction uses  
1621 information from the more precise fitter to repeat the previous two steps with tighter  
1622 cuts. Muons below the Cherenkov threshold can not generate optical photons in the  
1623 ID but the associated decay electron can due to its lower mass. These are the types of  
1624 events targeted in the fifth reduction step. The final cuts require the event vertex to be  
1625 within the fiducial volume (0.5m from the wall although the nominal distance is 2.0m),  
1626 visible energy  $E_{vis} > 30\text{MeV}$  and fewer than 16 hits within the higher energy OD  
1627 cluster. The culmination of the fully contained reduction results in 8.09 events/day in  
1628 the nominal fiducial volume [188]. The uncertainty in the reconstruction is calculated  
1629 by comparing Monte Carlo prediction to data. The largest discrepancy is found to be  
1630 1.3% in the fourth reduction step.

1631 The PC and Up- $\mu$  events are processed through their own reduction processes  
1632 detailed in [47]. Both of these samples are reconstructed with the APFit algorithm  
1633 rather than fitQun. This is because the efficiency of reconstructing events that leave  
1634 the detector has not been sufficiently studied for reliable systematic uncertainties. The  
1635 PC and Up- $\mu$  samples attain events at approximately 0.66 and 1.44 events/day.

1636 Events due to beam neutrinos undergo the same reduction steps as FC events and  
1637 are then subject to further cuts [189]. The GPS system which links the timing between  
1638 the beam facility and SK needs to be operating correctly and there should be no activity  
1639 within the detector in the previous  $100\mu\text{s}$  before the trigger. The events then need to  
1640 triggered between  $-2\mu\text{s}$  and  $10\mu\text{s}$  of the expected spill timing.

<sub>1641</sub> **Chapter 6**

<sub>1642</sub> **Oscillation Probability Calculation**

<sub>1643</sub> It is important to understand how and where the sensitivity to the oscillation pa-  
<sub>1644</sub> rameters comes from for both atmospheric and beam samples. An overview of how  
<sub>1645</sub> these samples observe changes in  $\delta_{CP}$ ,  $\Delta m_{23}^2$ , and  $\sin^2(\theta_{23})$  is given in section 6.1. It  
<sub>1646</sub> also explains the additional complexities involved when performing an atmospheric  
<sub>1647</sub> neutrino analysis as compared to a beam-only analysis.

<sub>1648</sub> Without additional techniques, atmospheric sub-GeV upward-going neutrinos  
<sub>1649</sub> ( $E_\nu < 1.33\text{GeV}, \cos(\theta_Z) < 0.$ ) can artificially inflate the sensitivity to  $\delta_{CP}$  due to the  
<sub>1650</sub> quickly varying oscillation probability in this region. Therefore, a “sub-sampling”  
<sub>1651</sub> approach has been developed to reduce these biases ensuring accurate and reliable  
<sub>1652</sub> sensitivity measurements. This technique ensures that small-scale unresolvable fea-  
<sub>1653</sub> tures of the oscillation probability have been averaged over whilst the large-scale  
<sub>1654</sub> features in the oscillation probability are unaffected. The documentation and valida-  
<sub>1655</sub> tion of this technique are found in section 6.2. The oscillation probability calculation is  
<sub>1656</sub> computationally intensive due to the large number of matrix multiplications needed.  
<sub>1657</sub> Consequently, the CUDAProb3 implementation choice made within the fitting frame-  
<sub>1658</sub> work, as detailed in section 6.3, ensures that the analysis can be done in a timely  
<sub>1659</sub> manner.

<sub>1660</sub> Whilst the beam neutrinos are assumed to propagate through a constant density  
<sub>1661</sub> slab of material, the density variations through the Earth result in more complex  
<sub>1662</sub> oscillation patterns. Furthermore, the uncertainty in the electron density can modify  
<sub>1663</sub> the oscillation probability for the denser core layers of the Earth. The model of the

1664 Earth used within this analysis is detailed in section 6.4. This includes information  
1665 about the official SK-only methodology as well as improvements that can be made  
1666 to remove some of the approximations made in that analysis. Another complexity of  
1667 atmospheric neutrinos oscillation studies is that the height of production in the atmo-  
1668 sphere is not known on an event-by-event basis. An analytical averaging technique  
1669 that approximates the uncertainty of the oscillation probability has been followed,  
1670 with the author of this thesis being responsible for the implementation and validation.  
1671 This implementation of an external technique is illustrated in section 6.5.

## 1672 6.1 Overview

1673 The analysis presented within this thesis focuses on the determination of oscillation  
1674 parameters from atmospheric and beam neutrinos. Whilst subject to the same oscil-  
1675 lation formalism, the way in which the two samples have sensitivity to the different  
1676 oscillation parameters differs quite significantly.

1677 Atmospheric neutrinos have a varying baseline, or “path length”,  $L$ , such that  
1678 the distance each neutrino travels before interacting is dependent upon the zenith  
1679 angle,  $\theta_Z$ . As primary cosmic rays can interact anywhere between the Earth’s surface  
1680 and  $\sim 50\text{km}$  above that, the height,  $h$ , in the atmosphere at which the neutrino was  
1681 generated also affects the path length,

$$L = \sqrt{(R_E + h)^2 - R_E^2 (1 - \cos^2(\theta_Z))} - R_E \cos(\theta_Z). \quad (6.1)$$

1682 Where  $R_E = 6,371\text{km}$  is the Earth’s radius. Consequently, the oscillation probabil-  
1683 ity is dependent upon two parameters,  $\cos(\theta_Z)$  and  $E_\nu$ .

1684 The oscillation probability used within this analysis is based on [21]. The neutrino  
1685 wavefunction in the vacuum Hamiltonian evolves in each layer of constant matter  
1686 density via

$$i\frac{d\psi_j(t)}{dt} = \frac{m_j^2}{2E_\nu}\psi_j(t) - \sum_k \sqrt{2}G_F N_e U_{ej} U_{ke}^\dagger \psi_k(t), \quad (6.2)$$

1687 where  $m_j^2$  is the square of the  $j^{th}$  vacuum eigenstate mass,  $E_\nu$  is the neutrino  
1688 energy,  $G_F$  is Fermi's constant,  $N_e$  is the electron number density and  $U$  is the PMNS  
1689 matrix. The transformation  $N_e \rightarrow -N_e$  and  $\delta_{CP} \rightarrow -\delta_{CP}$  is applied for antineutrino  
1690 propagation. Thus, a model of the Earth's density is required for atmospheric neutrino  
1691 propagation. Following the official SK-only methodology [190], this analysis uses the  
1692 Preliminary Reference Earth Model (PREM) [191]. This model provides piecewise cubic  
1693 polynomials as a function of the Earth's radius which results in the density profile  
1694 illustrated in Figure 6.1. As discussed, the propagator requires layers of constant  
1695 density. The SK methodology approximates the PREM model by using four layers of  
1696 constant density [190]. The details of these layers are detailed in Table 6.1.

Layer	Outer Radius [km]	Density [g/cm <sup>3</sup> ]	Chemical composition (Z/A)
Inner Core	1220	13	$0.468 \pm 0.029$
Outer Core	3480	11.3	$0.468 \pm 0.029$
Lower Mantle	5701	5.0	0.496
Transition Zone	6371	3.3	0.496

**Table 6.1:** Description of the four layers of the Earth invoked within the constant density approximation of the PREM model [191].

1697 The atmospheric neutrino oscillation probabilities can be presented as two dimensional  
1698 “oscillograms” as illustrated in Figure 6.2. The distinct discontinuities, as a

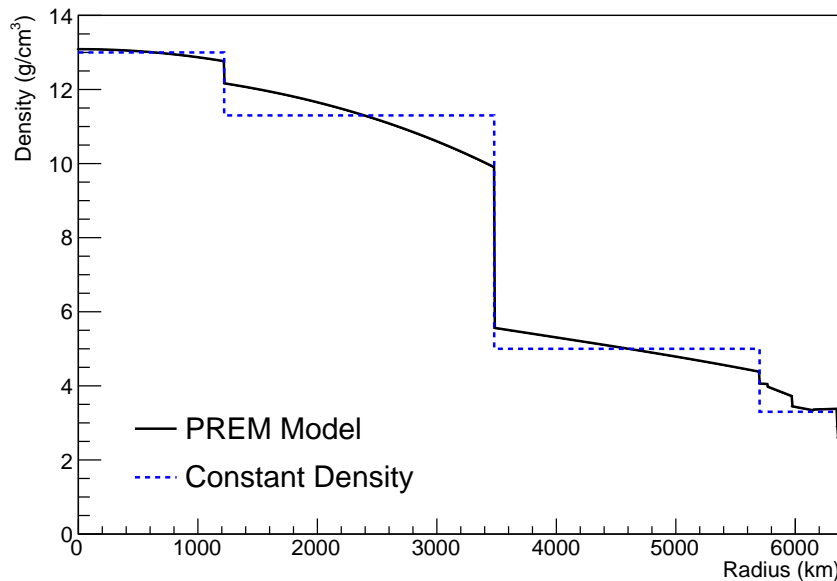


**Figure 6.1:** The density of the Earth given as a function of the radius, as given by the PREM model (Black), and the constant density four-layer approximation (Blue), as used in the official SK-only analysis.

function of  $\cos(\theta_Z)$ , are due to the discrete change in density invoked within the PREM model.

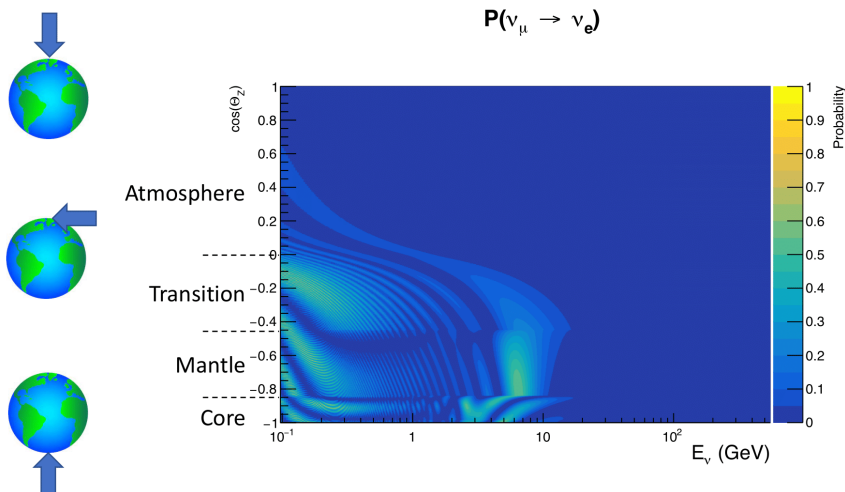


**Figure 6.2:** An “oscillogram” that depicts the  $P(\nu_\mu \rightarrow \nu_e)$  oscillation probability as a function of neutrino energy and cosine of the zenith angle. The zenith angle is defined such that  $\cos(\theta_Z) = 1.0$  represents neutrinos that travel from directly above the detector. The four-layer constant density PREM model approximation is used and Asimov A oscillation parameters are assumed (Table 2.2).

1701 Atmospheric neutrinos do have sensitivity to  $\delta_{CP}$  through a normalisation term.  
 1702 Figure 6.3 illustrates the difference in oscillation probability between CP-conserving  
 1703 ( $\delta_{CP} = 0.$ ) and a CP-violating ( $\delta_{CP} = -1.601$ ) value taken from Asimov A oscillation  
 1704 parameter set (Table 2.2). The result is a complicated oscillation pattern in the appear-  
 1705 ance probability for sub-GeV upgoing neutrinos. The detector does not have sufficient  
 1706 resolution to resolve these individual patterns so the sensitivity to  $\delta_{CP}$  for atmospheric  
 1707 neutrinos comes via the overall normalisation of these events.

1708 The presence of matter means that the effect  $\delta_{CP}$  has on the oscillation probability  
 1709 is not equal between neutrinos and antineutrinos, which would be expected when  
 1710 propagating through a vacuum. This is further extenuated by the fact that SK can  
 1711 not distinguish neutrinos and antineutrinos well and that the cross-section neutrino  
 1712 interaction is larger than that for antineutrinos. Finally, sample selections (discussed  
 1713 in [DB: Link to selection chapter](#)) targeting different neutrino interaction modes result  
 1714 in an imbalance in the percentage of neutrinos to anti-neutrinos. This is because  
 1715 negatively charged pions from antineutrino interactions are more likely to be captured  
 1716 by a nucleus compared to a positively charged pion. All of these effects lead to  
 1717 a difference in the number of neutrinos detected compared to antineutrinos. This  
 1718 changes how the  $\delta_{CP}$  normalisation term is observed, resulting in a very complex  
 1719 sensitivity to  $\delta_{CP}$ .

1720 Atmospheric neutrinos are subject to matter effects as they travel through the dense  
 1721 matter in the Earth. The vacuum and matter oscillation probabilities for  $P(\nu_e \rightarrow \nu_e)$   
 1722 and  $P(\bar{\nu}_e \rightarrow \bar{\nu}_e)$  are presented in Figure 6.4, where the PREM model has been assumed.  
 1723 The oscillation probability for both neutrinos and antineutrinos is affected in the  
 1724 presence of matter. However, the resonance effects around  $O(5)$ GeV only occur for  
 1725 neutrinos in normal mass hierarchy and antineutrinos in inverse mass hierarchy. The

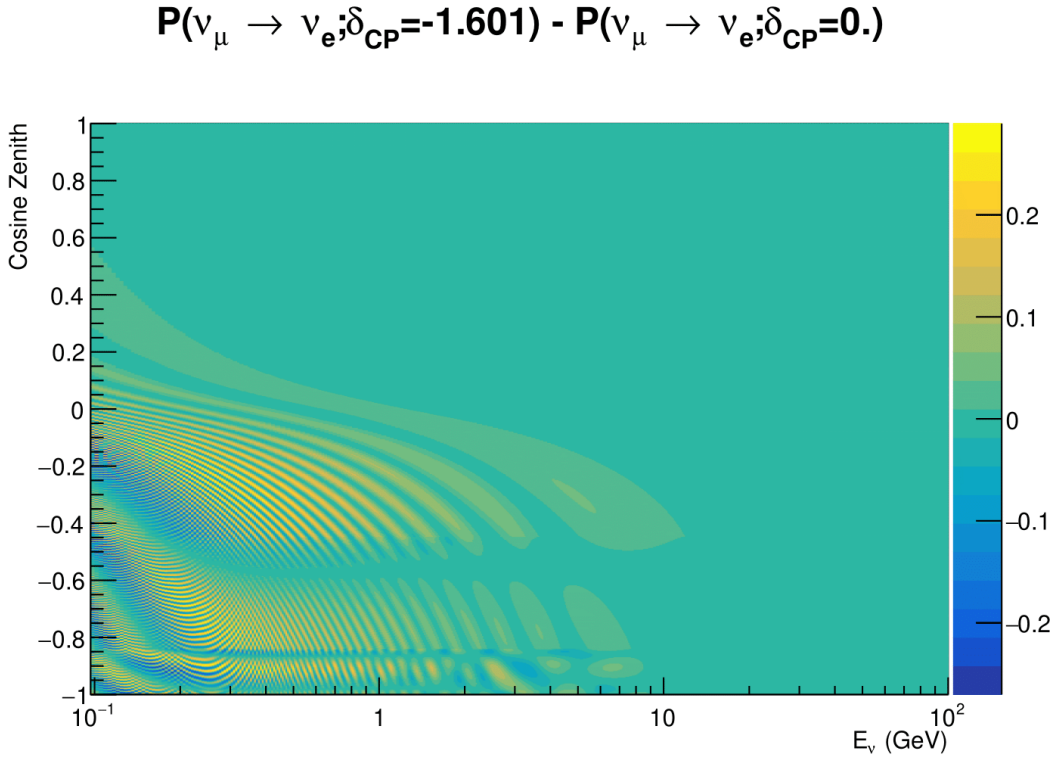


**Figure 6.3:** The effect of  $\delta_{CP}$  for atmospheric neutrinos given in terms of the neutrino energy and zenith angle. This oscillogram compares the  $P(\nu_\mu \rightarrow \nu_e)$  oscillation probability for a CP conserving ( $\delta_{CP} = 0.0$ ) and a CP violating ( $\delta_{CP} = -1.601$ ) value taken from the Asimov A parameter set. The other oscillation parameters assume the Asimov A oscillation parameter set given in Table 2.2.

1726 exact position and amplitude of the resonance depend on  $\sin^2(\theta_{23})$  meaning that the  
 1727 atmospheric neutrinos have sensitivity to  $\sin^2(\theta_{23})$ .

1728 As the T2K beam flux is centered at the first oscillation maximum ( $E_\nu = 0.6\text{GeV}$ ),  
 1729 the sensitivity to  $\delta_{CP}$  is predominantly observed as a change in the event-rate of e-like  
 1730 samples in  $\nu/\bar{\nu}$  modes. Figure 6.5 illustrates the  $P(\nu_\mu \rightarrow \nu_e)$  oscillation probability  
 1731 for a range of  $\delta_{CP}$  values. A circular modulation of the first oscillation peak (in both  
 1732 magnitude and position) is observed when varying throughout the allowable values  
 1733 of  $\delta_{CP}$ . The CP-conserving values of  $\delta_{CP} = 0, \pi$  have a lower(higher) oscillation  
 1734 maximum than the CP-violating values of  $\delta_{CP} = -\pi/2(\delta_{CP} = \pi/2)$ . A sub-dominant

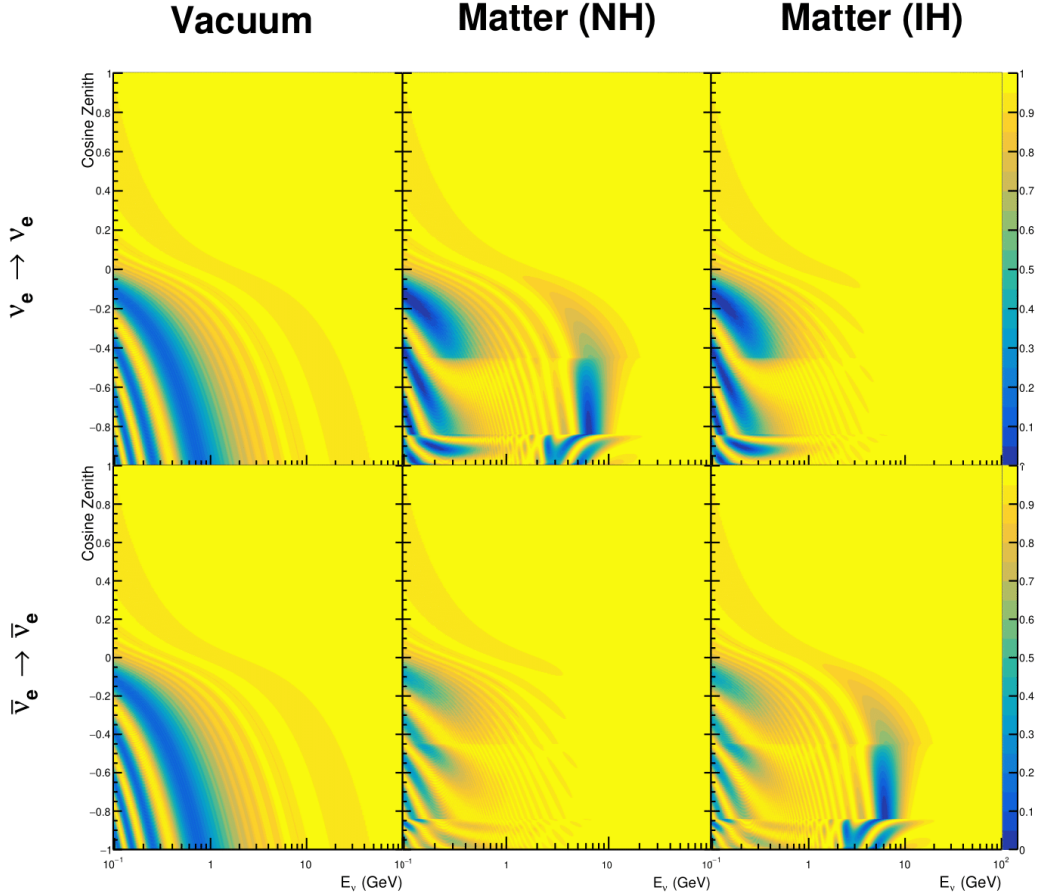


**Figure 6.4:** An illustration of the matter-induced effects on the oscillation probability, given as a function of neutrino energy and zenith angle. The top row of panels gives the  $P(\nu_e \rightarrow \nu_e)$  oscillation probability and the bottom row illustrates the  $P(\bar{\nu}_e \rightarrow \bar{\nu}_e)$  oscillation probability. The left column highlights the oscillation probability in a vacuum, whereas the middle and right column represents the oscillation probabilities when the four-layer fixed density PREM model is assumed. All oscillation probabilities assume the “Asimov A” set given in Table 2.2, but importantly, the right column sets an inverted mass hierarchy. The “matter resonance” effects at  $E_\nu \sim 5\text{GeV}$  can be seen in the  $P(\nu_e \rightarrow \nu_e)$  for normal mass hierarchy and  $P(\bar{\nu}_e \rightarrow \bar{\nu}_e)$  for inverted hierarchy.

<sub>1735</sub> shift in the energy of the oscillation peak is also present to aid in separating the two  
<sub>1736</sub> CP-conserving values of  $\delta_{CP}$ .

<sub>1737</sub> T2K’s sensitivity to the  $\sin^2(\theta_{23})$  and  $\Delta m_{23}^2$  is observed as a shape-based variation  
<sub>1738</sub> of the muon-like samples, as illustrated in Figure 6.5. The value of  $\Delta m_{32}^2$  laterally shifts  
<sub>1739</sub> the position of the oscillation dip (around  $E_\nu \sim 0.6\text{GeV}$ ) in the  $P(\nu_\mu \rightarrow \nu_\mu)$  oscillation

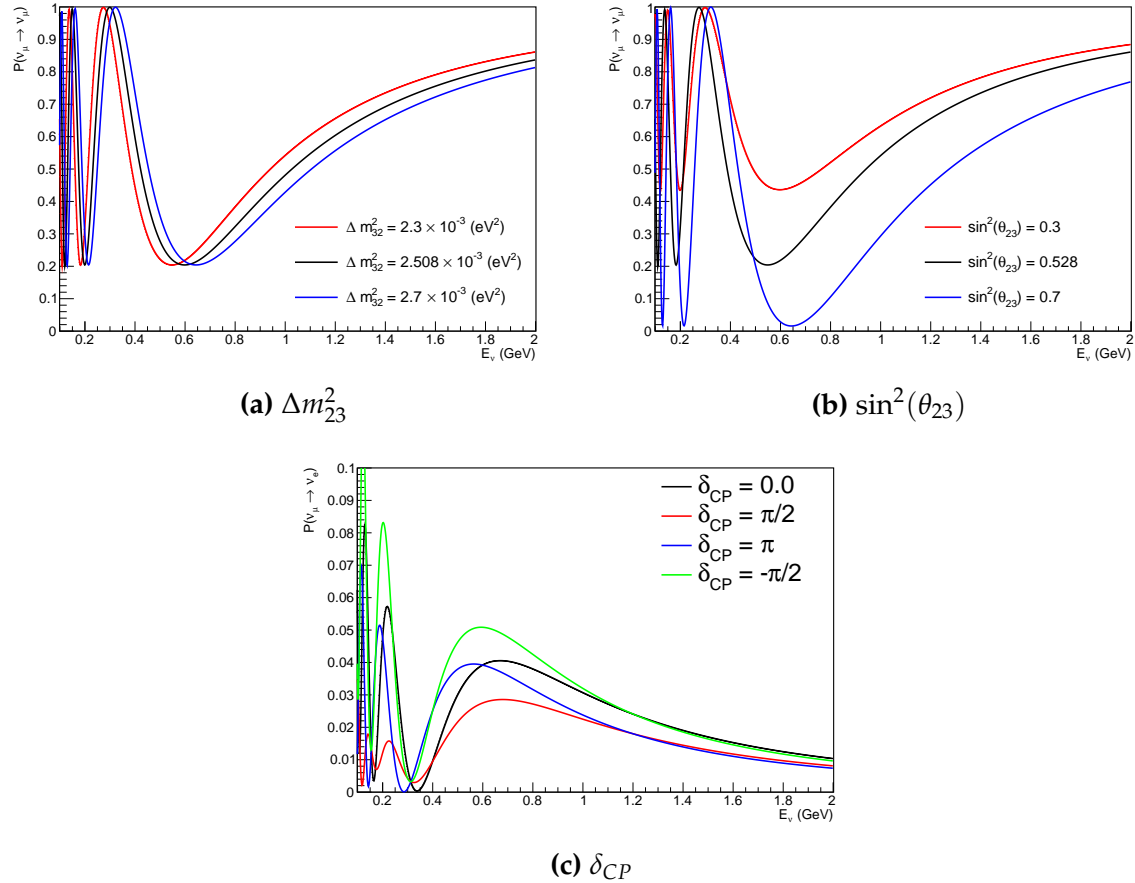


**Figure 6.5:** The oscillation probability for beam neutrino events given as a function of neutrino energy. All oscillation parameters assume the “Asimov A” set given in Table 2.2 unless otherwise stated. Each panel represents a change in one of the oscillation parameters whilst keeping the remaining parameters fixed.

1740 probability. A variation of  $\sin^2(\theta_{23})$  is predominantly observed as a vertical shift of  
 1741 the oscillation dip with second-order horizontal shifts being due to matter effects.  
 1742 The beam neutrinos have limited sensitivity to matter effects due to the relatively  
 1743 shorter baseline as well as the Earth’s mantle being a relatively low-density material  
 1744 (as compared to the Earth’s core). For some values of  $\delta_{CP}$ , the degeneracy in the  
 1745 number of e-like events allows the mass hierarchy to be resolved. This leads to a  $\delta_{CP}$   
 1746 -dependent mass hierarchy sensitivity which can be seen in Figure 6.6.

1747 Whilst all oscillation channels should be included for completeness, the computa-  
 1748 tional resources required to run a fit are limited and any reasonable approximations

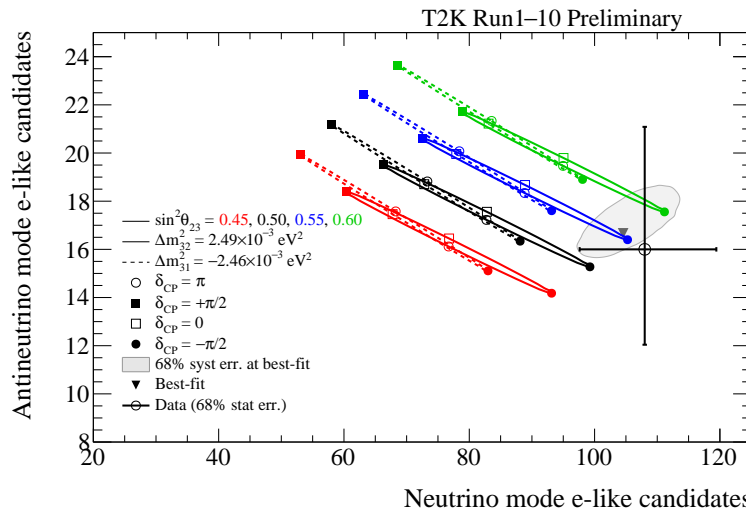


**Figure 6.6:** The number of electron-like events in the FHC and RHC operating mode of the beam, as a function of the oscillation probabilities. Both normal hierarchy (Solid) and inverse hierarchy (Dashed) values of  $\Delta m_{23}^2$  are given.

1749 which reduce the number of oscillation probability calculations that need to be made  
 1750 should be applied. The  $\nu_e \rightarrow \nu_{e,\mu,\tau}$  (and antineutrino equivalent) oscillations can be  
 1751 ignored for beam neutrinos as the  $\nu_e/\bar{\nu}_e$  fluxes are approximately two orders of magni-  
 1752 tude smaller than the corresponding  $\nu_\mu/\bar{\nu}_\mu$  flux. Furthermore, as the peak neutrino  
 1753 energy of the beam is well below the threshold for charged current tau production  
 1754 ( $E_\nu = 3.5\text{GeV}$  [51], only a small proportion of the neutrinos produced in the beam have  
 1755 the required energy. For the few neutrinos that have sufficient energy, the oscillation  
 1756 probability is very small due to the short baseline. Whilst these approximations can  
 1757 be made for the beam neutrinos, the atmospheric flux of  $\nu_e$  is of the same order of  
 1758 magnitude as the  $\nu_\mu$  flux and the energy distribution of atmospheric neutrinos extends  
 1759 well above the tau production threshold.

<sub>1760</sub> **6.2 Treatment of Fast Oscillations**

<sub>1761</sub> As shown in Figure 6.7, atmospheric neutrino oscillations have a significantly more  
<sub>1762</sub> complex structure for upgoing neutrinos with energy below 1GeV. This is because the  
<sub>1763</sub>  $L/E$  dependence of the oscillation probability in this region induces rapid variations  
<sub>1764</sub> for small changes in  $L$  or  $E$ . As discussed in section 6.1, this is also the region in which  
<sub>1765</sub> atmospheric neutrinos have sensitivity to  $\delta_{CP}$ . In practice, the direction of the neutrino  
<sub>1766</sub> is inferred from the direction of the final state particles traveling in the detector, which  
<sub>1767</sub> can be poor for low-energy neutrino interactions. This creates a distinct difference  
<sub>1768</sub> from the beam neutrinos where the position of the source is very precisely known.

<sub>1769</sub> As a consequence of the unresolvable structure, an average oscillation probability  
<sub>1770</sub> is observed in the subGeV upgoing region. This creates a computational problem; A  
<sub>1771</sub> significantly large amount of Monte Carlo statistics would be required to accurately  
<sub>1772</sub> predict the number of events if Monte Carlo averaging was the only technique used.  
<sub>1773</sub> This section describes the ‘sub-sampling’ approach developed for this analysis and  
<sub>1774</sub> compares it to the methodology used within the SK-only analysis.

<sub>1775</sub> The official SK-only analysis uses the osc3++ oscillation parameter fitter [190].  
<sub>1776</sub> To perform the fast oscillation averaging, it uses a ‘nearest-neighbour’ technique.  
<sub>1777</sub> For a given neutrino event, the nearest twenty neighbours in reconstructed lepton  
<sub>1778</sub> momentum and zenith angle are found and a distribution of their neutrino energies is  
<sub>1779</sub> built. The RMS,  $\sigma$ , of this distribution is then used to compute an average oscillation  
<sub>1780</sub> probability for the given neutrino Monte Carlo event.

<sub>1781</sub> For the  $i^{th}$  event, the oscillation weight is calculated as

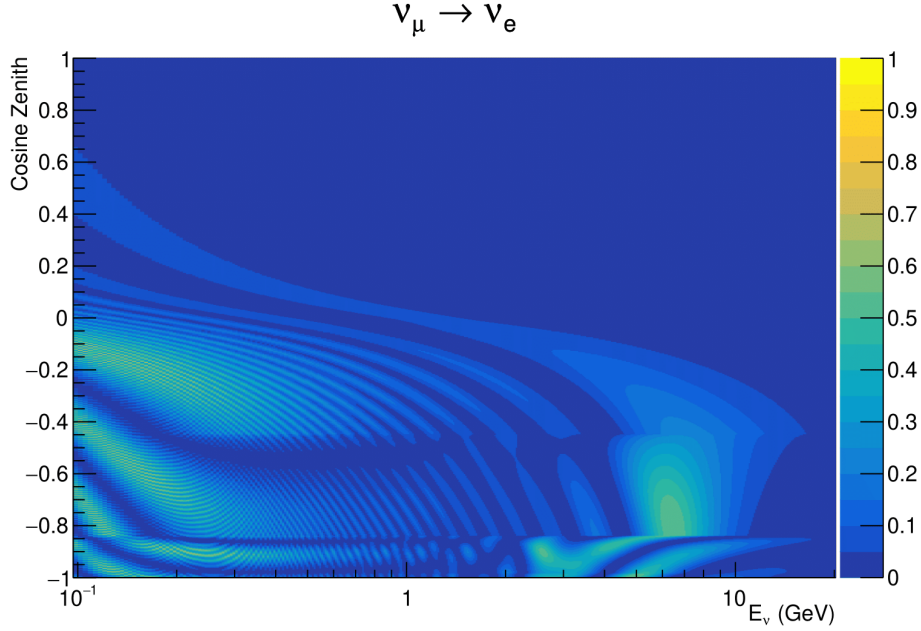


**Figure 6.7:** The oscillation probability  $P(\nu_\mu \rightarrow \nu_e)$ , given as a function of neutrino energy and zenith angle, which highlights an example of the “fast” oscillations in the sub-GeV upgoing region.

$$W_i = \frac{1}{5}P(E_i, \bar{L}_i) + \frac{1}{5} \sum_{\beta=-1,-0.5,0.5,1} P(E_i + \beta\sigma_i, L_\beta), \quad (6.3)$$

where  $P(E, L)$  is the oscillation probability calculation for neutrino energy  $E$  and path length  $L$  and the two path lengths,  $\bar{L}_i$  and  $L_\beta$  are discussed below. All of the oscillation probability calculations are performed with a fixed zenith angle such that the same density profile is used.

The uncertainty in the production height is controlled by using an “average” production height,  $\bar{L}_i$ , which represents the average path length computed using twenty production heights taken from the Honda flux model’s prediction [45]. For a given event, the production heights are sampled in steps of 5% of their cumulative distribution function.  $L_\beta$  values are similarly calculated but instead use different combinations of four production heights,

$$\begin{aligned}
 L_{-1.0} &= \frac{1}{4}L(45, 50, 55, 60), \\
 L_{-0.5} &= \frac{1}{4}L(35, 40, 65, 70), \\
 L_{+0.5} &= \frac{1}{4}L(25, 30, 75, 68), \\
 L_{+1.0} &= \frac{1}{4}L(15, 20, 85, 89).
 \end{aligned} \tag{6.4}$$

1792 This averaging technique works because of the inference between the zenith angle  
 1793 and the reconstructed direction of final state particles in the detector. For low-energy  
 1794 neutrinos, where the resolution of the true neutrino direction is poor,  $\sigma_i$  will be large,  
 1795 resulting in significant averaging effects. Contrary to this, the inferred direction of  
 1796 high-energy neutrinos will be much closer to the true value, meaning that  $\sigma_i$  will be  
 1797 smaller, culminating in small averaging effects.

1798 In practice, this technique is performed before the fit in order to deal with the  
 1799 computational cost. This is possible as the Osc3++ framework uses binned oscillation  
 1800 parameters rather than continuous so the oscillation parameters used in the fit are  
 1801 known prior to run-time. The framework used in this analysis uses continuous  
 1802 oscillation parameters, and due to the MCMC fitting technique, there is no way to  
 1803 know which oscillation parameter values will be selected *a priori*. Therefore, the  
 1804 oscillation parameter calculation has to be performed at run-time. Computing five  
 1805 oscillation probabilities per event would require far too many computational resources  
 1806 to be viable. Therefore SK technique can not be used within this analysis. However,  
 1807 the concept of the averaging technique can be taken from it.

1808 To perform a similar averaging as the SK analysis, a sub-sampling approach using  
 1809 binned oscillograms has been devised. The technique can be explained by considering  
 1810 a “fine” and “coarse” oscillogram. The fine oscillograms are used to define the array of

1811  $\cos(\theta_Z)$  and  $E_\nu$  used in the oscillation engine. The coarse oscillograms cover the same  
1812 phase-space but have fewer bins, where the value of a particular coarse bin is taken  
1813 as the linear average (flat prior in  $E_\nu$  and  $\cos(\theta_Z)$ ) of all fine bins which falls into it.  
1814 The coarse oscillogram is then used for determining the oscillation weight for a given  
1815 event. The binning which is used to calculate the oscillation probabilities, known as  
1816 the ‘fine’ binning, has  $N \times N$  subdivisions per coarse bin. Figure 6.8 illustrates the  
1817  $N = 2$  example where the assigned value to a coarse bin is the average of the four fine  
1818 bins which fall in that coarse bin. Whilst the coarse bin edges do not have to be linear  
1819 on either axis, the sub-division of the fine bins is linear over the range of a coarse bin.

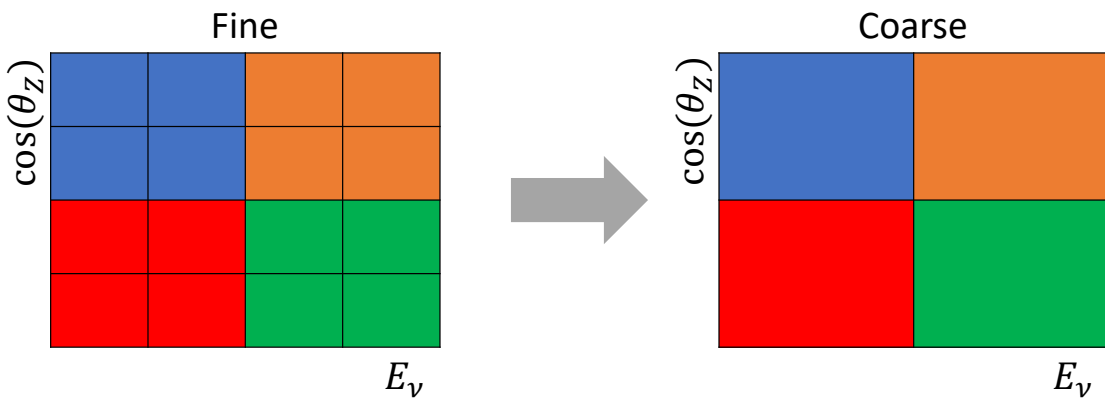


**Figure 6.8:** Illustration of the averaging procedure for  $N = 2$ . The oscillation probabilities calculated on the finer left binning are averaged to obtain the oscillation probabilities in the coarser right binning. These averaged oscillation probabilities with the coarser binning are then applied to each event during the fit.

1820 The coarse binning is defined with  $67 \times 52$  bins in true neutrino energy  $\times$  cosine  
1821 zenith. It is picked to be identical to that provided in [192]. In general, the binning is  
1822 logarithmically spaced in neutrino energy but has some hand-picked bin edges. Firstly,  
1823 the bin density around the matter resonance is smoothly increased around the matter  
1824 resonance region. This is to avoid smearing this region which can be well sampled by  
1825 the Monte Carlo. Secondly, bin edges are selected to hit  $0.4, 0.6, 1, 10, 30, 50, 100\text{GeV}$ .  
1826 This is to ensure that the Coulomb correction systematic and the atmospheric flux  
1827 systematics definitions in neutrino energy can be hit. The cosine zenith binning is

1828 approximately linearly spaced across the allowable range but the values of layer  
 1829 transitions are hit precisely:  $-0.8376$  (core-mantle) and  $-0.4464$  (mantle/transition  
 1830 zone). Bins are spread further apart for downgoing events as this is a region unaffected  
 1831 by the fast oscillation wavelengths and reduces the total number of calculations  
 1832 required to perform the calculation.

1833 The choice of  $N$  is justified based on two studies. Firstly, the variation of event rates  
 1834 of each sample is studied as a function of  $N$ . For a given set of oscillation parameters  
 1835 thrown from the PDG prior constraints (detailed in Table 2.1), the oscillation probabili-  
 1836 ties are calculated using a given value of  $N$ . Each sample is re-weighted and the event  
 1837 rate is stored. The value of  $N$  is scanned from 1, which corresponds to no averaging, to  
 1838 24, which corresponds to the largest computationally viable subdivision binning. The  
 1839 event rate of each sample at large  $N$  is expected to converge to a stationary value due  
 1840 to the fine binning fully sampling the small-scale structure. Figure 6.9 illustrates this  
 1841 behaviour for the SubGeV\_elike\_0dcy sample for 30 different throws of the oscillation  
 1842 parameters.

1843 Denoting the event rate for one sample for a given throw  $t$  at each  $N$  by  $\lambda_t^N$ , the  
 1844 average over all considered  $N$  values ( $\bar{\lambda}_t = \frac{1}{24} \sum_{N=1}^{24} \lambda_t^N$ ) is computed. The variance in  
 1845 the event rate at each  $N$  is then calculated as

$$\text{Var}[\lambda^N] = \frac{1}{N_{\text{throws}}} \sum_{t=1}^{N_{\text{throws}}} (\lambda_t^N - \bar{\lambda}_t)^2 - \left[ \frac{1}{N_{\text{throws}}} \sum_{t=1}^{N_{\text{throws}}} (\lambda_t^N - \bar{\lambda}_t) \right]^2. \quad (6.5)$$

1846 The aim of the study is to find the lowest value of  $N$  such that this variance is  
 1847 below 0.001. This is the typical threshold used by T2K fitters to validate systematic  
 1848 implementation so has been set as the same criteria. The results of this study for  
 1849 each atmospheric sample used within this thesis are illustrated in Figure 6.10 for

### SubGeV-elike-0dcy

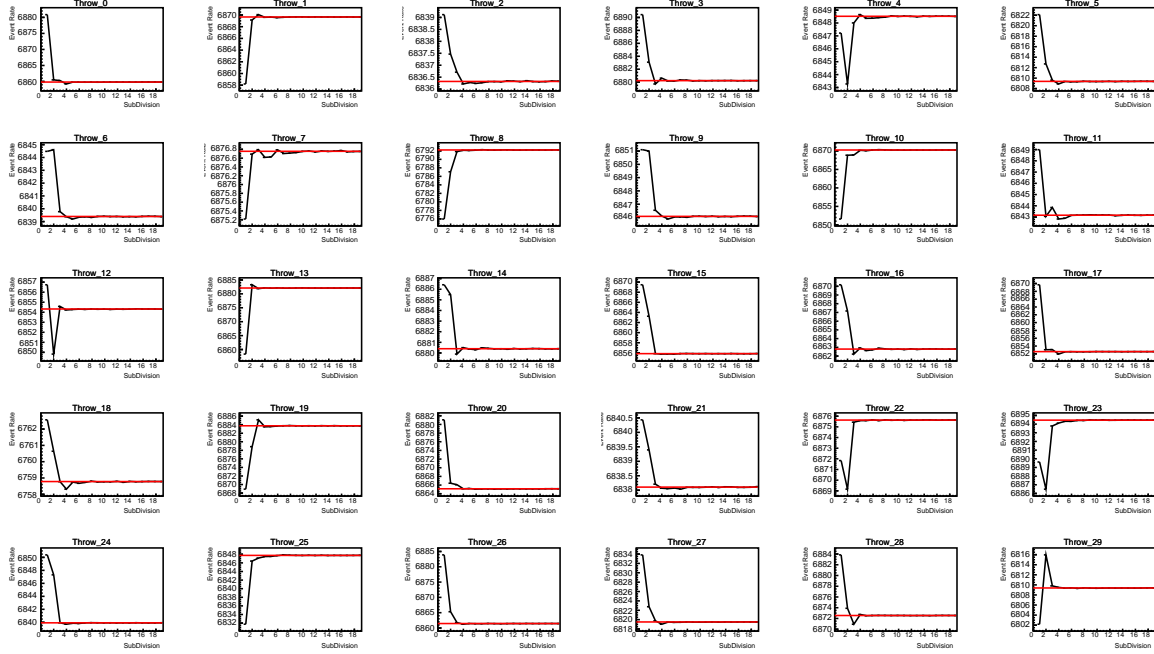


**Figure 6.9:** Event rate of the SubGeV\_elike\_0dcy sample as a function of the number of subdivisions per coarse bin. Each subplot represents the event rate of the sample at a different oscillation parameter set thrown from the PDG priors detailed in Table 2.1. The red line in each subplot represents the mean of the event rate over the different values of sub-divisions for that particular oscillation parameter throw.

1850 2000 throws of the oscillation parameters. As can be seen, the variance is below  
 1851 the threshold at  $N = 10$ , and is driven primarily by the SubGeV\_mulike\_1dcy and  
 1852 SubGeV\_elike\_0dcy samples.

1853 The second study to determine the value of  $N$  is as follows. The likelihood for each  
 1854 sample is computed against an Asimov data set created with Asimov A oscillation  
 1855 parameters (Table 2.2). Following Equation 6.5, the variance of the log-likelihood over  
 1856 all considered  $N$  is computed. The results are shown in Figure 6.11.

1857 A choice of  $N = 10$  sub-divisions per coarse bin has a variance in both event rate  
 1858 and log-likelihood residuals less than the required threshold of 0.001. The largest  
 1859 value of the likelihood variance is of order  $10^{-7}$ , corresponding to an error on the log-

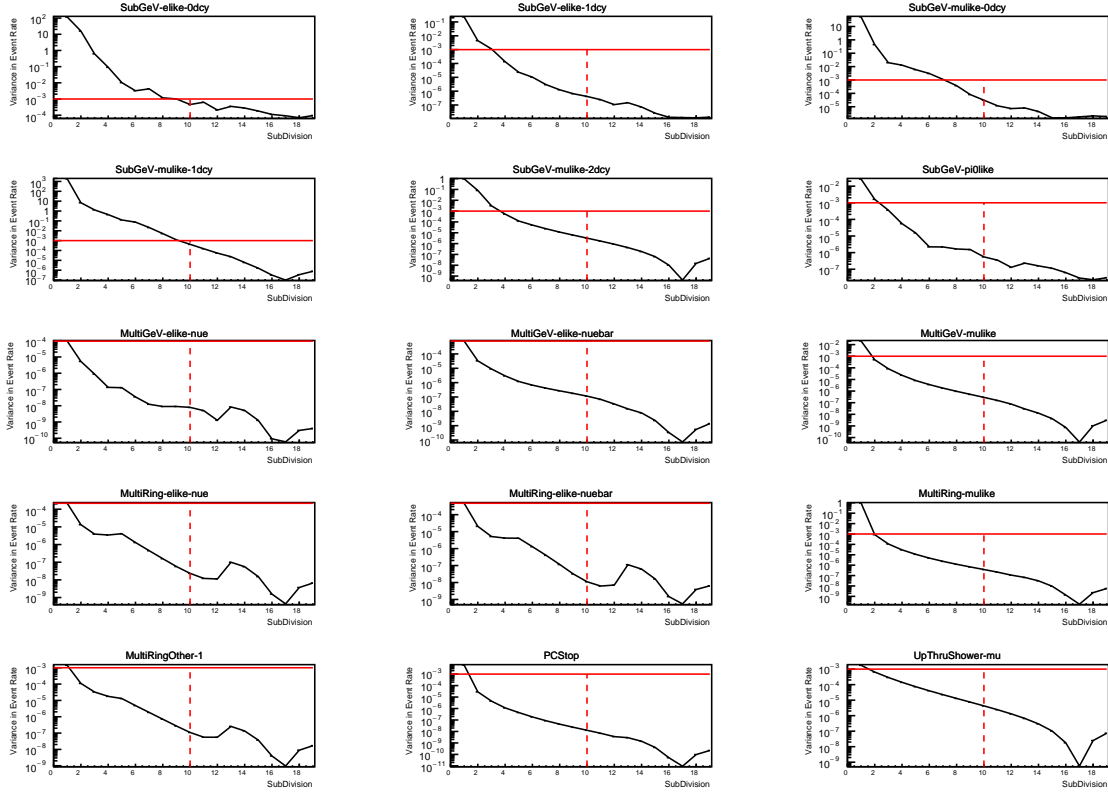


**Figure 6.10:** Variance of event rate for each atmospheric sample as a function of the number of sub-divisions per coarse bin. The solid red line indicates the 0.1% threshold and the dashed red line indicates the variance at a sub-division  $N = 10$ .

1860 likelihood of about  $3 \times 10^{-4}$  which is small enough to be negligible for the oscillation  
 1861 analysis.

1862 Figure 6.12 illustrates the effect of the smearing using  $N = 10$ . The fast oscillations  
 1863 in the sub-GeV upgoing region have been replaced with a normalisation effect whilst  
 1864 the large matter resonance structure remains.

### 1865 6.3 Calculation Engine

1866 As previously discussed in section 6.2, the calculation of oscillation probabilities is per-  
 1867 formed at run-time due to utilising continuous oscillation parameters. Consequently,  
 1868 the time per calculation is crucial for fit performance. The initial fitting framework

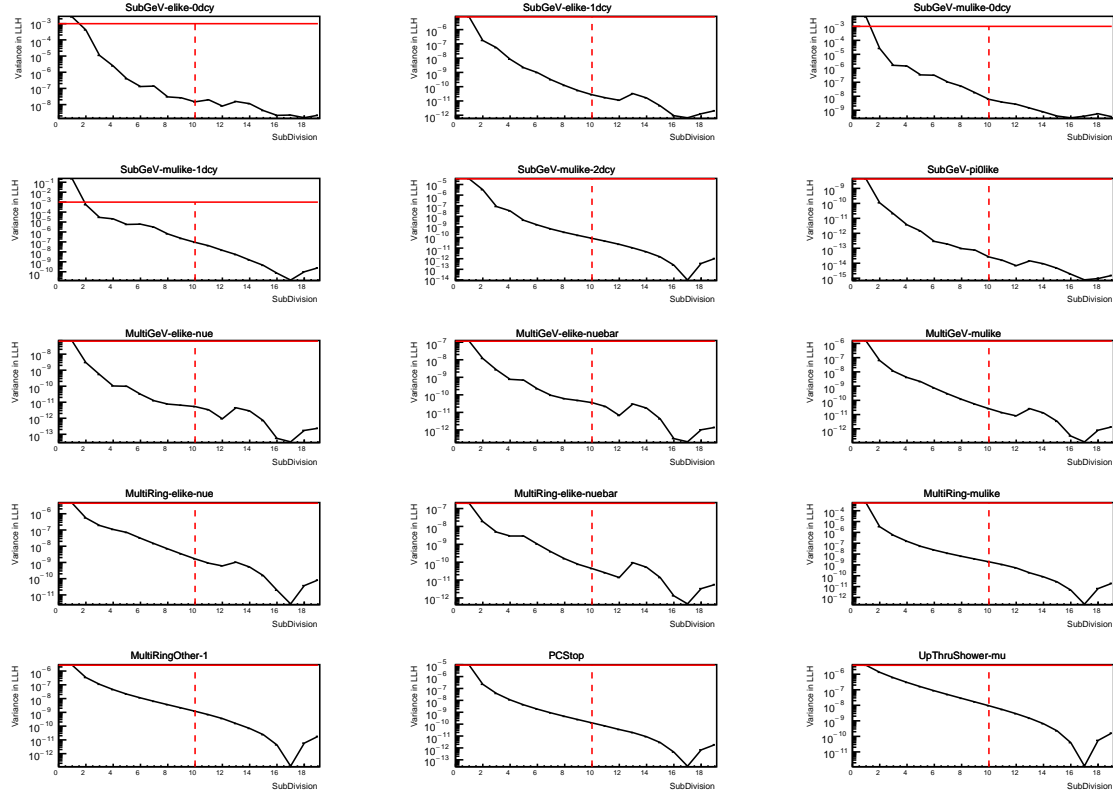


**Figure 6.11:** Variance of sample likelihood, when compared to ‘Asimov data’ set at Asimov A, for each atmospheric sample as a function of the number of sub-divisions per coarse bin. The solid red line indicates the 0.1% threshold and the dashed red line is a graphical indication of the variance at a sub-division  $N = 10$ .

1869 used for this analysis was developed with ProbGPU [193]. This is a GPU-only implemen-  
 1870 tation of the prob3 engine [194]. It is primarily designed for neutrino propagation in a  
 1871 beam experiment (single layer of constant density) with the atmospheric propagation  
 1872 code not being used prior to the analysis in this thesis.

1873 Another engine, CUDAProb3 [195], has been implemented within the fitting frame-  
 1874 work used in this analysis. It has been specifically optimised for atmospheric neutrino  
 1875 oscillation calculation so does not contain the code to replace the beam oscillation  
 1876 calculation. The engine utilises object-orientated techniques as compared to the func-  
 1877 tional implementation of ProbGPU. This allows the energy and cosine zenith arrays to  
 1878 be kept on GPU memory, rather than having to load these arrays onto GPU memory  
 1879 for each calculation. General memory interfacing is one of the slowest tasks which

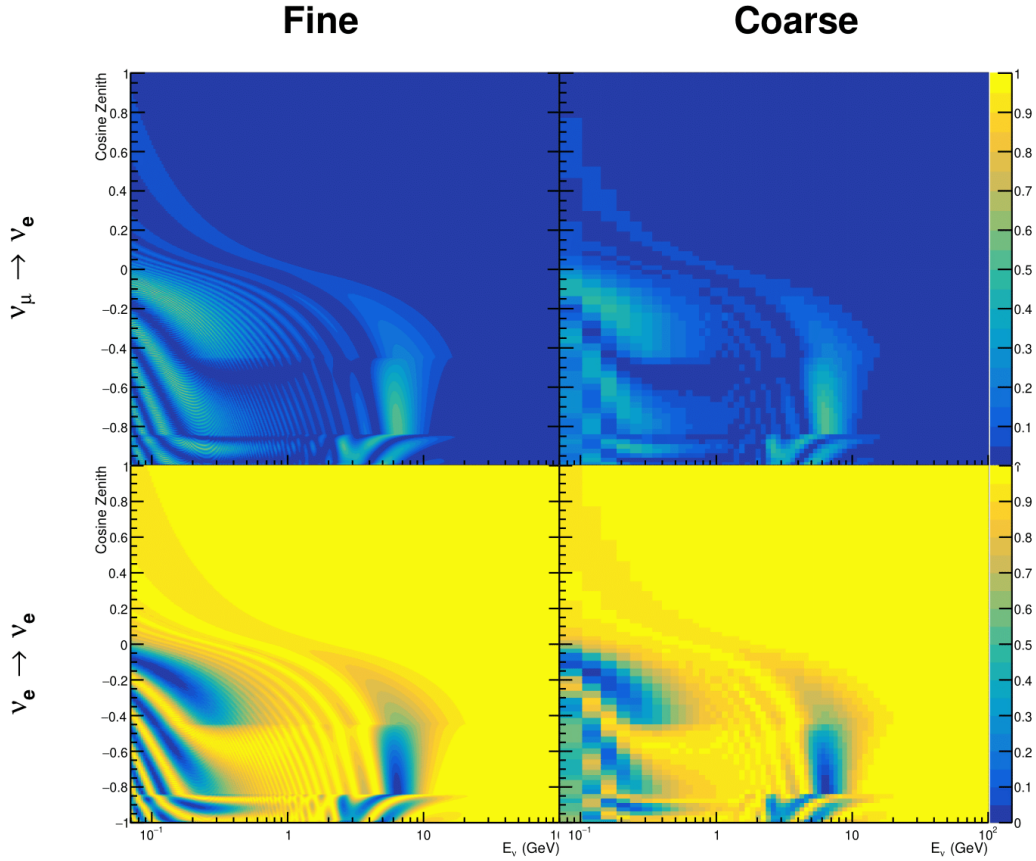


**Figure 6.12:** The oscillation probability,  $P(\nu_\mu \rightarrow \nu_e)$  (top row) and  $P(\nu_e \rightarrow \nu_\mu)$  (bottom row), given as a function of neutrino energy and zenith angle. The left column gives the “fine” binning used to calculate the oscillation probabilities and the right column illustrates the “coarse” binning used to reweight the Monte Carlo events. The fine binning choice is given with  $N = 10$ , which was determined to be below the threshold from Figure 6.10 and Figure 6.11.

1880 GPUs can do, so being able to eliminate this significantly reduces the time required  
 1881 for calculation. This can be seen in Figure 6.13, where the GPU implementation of  
 1882 CUDAProb3 is approximately three times faster than the ProbGPU engine.

1883 Another significant advantage of CUDAProb3 is that it contains a CPU multithreaded  
 1884 implementation which is not possible with the ProbGPU or prob3 engines. This elimi-  
 1885 nates the requirement for GPU resources when submitting jobs to batch systems. As  
 1886 illustrated in Figure 6.13, the calculation speed depends on the number of available

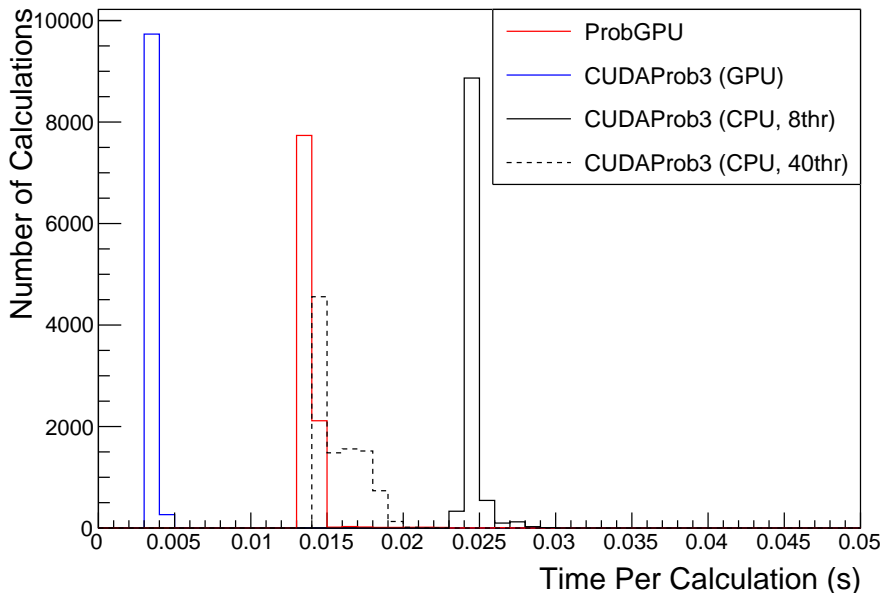


**Figure 6.13:** The calculation time taken to both calculate the oscillation probabilities and fill the “coarse” oscillograms, following the technique given in section 6.2, for the CUDAProb3 and ProbGPU (Red) calculation engines. CUDAProb3 has both a GPU (Blue) and CPU (Black) implementation, where the CPU implementation is multithreaded. Therefore, 8-threads (solid) and 40-threads (dashed) configurations have been tested. Prob3, which is a CPU single-thread implementation has a mean step time of 1.142s.

1887 threads. Using 8 threads (which is typical of the batch systems being used) is ap-  
 1888 proximately twice as slow as the ProbGPU engine implementation, but would allow  
 1889 the fitting framework to be run on many more resources. This fact is utilised for any  
 1890 SK-only fits but GPU resources are required for any fits which include beam samples  
 1891 due to the ProbGPU requirement. Based on the benefits shown by the implementa-  
 1892 tion in this section, efforts are being placed into including linear propagation for beam  
 1893 neutrino propagation into the engine [196].

## 1894 6.4 Matter Density Profile

1895 For an experiment observing atmospheric neutrinos propagating through the Earth, a  
 1896 model of the Earth’s density profile is required. The model used within this analysis is

1897 the Preliminary Reference Earth Model (PREM) [191], as illustrated in Figure 6.1. As  
1898 discussed in section 6.1, the propagator used within the calculation engine requires  
1899 constant density layers. To follow the official SK-only analysis [190], the average  
1900 density of each layer has been taken from the PREM model. Table 6.1 documents  
1901 the density and radii of the layers used within this approximation. The density  
1902 measurements provided in the PREM model are provided in terms of mass density,  
1903 whereas neutrino oscillations are sensitive to the electron number density. This value  
1904 can be computed as the product of the chemical composition, or the  $Z/A$  value, and  
1905 the mass density of each layer. Currently, the only way to calculate the chemical  
1906 composition value for layers close to the Earth’s core is through neutrino oscillations.  
1907 The chemical composition of the upper layers of the Earth’s Mantle and the Transition  
1908 zone is well known due to it being predominantly pyrolite which has a chemical  
1909 composition value of 0.496 [197]. The components of the Earth’s core region are less  
1910 well known. Consequently, the chemical composition dial for the core layers is set to a  
1911 value of 0.468, as calculated in [198]. This value is assigned a Gaussian error with a  
1912 standard deviation equivalent to the difference in chemical composition in core and  
1913 mantle layers. Figure 6.14 illustrates the effect of moving from the  $Z/A = 0.5$  method  
1914 which is used in the official SK-only analysis [190] to these more precise values.

1915 The beam oscillation probability in this thesis uses a baseline of 295km, density  
1916  $2.6\text{g/cm}^3$ , and chemical composition 0.5 as is done by the official T2K-only analysis  
1917 [199].

1918 Whilst the propagator requires a fixed density layer model of the Earth, the density  
1919 only has to be fixed for a specific  $E_\nu \times \cos(\theta_Z)$  bin in a given layer. As the density is a  
1920 function of radius, which is a function of the direction in which a neutrino propagates,  
1921 a better approximation of the PREM model can be made if a  $\cos(\theta_Z)$ -specific density is  
1922 calculated.

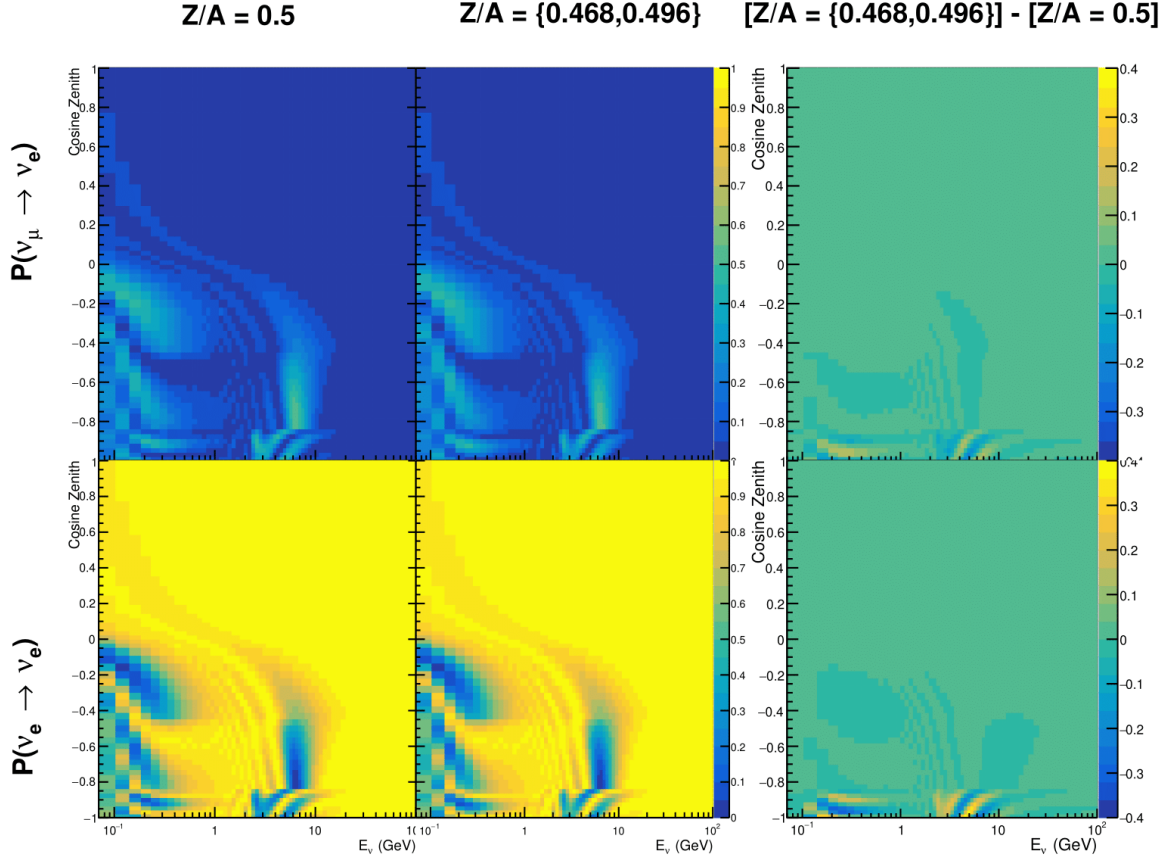


**Figure 6.14:** The oscillation probability,  $P(\nu_\mu \rightarrow \nu_e)$  (top row) and  $P(\nu_e \rightarrow \nu_\mu)$  (bottom row), given as a function of neutrino energy and zenith angle. The left column gives probabilities where the constant  $Z/A = 0.5$  approximation which is used in the official SK-only analysis. The middle column gives the probabilities where  $Z/A = [0.468, 0.498]$  values are used, as given in Table 6.1. The right column illustrates the difference in oscillation probability between the two different techniques.

1923 To achieve this, the average density,  $\langle \rho \rangle_i$ , in the  $i^{th}$  layer, is calculated as the density,  
 1924  $\rho(t)$ , integrated over the track a given  $\cos(\theta_Z)$ ,

$$\langle \rho \rangle_i = \frac{1}{t_{i+1} - t_i} \int_{t_i}^{t_{i+1}} \rho(t) dt \quad (6.6)$$

1925 where  $t_i$  are the intersection points between each layer and  $t$  is the path length of

1926 the trajectory across the layer.

1927 The oscillation probability calculation speed is approximately linear in the number

1928 of layers invoked within the Earth model. Therefore a four-layer model is still utilized

1929 with the only difference to the official SK-only analysis being that the four-layer model

1930 used for each value of  $\cos(\theta_Z)$  is different. Following the method outlined in [200],

1931 a four-layer piecewise quadratic polynomial is fit to the PREM model for the four

1932 layers defined in Table 6.1. This fit was not performed by the author of the thesis

1933 and is documented in [192]. The coefficients of the quadratic fit to each layer are

1934 given in Table 6.2 with the final distribution illustrated in Figure 6.15. The quadratic

1935 approximation is clearly much closer to the PREM model as compared to the constant

1936 density approximation.

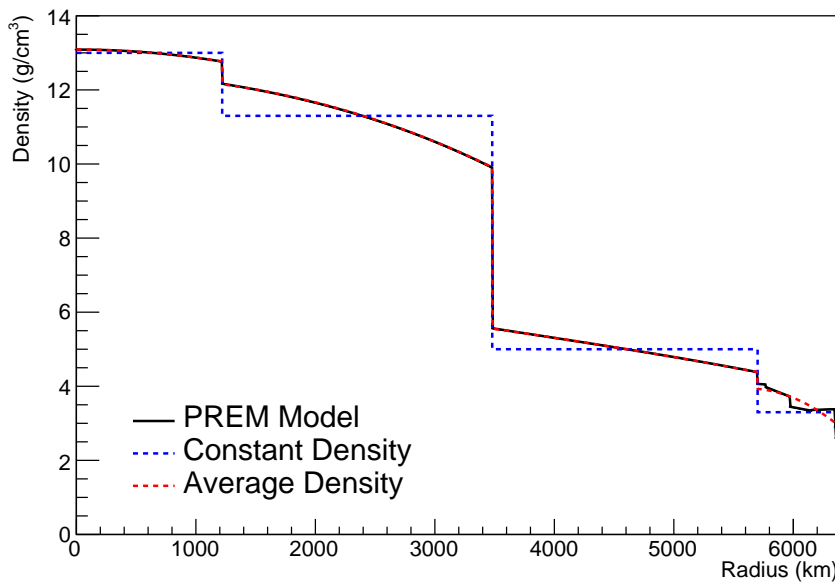


**Figure 6.15:** The density of the Earth given as a function of the radius, as given by the PREM model (Black), the constant density four-layer approximation (Blue), as used in the official SK-only analysis, and the quadratic approximation of the PREM model (Red).

Layer	Outer Radius [km]	Density [g/cm <sup>3</sup> ]
Inner Core	1220	$13.09 - 8.84x^2$
Outer Core	3480	$12.31 + 1.09x - 10.02x^2$
Lower Mantle	5701	$6.78 - 1.56x - 1.25x^2$
Transition Zone	6371	$-50.42 + 123.33x - 69.95x^2$

**Table 6.2:** The quadratic polynomial fits to the PREM model for four assumed layers of the PREM model. The fit to calculate the coefficients is given in [192], where  $x = R/R_{Earth}$ .

1937 The effect of using the quadratic density per  $\cos(\theta_Z)$  model is highlighted in  
 1938 Figure 6.16. The slight discontinuity in the oscillation probability around  $\cos(\theta_Z) \sim -$   
 1939 0.45 in the fixed density model, which is due to the transition to mantle layer boundary,  
 1940 has been reduced. This is expected as the difference in the density across this boundary  
 1941 is significantly smaller in the quadratic density model as compared to the constant  
 1942 density model. Whilst the difference in density across the other layer transitions  
 1943 is reduced, there is still a significant difference. This means the discontinuities in  
 1944 the oscillation probabilities remain but are significantly reduced. However, as the  
 1945 quadratic density approximation matches the PREM model well in this region, these  
 1946 discontinuities are due to the Earth model rather than an artifact of the oscillation  
 1947 calculation.

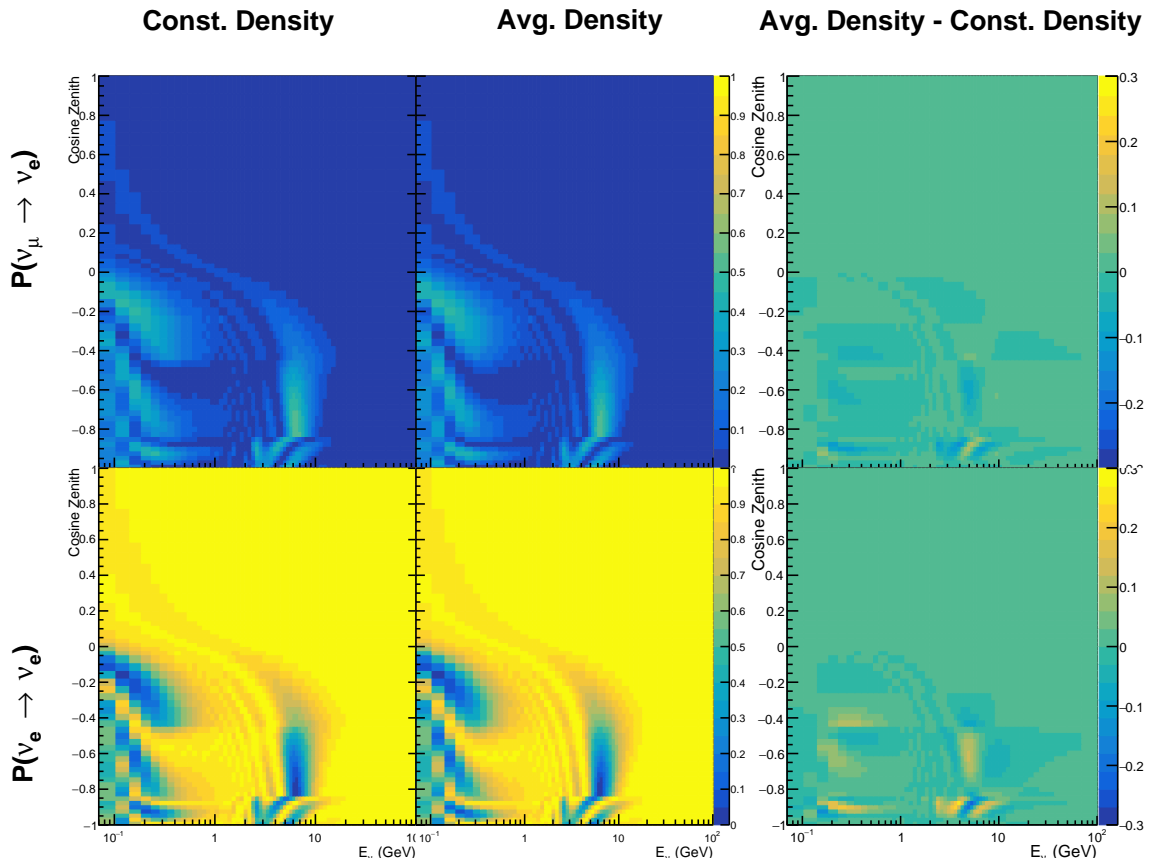


**Figure 6.16:** The oscillation probability,  $P(\nu_\mu \rightarrow \nu_e)$  (top row) and  $P(\nu_e \rightarrow \nu_\mu)$  (bottom row), given as a function of neutrino energy and zenith angle. The left column gives probabilities where the four-layer constant density approximation is used. The middle column gives the probabilities where the density is integrated over the trajectory, using the quadratic PREM approximation, for each  $\cos(\theta_Z)$  is used. The right column illustrates the difference in oscillation probability between the two different techniques.

## <sup>1948</sup> 6.5 Production Height Averaging

<sup>1949</sup> As discussed in section 6.1, the height at which the cosmic ray flux interacts in the  
<sup>1950</sup> atmosphere is not known on an event-by-event basis. The production height can vary  
<sup>1951</sup> from the Earth's surface to  $\sim 50\text{km}$  above that. The SK-only analysis methodology  
<sup>1952</sup> (described in section 6.2) for including the uncertainty on the production height is  
<sup>1953</sup> to include variations from the Honda model when pre-calculating the oscillation  
<sup>1954</sup> probabilities prior to the fit. This technique is not possible for this analysis which  
<sup>1955</sup> uses continuous oscillation parameters that can not be known prior to the fit. Conse-  
<sup>1956</sup> quently, an analytical averaging technique was developed in [192]. The author of this  
<sup>1957</sup> thesis was not responsible for the derivation of the technique but has performed the  
<sup>1958</sup> implementation and validation of the technique for this analysis alone.

<sup>1959</sup> Using the 20 production heights per Monte Carlo neutrino event, provided as 5%  
<sup>1960</sup> percentiles from the Honda flux model, a production height distribution  $p_j(h|E_\nu, \cos\theta_Z)$   
<sup>1961</sup> is built for each neutrino flavour  $j = \nu_e, \bar{\nu}_e, \nu_\mu, \bar{\nu}_\mu$ . In practice, a histogram is filled with  
<sup>1962</sup> 20 evenly spaced bins in production height  $h$  between 0 and 50km. The neutrino energy  
<sup>1963</sup> and cosine zenith binning of the histogram is the same as that provided in section 6.2.  
<sup>1964</sup> The average production height,  $\bar{h} = \int dh \frac{1}{4} \sum_j p_j(h|E_\nu, \cos(\theta_Z))$ , is calculated. The  
<sup>1965</sup> production height binning of this histogram is then translated into  $\delta t(h) = t(\bar{h}) - t(h)$ ,  
<sup>1966</sup> where  $t(h)$  is the distance travelled along the trajectory.

<sup>1967</sup> For the  $i^{\text{th}}$  traversed layer, the transition amplitude,  $D_i(t_{i+1}, t_i)$ , is computed. The  
<sup>1968</sup> time-ordered product of these is then used as the overall transition amplitude via

$$A(t_{n+1}, t_0) = D_n(t_{n+1}, t_n) \dots D_1(t_2, t_1) D_0(t_1, t_0), \quad (6.7)$$

1969

where,

$$\begin{aligned} D_n(t_{n+1}, t_n) &= \exp[-iH_n(t_{n+1} - t_n)] \\ &= \sum_{k=1}^3 C_k \exp[ia_k(t_{n+1} - t_n)] \end{aligned} \quad (6.8)$$

1970 is expressed as a diagonalised time-dependent solution to the Schrodinger equation.

1971 The  $0^{th}$  layer is the propagation through the atmosphere and is the only term that  
 1972 depends on the production height. Using the substitution  $t_0 = t(\bar{h}) - \delta t(h)$ , it can be  
 1973 shown that

$$D_0(t_1, t_0) = D_0(t_1, \bar{h})D_0(\delta t). \quad (6.9)$$

1974

Thus Equation 6.7 becomes

$$\begin{aligned} A(t_{n+1}, t_0) &= D_n(t_{n+1}, t_n) \dots D_1(t_2, t_1)D_0(t_1, \bar{h})D(\delta t) \\ &= A(t_{n+1}, \bar{h}) \sum_{k=1}^3 C_k \exp[ia_k \delta t], \\ &= \sum_{k=1}^3 B_k \exp[ia_k \delta t]. \end{aligned} \quad (6.10)$$

1975

The oscillation probability averaged over production height is then calculated as

$$\begin{aligned}
 \bar{P}(\nu_j \rightarrow \nu_i) &= \int d(\delta t) p_j(\delta t | E_\nu, \cos \theta_Z) P(\nu_j \rightarrow \nu_i) \\
 &= \int d(\delta t) p_j(\delta t | E_\nu, \cos \theta_Z) A(t_{n+1}, t_0) A^*(t_{n+1}, t_0) \\
 &= \sum_{km} (B_k)_{ij} (B_m)_{ij}^* \int d(\delta t) p_j(\delta t | E_\nu, \cos \theta_Z) \exp[i(a_k - a_m)\delta t]
 \end{aligned} \tag{6.11}$$

1976 In practice, implementation in CUDAProb3 [195] is relatively straightforward as  
 1977 the majority of these terms are already calculated in the standard oscillation calculation.  
 1978 Figure 6.17 illustrates the results of the production height averaging. As expected,  
 1979 the main effect is observed in the low-energy downward-going and horizontal-going  
 1980 events. Upward-going events have to travel the radius of the Earth,  $R_E = 6371\text{km}$ ,  
 1981 where the production height uncertainty is a small fraction of the total path length.

1982

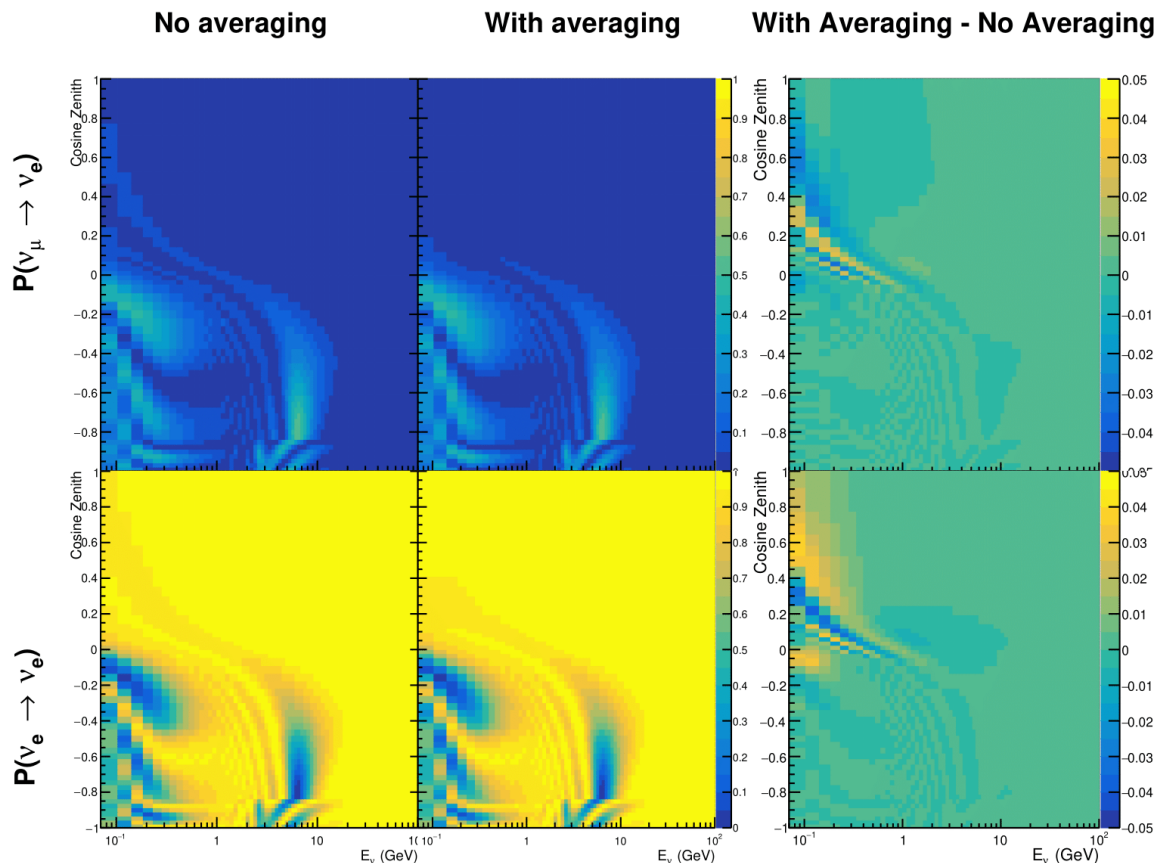


**Figure 6.17:** The oscillation probability,  $P(\nu_\mu \rightarrow \nu_e)$  (top row) and  $P(\nu_e \rightarrow \nu_e)$  (bottom row), given as a function of neutrino energy and zenith angle. The left column gives probabilities where a fixed production height of 25km is used. The middle column gives the probabilities where the production height is analytically averaged. The right column illustrates the difference in oscillation probability between the two different techniques.

# <sup>1983</sup> Bibliography

- <sup>1984</sup> [1] J. Chadwick, Verhandl. Dtsc. Phys. Ges. **16**, 383 (1914).
- <sup>1985</sup> [2] C. D. Ellis and W. A. Wooster, Proc. R. Soc. Lond. A Math. Phys. Sci. **117**, 109 (1927).
- <sup>1986</sup> [3] W. Pauli, Phys. Today **31N9**, 27 (1978).
- <sup>1987</sup> [4] E. Fermi, Z. Phys. **88**, 161 (1934).
- <sup>1988</sup> [5] F. Reines and C. L. Cowan, Phys. Rev. **92**, 830 (1953).
- <sup>1989</sup> [6] C. L. Cowan, F. Reines, F. B. Harrison, H. W. Kruse, and A. D. McGuire, Science **124**, 103 (1956), <http://science.sciencemag.org/content/124/3212/103.full.pdf>.
- <sup>1990</sup> [7] G. Danby *et al.*, Phys. Rev. Lett. **9**, 36 (1962).
- <sup>1991</sup> [8] K. Kodama *et al.*, Physics Letters B **504**, 218 (2001).
- <sup>1992</sup> [9] LSND, A. Aguilar-Arevalo *et al.*, Phys. Rev. **D64**, 112007 (2001), hep-ex/0104049.
- <sup>1993</sup> [10] MiniBooNE Collaboration, A. A. Aguilar-Arevalo *et al.*, Phys. Rev. Lett. **110**, 161801 (2013).
- <sup>1994</sup> [11] Planck Collaboration *et al.*, aap **641** (2020).
- <sup>1995</sup> [12] The ALEPH Collaboration, The Delphi Collaboration, The L3 Collaboration, The SLD Collaboration, The LEP Electroweak Working Group, The SLD Electroweak and Heavy Flavour Groups, J. A. Bagger *et al.*, Physics Reports **427**, 257 (2006).
- <sup>1996</sup> [13] B. Pontecorvo, Sov. Phys. JETP **26**, 984 (1968), [Zh. Eksp. Teor. Fiz. 53, 1717 (1967)].
- <sup>1997</sup> [14] B. Pontecorvo, Sov. Phys. JETP **7**, 172 (1958), [Zh. Eksp. Teor. Fiz. 34, 247 (1957)].
- <sup>1998</sup> [15] M. Kobayashi and T. Maskawa, Progress of Theoretical Physics **49**, 652 (1973).
- <sup>1999</sup> [16] N. Cabibbo, Phys. Rev. Lett. **10**, 531 (1963).
- <sup>2000</sup> [17] A. M. and, Journal of Physics: Conference Series **587**, 012030 (2015).
- <sup>2001</sup> [18] A. Y. Smirnov, (2003).
- <sup>2002</sup> [19] S. Mikheyev and A. Smirnov, Soviet Journal of Nuclear Physics **42**, 913 (1985).

- 2008 [20] L. Wolfenstein, Phys. Rev. D **17**, 2369 (1978).
- 2009 [21] V. D. Barger, K. Whisnant, S. Pakvasa, and R. J. N. Phillips, Phys. Rev. D **22**, 2718 (1980).
- 2010
- 2011 [22] The Super-Kamiokande Collaboration, Y. Ashie *et al.*, Phys. Rev. Lett. **93**, 101801 (2004).
- 2012
- 2013 [23] SNO Collaboration, Q. R. Ahmad *et al.*, Phys. Rev. Lett. **89**, 011301 (2002).
- 2014 [24] 2015 Nobel prize in Physics as listed by Nobelprize.org, [https://www.nobelprize.org/nobel\\_prizes/physics/laureates/2015/](https://www.nobelprize.org/nobel_prizes/physics/laureates/2015/), Accessed: 22-06-2016
- 2015
- 2016
- 2017 [25] J. A. Formaggio and G. P. Zeller, Rev. Mod. Phys. **84**, 1307 (2012), 1305.7513.
- 2018 [26] A. Bellerive, Int. J. Mod. Phys. A **19**, 1167 (2004).
- 2019 [27] R. Davis, D. S. Harmer, and K. C. Hoffman, Phys. Rev. Lett. **20**, 1205 (1968).
- 2020 [28] N. Vinyoles *et al.*, Astrophys. J. **835**, 202 (2017).
- 2021 [29] V. Gribov and B. Pontecorvo, Phys. Lett. B **28**, 493 (1969).
- 2022 [30] K. S. Hirata *et al.*, Phys. Rev. Lett. **63**, 16 (1989).
- 2023 [31] W. Hampel *et al.*, Phys. Lett. B **447**, 127 (1999).
- 2024 [32] SAGE Collaboration, J. N. Abdurashitov *et al.*, Phys. Rev. C **60**, 055801 (1999).
- 2025 [33] Q. R. Ahmad *et al.*, Phys. Rev. Lett. **89** (2002).
- 2026 [34] Borexino Collaboration, Nature **562**, 505 (2018).
- 2027 [35] B. Aharmim *et al.*, Astrophys. J. **653**, 1545 (2006).
- 2028 [36] M. Agostini *et al.*, (2020).
- 2029 [37] S. Andringa *et al.*, Adv. High Energy Phys. **2016**, 1 (2016).
- 2030 [38] J. F. Beacom *et al.*, Chin. phys. C **41**, 023002 (2017).
- 2031 [39] F. An *et al.*, J. Phys. G Nucl. Part. Phys. **43**, 030401 (2016).
- 2032 [40] J. Aalbers *et al.*, (2020), 2006.03114.
- 2033 [41] T. K. Gaisser and M. Honda, (2002).

- 2034 [42] G. D. Barr, T. K. Gaisser, P. Lipari, S. Robbins, and T. Stanev, Physical Review D  
2035 **70** (2004).
- 2036 [43] M. Honda, T. Kajita, K. Kasahara, S. Midorikawa, and T. Sanuki, Physical Review  
2037 D **75** (2007).
- 2038 [44] M. Honda, T. Kajita, K. Kasahara, and S. Midorikawa, Phys. Rev. D **70**, 043008  
2039 (2004).
- 2040 [45] M. Honda, T. Kajita, K. Kasahara, and S. Midorikawa, Phys. Rev. D **83**, 123001  
2041 (2011).
- 2042 [46] A. Fasso, A. Ferrari, P. R. Sala, and J. Ranft, (2001).
- 2043 [47] Y. Ashie *et al.*, Physical Review D **71** (2005).
- 2044 [48] F. Reines *et al.*, Phys. Rev. Lett. **15**, 429 (1965).
- 2045 [49] D. Casper *et al.*, Phys. Rev. Lett. **66**, 2561 (1991).
- 2046 [50] K. S. Hirata *et al.*, Phys. Lett. B **280**, 146 (1992).
- 2047 [51] Z. Li *et al.*, Physical Review D **98** (2018).
- 2048 [52] Kamiokande Collaboration *et al.*, (2017).
- 2049 [53] T2K Collaboration, Nature **580**, 339 (2020).
- 2050 [54] M. A. Acero *et al.*, Phys. Rev. Lett. **123**, 151803 (2019).
- 2051 [55] M. G. Aartsen *et al.*, Phys. Rev. Lett. **120** (2018).
- 2052 [56] P. Adamson *et al.*, Phys. Rev. Lett. **112** (2014).
- 2053 [57] M. S. Athar *et al.*, Progress in Particle and Nuclear Physics **124**, 103947 (2022).
- 2054 [58] G. Danby *et al.*, Phys. Rev. Lett. **9**, 36 (1962).
- 2055 [59] K. Abe *et al.*, Physical Review D **87** (2013).
- 2056 [60] MINOS Collaboration, D. G. Michael *et al.*, Phys. Rev. Lett. **97**, 191801 (2006).
- 2057 [61] G. Danby *et al.*, Phys. Rev. Lett. **9**, 36 (1962).
- 2058 [62] NOvA Collaboration, M. A. Acero *et al.*, Phys. Rev. Lett. **123**, 151803 (2019).
- 2059 [63] B. Abi, R. Acciarri, M. A. Acero, and G. e. a. Adamov, Eur. Phys. J. C Part. Fields

- 2060       **80** (2020).
- 2061 [64] Hyper-Kamiokande Proto-Collaboration *et al.*, Prog. Theor. Exp. Phys. **2015**,  
2062       53C02 (2015).
- 2063 [65] C. Blanco, D. Hooper, and P. Machado, Physical Review D **101** (2020).
- 2064 [66] MicroBooNE Collaboration *et al.*, Search for an Excess of Electron Neutrino  
2065       Interactions in MicroBooNE Using Multiple Final State Topologies, 2021.
- 2066 [67] KARMEN Collaboration, B. Armbruster *et al.*, Phys. Rev. D **65**, 112001 (2002).
- 2067 [68] S.-B. Kim, T. Lasserre, and Y. Wang, Adv. High Energy Phys. **2013**, 1 (2013).
- 2068 [69] M. Sajjad Athar *et al.*, Prog. Part. Nucl. Phys. **124**, 103947 (2022), 2111.07586.
- 2069 [70] K. Abe *et al.*, Nucl. Instrum. Methods Phys. Res. A **1027**, 166248 (2022).
- 2070 [71] F. P. An *et al.*, Phys. Rev. Lett. **108**, 171803 (2012).
- 2071 [72] RENO Collaboration, J. K. Ahn *et al.*, Phys. Rev. Lett. **108**, 191802 (2012).
- 2072 [73] Double Chooz Collaboration, Y. Abe *et al.*, Phys. Rev. Lett. **108**, 131801 (2012).
- 2073 [74] J. Collaboration *et al.*, TAO Conceptual Design Report: A Precision Measurement  
2074       of the Reactor Antineutrino Spectrum with Sub-percent Energy Resolution, 2020,  
2075       2005.08745.
- 2076 [75] for the RENO Collaboration, New results from RENO and the 5 MeV excess,  
2077       AIP Publishing LLC, 2015.
- 2078 [76] Y. Abe *et al.*, Journal of High Energy Physics **2014** (2014).
- 2079 [77] Daya Bay Collaboration, D. Adey *et al.*, Phys. Rev. Lett. **123**, 111801 (2019).
- 2080 [78] M. P. Decowski, Nucl. Phys. B. **908**, 52 (2016).
- 2081 [79] The KamLAND Collaboration, A. Gando *et al.*, Phys. Rev. D **83**, 052002 (2011).
- 2082 [80] P. Dunne, Latest Neutrino oscillation results from T2K, 2020.
- 2083 [81] M. Tanabashi *et al.*, Phys. Rev. D. **98** (2018).
- 2084 [82] Particle Data Group, R. L. Workman and Others, PTEP **2022**, 083C01 (2022).
- 2085 [83] T2K Collaboration, K. Abe *et al.*, Phys. Rev. Lett. **112**, 181801 (2014).

- 2086 [84] Y. Fukuda *et al.*, Phys. Rev. Lett. **81**, 1562 (1998).
- 2087 [85] Linyan Wan, (2022).
- 2088 [86] K. Abe *et al.*, Nuclear Instruments and Methods in Physics Research Section  
2089 A: Accelerators, Spectrometers, Detectors and Associated Equipment **737**, 253  
2090 (2014).
- 2091 [87] S. Fukuda *et al.*, Nucl. Instrum. Methods Phys. Res. A **501**, 418 (2003).
- 2092 [88] Y. Itow *et al.*, (2001).
- 2093 [89] M. Jiang *et al.*, Prog. Theor. Exp. Phys. **2019** (2019).
- 2094 [90] S. Fukuda *et al.*, Nuclear Instruments and Methods in Physics Research Section  
2095 A: Accelerators, Spectrometers, Detectors and Associated Equipment **501**, 418  
2096 (2003), <http://www.sciencedirect.com/science/article/pii/S016890020300425X>.
- 2097 [91] Y. Nakano *et al.*, Nucl. Instrum. Methods Phys. Res. A **977**, 164297 (2020).
- 2098 [92] Hamamatsu, Hamamatsu Photonics Photomultiplier Tubes Handbook.
- 2099 [93] K. Abe *et al.*, Nucl. Instrum. Methods Phys. Res. A **1027**, 166248 (2022).
- 2100 [94] J. F. Beacom and M. R. Vagins, Phys. Rev. Lett. **93**, 171101 (2004).
- 2101 [95] L. Marti *et al.*, Nucl. Instrum. Methods Phys. Res. A **959**, 163549 (2020).
- 2102 [96] L. Marti *et al.*, (2019).
- 2103 [97] M. Vagins, Solar/DSNB Neutrino\_SK-Gd, 2022.
- 2104 [98] J. Focht, PhD thesis, Massachusetts Institute of Technology, 2004.
- 2105 [99] T. Tanimori *et al.*, IEEE Transactions on Nuclear Science **36**, 497 (1989).
- 2106 [100] Super-Kamiokande Collaboration, J. Hosaka *et al.*, Phys. Rev. D **73**, 112001  
2107 (2006).
- 2108 [101] H. Nishino *et al.*, Nucl. Instrum. Methods Phys. Res. A **610**, 710 (2009).
- 2109 [102] S. Yamada *et al.*, IEEE Transactions on Nuclear Science **57**, 428 (2010).
- 2110 [103] S. Yamada, Y. Hayato, Y. Obayashi, and M. Shiozawa, New online system  
2111 without hardware trigger for the Super-Kamiokande experiment, in *2007 IEEE  
2112 Nuclear Science Symposium Conference Record*, IEEE, 2007.

- <sup>2113</sup> [104] G. Carminati, Phys. Procedia **61**, 666 (2015).
- <sup>2114</sup> [105] P. A. Čerenkov, Phys. Rev. **52**, 378 (1937).
- <sup>2115</sup> [106] I. Frank and I. Tamm, Coherent visible radiation of fast electrons passing  
<sup>2116</sup> through matter, in *Selected Papers*, pp. 29–35, Springer Berlin Heidelberg, Berlin,  
<sup>2117</sup> Heidelberg, 1991.
- <sup>2118</sup> [107] The T2K Collaboration, KEK Proposal (2001),  
<sup>2119</sup> <http://neutrino.kek.jp/jhfnu/loi/loi.v2.030528.pdf>.
- <sup>2120</sup> [108] Y. Itow *et al.*, (2001), hep-ex/0106019.
- <sup>2121</sup> [109] The K2K Collaboration and S. H. Ahn, (2001), hep-ex/0103001.
- <sup>2122</sup> [110] The T2K Collaboration, KEK Proposal (2006), [http://j-parc.jp/researcher/Hadron/en/pac\\_0606/pdf/p11-Nishikawa.pdf](http://j-parc.jp/researcher/Hadron/en/pac_0606/pdf/p11-Nishikawa.pdf).
- <sup>2124</sup> [111] C. Bronner, Accelerator Neutrino I\_Recent results from T2K, 2022.
- <sup>2125</sup> [112] T2K Collaboration, K. Abe *et al.*, Phys. Rev. Lett. **112**, 061802 (2014),  
<sup>2126</sup> <https://link.aps.org/doi/10.1103/PhysRevLett.112.061802>.
- <sup>2127</sup> [113] NINJA Collaboration, T. Fukuda *et al.*, Proposal for precise measurement of  
<sup>2128</sup> neutrino-water cross-section in NINJA physics run, Proposal for J-PARC and  
<sup>2129</sup> KEK, 2017.
- <sup>2130</sup> [114] T. Ovsianikova *et al.*, Physics of Particles and Nuclei **48**, 1014 (2017),  
<sup>2131</sup> <https://doi.org/10.1134/S1063779617060478>.
- <sup>2132</sup> [115] M. Antonova *et al.*, Journal of Instrumentation **12**, C07028 (2017),  
<sup>2133</sup> <http://stacks.iop.org/1748-0221/12/i=07/a=C07028>.
- <sup>2134</sup> [116] The T2K Collaboration, K. Abe *et al.*, Phys. Rev. D **102**, 012007 (2020).
- <sup>2135</sup> [117] K. Abe *et al.*, Progress of Theoretical and Experimental Physics **2021** (2021).
- <sup>2136</sup> [118] The T2K Collaboration, K. Abe *et al.*, Nuclear Instruments  
<sup>2137</sup> and Methods in Physics Research Section A: Accelerators, Spectrometers,  
<sup>2138</sup> Detectors and Associated Equipment **659**, 106 (2011),  
<sup>2139</sup> <http://www.sciencedirect.com/science/article/pii/S0168900211011910>.
- <sup>2140</sup> [119] K. Matsuoka *et al.*, Nuclear Instruments and Methods in Physics Research Section  
<sup>2141</sup> A: Accelerators, Spectrometers, Detectors and Associated Equipment **624**, 591

- 2142 (2010), <http://www.sciencedirect.com/science/article/pii/S016890021002098X>.
- 2143 [120] K. Abe *et al.*, Phys. Rev. D. **103** (2021).
- 2144 [121] T. Vladisavljevic, *Predicting the T2K neutrino flux and measuring oscillation parameters* Springer theses, 1 ed. (Springer Nature, Cham, Switzerland, 2020).
- 2145
- 2146 [122] D. Beavis, A. Carroll, and I. Chiang, (1995).
- 2147 [123] P.-A. Amaudruz *et al.*, Nuclear Instruments and Methods in Physics Research  
2148 Section A: Accelerators, Spectrometers, Detectors and Associated Equipment  
2149 **696**, 1 (2012).
- 2150 [124] N. Abgrall *et al.*, Nuclear Instruments and Methods in Physics Research Section  
2151 A: Accelerators, Spectrometers, Detectors and Associated Equipment **637**, 25  
2152 (2011).
- 2153 [125] S. Assylbekov *et al.*, Nuclear Instruments and Methods in Physics Research  
2154 Section A: Accelerators, Spectrometers, Detectors and Associated Equipment  
2155 **686**, 48 (2012).
- 2156 [126] D. Allan *et al.*, Journal of Instrumentation **8**, P10019 (2013).
- 2157 [127] F. Vannucci, Advances in High Energy Physics **2014**, 1 (2014).
- 2158 [128] UA1 magnet sets off for a second new life, 2022.
- 2159 [129] S. Aoki *et al.*, Nuclear Instruments and Methods in Physics Research Section  
2160 A: Accelerators, Spectrometers, Detectors and Associated Equipment **698**, 135  
2161 (2013).
- 2162 [130] K. Suzuki *et al.*, Progress of Theoretical and Experimental Physics **2015**, 53C01  
2163 (2015).
- 2164 [131] S. Brooks, A. Gelman, G. L. Jones, and X.-L. Meng, *Handbook of Markov Chain  
Monte Carlo* (CRC Press, 2011).
- 2165
- 2166 [132] W. R. Gilks, S. Richardson, and D. J. Spiegelhalter, *Markov Chain Monte Carlo in  
Practice* (Chapman & Hall/CRC Interdisciplinary Statistics, 1995).
- 2167
- 2168 [133] C. Wret, *Minimising systematic uncertainties in the T2K experiment using near-  
detector and external data*, PhD thesis, Imperial College London, 2018.
- 2169
- 2170 [134] K. E. Duffy, *Measurement of the Neutrino Oscillation Parameters  $\sin^2 \theta_{23}$ ,  $\Delta m_{32}^2$ ,*

- <sup>2171</sup>  $\sin^2 \theta_{13}$ , and  $\delta_{CP}$  in Neutrino and Antineutrino Oscillation at T2K, PhD thesis, Oriel  
<sup>2172</sup> College, University of Oxford, 2016.
- <sup>2173</sup> [135] T. Bayes, Rev. Phil. Trans. Roy. Soc. Lond. **53**, 370 (1764).
- <sup>2174</sup> [136] N. Metropolis, A. W. Rosenbluth, M. N. Rosenbluth, A. H. Teller, and E. Teller,  
<sup>2175</sup> Journal of Chemical Physics **21** (1970).
- <sup>2176</sup> [137] W. K. Hastings, Biometrika **57** (1970).
- <sup>2177</sup> [138] J. Dunkley, M. Bucher, P. G. Ferreira, K. Moodley, and C. Skordis, Mon. Not. R.  
<sup>2178</sup> Astron. Soc. **356**, 925 (2005).
- <sup>2179</sup> [139] Particle Data Group *et al.*, Prog. Theor. Exp. Phys. **2020** (2020).
- <sup>2180</sup> [140] H. Jeffreys, *The Theory of Probability* Oxford Classic Texts in the Physical Sciences  
<sup>2181</sup> (, 1939).
- <sup>2182</sup> [141] R. E. Kass and A. E. Raftery, J. Am. Stat. Assoc. **90**, 773 (1995).
- <sup>2183</sup> [142] T. Böhlen *et al.*, Nuclear Data Sheets **120**, 211 (2014),  
<sup>2184</sup> <http://www.sciencedirect.com/science/article/pii/S0090375214005018>.
- <sup>2185</sup> [143] R. Brun *et al.*, GEANT: Detector Description and Simulation Tool; Oct 1994 CERN  
<sup>2186</sup> Program Library (CERN, Geneva, 1993), <http://cds.cern.ch/record/1082634>,  
<sup>2187</sup> Long Writeup W5013.
- <sup>2188</sup> [144] T2K Collaboration, K. Abe *et al.*, Phys. Rev. D **87**, 012001 (2013).
- <sup>2189</sup> [145] C. Zeitnitz and T. Gabriel, Nuclear Instruments and Methods in  
<sup>2190</sup> Physics Research Section A: Accelerators, Spectrometers,  
<sup>2191</sup> Detectors and Associated Equipment **349**, 106 (1994),  
<sup>2192</sup> <http://www.sciencedirect.com/science/article/pii/0168900294906130>.
- <sup>2193</sup> [146] A. Fiorentini *et al.*, T2K Technical Note **217** (2017).
- <sup>2194</sup> [147] N. Abgrall *et al.*, Physical Review C **84** (2011).
- <sup>2195</sup> [148] N. Abgrall *et al.*, Physical Review C **85** (2012).
- <sup>2196</sup> [149] N. Abgrall *et al.*, Nuclear Instruments and Methods in Physics Research Section  
<sup>2197</sup> A: Accelerators, Spectrometers, Detectors and Associated Equipment **701**, 99  
<sup>2198</sup> (2013), <http://www.sciencedirect.com/science/article/pii/S016890021201234X>.

- 2199 [150] HARP Collaboration, M. Apollonio *et al.*, Phys. Rev. C **80**, 035208 (2009),  
2200 <https://link.aps.org/doi/10.1103/PhysRevC.80.035208>.
- 2201 [151] B. Blau *et al.*, Nuclear Physics B - Proceedings Supplements **113**, 125 (2002).
- 2202 [152] S. Haino *et al.*, Physics Letters B **594**, 35 (2004).
- 2203 [153] NASA, U.S. Standard Atmosphere, 1976, 1976.
- 2204 [154] S. Roesler, R. Engel, and J. Ranft, The Monte Carlo Event Generator DPMJET-III,  
2205 in *Advanced Monte Carlo for Radiation Physics, Particle Transport Simulation and*  
2206 *Applications*, pp. 1033–1038, Springer Berlin Heidelberg, 2001.
- 2207 [155] K. Niita *et al.*, Radiation Measurements **41**, 1080 (2006).
- 2208 [156] T. Sanuki *et al.*, Physics Letters B **541**, 234 (2002).
- 2209 [157] P. Achard *et al.*, Physics Letters B **598**, 15 (2004).
- 2210 [158] K. Sato, Atmospheric Neutrino\_Reviews on neutrino fluxes (low E atm nu),  
2211 2022.
- 2212 [159] Y. Hayato and L. Pickering, The European Physical Journal Special Topics **230**,  
2213 4469 (2021).
- 2214 [160] Y. Hayato, Acta Physica Polonica B **40** (2009).
- 2215 [161] C. L. Smith, Physics Reports **3**, 261 (1972),  
2216 <http://www.sciencedirect.com/science/article/pii/0370157372900105>.
- 2217 [162] O. Benhar, A. Fabrocini, and S. Fantoni, Nuclear Physics A **497**, 423 (1989).
- 2218 [163] R. Bradford, A. Bodek, H. Budd, and J. Arrington, Nuclear Physics B - Proceedings Supplements **159**, 127 (2006),  
2219 <http://www.sciencedirect.com/science/article/pii/S0920563206005184>,  
2220 Proceedings of the 4th International Workshop on Neutrino-Nucleus Interac-  
2221 tions in the Few-GeV Region.
- 2222 [164] A. A. Aguilar-Arevalo *et al.*, Physical Review D **81** (2010).
- 2223 [165] R. Gran, J. Nieves, F. Sanchez, and M. J. V. Vacas, Phys. Rev. D **88**, 113007 (2013),  
2224 <https://link.aps.org/doi/10.1103/PhysRevD.88.113007>.
- 2225 [166] C. Berger and L. M. Sehgal, Phys. Rev. D **76**, 113004 (2007).

- 2227 [167] C. Berger and L. M. Sehgal, Phys. Rev. D **79**, 053003 (2009),  
2228 <https://link.aps.org/doi/10.1103/PhysRevD.79.053003>.
- 2229 [168] T. Sjöstrand, Computer Physics Communications **82**, 74 (1994).
- 2230 [169] C. Bronner and M. Hartz, Tuning of the Charged Hadrons Multiplicities for Deep  
2231 Inelastic Interactions in NEUT, in *Proceedings of the 10th International Workshop on*  
2232 *Neutrino-Nucleus Interactions in Few-GeV Region (NuInt15)*, Journal of the Physical  
2233 Society of Japan, 2016.
- 2234 [170] M. Glück, E. Reya, and A. Vogt, The European Physical Journal C **5**, 461 (1998).
- 2235 [171] A. Bodek and U.-k. Yang, Axial and Vector Structure Functions for Electron- and  
2236 Neutrino- Nucleon Scattering Cross Sections at all  $Q^2$  using Effective Leading  
2237 order Parton Distribution Functions, 2010.
- 2238 [172] A. Bodek and U.-K. Yang, (2010).
- 2239 [173] S. Gollapinni, (2016).
- 2240 [174] E. S. P. Guerra *et al.*, Phys. Rev. D **99**, 052007 (2019).
- 2241 [175] GEANT4, S. Agostinelli *et al.*, Nucl. Instrum. Meth. **A506**, 250 (2003).
- 2242 [176] R. Brun, F. Bruyant, M. Maire, A. C. McPherson, and P. Zanarini, (1987).
- 2243 [177] K. Abe *et al.*, Physical Review Letters **121** (2018).
- 2244 [178] K. Abe *et al.*, Physical Review D **91** (2015).
- 2245 [179] R. Patterson *et al.*, Nuclear Instruments and Methods in Physics Research Section  
2246 A: Accelerators, Spectrometers, Detectors and Associated Equipment **608**, 206  
2247 (2009).
- 2248 [180] e. a. S. Berkman, T2K Technical Note **146** (2013).
- 2249 [181] e. a. A. Himmel, T2K Technical Note **219** (2015).
- 2250 [182] F. a. James, (1998), CERN Program Library Long Writeups.
- 2251 [183] e. a. D. Barrow, T2K Technical Note **326** (2020).
- 2252 [184] A. Maghrabi, A. Aldosari, and M. Almutairi, Advances in Space Research **68**,  
2253 2941 (2021).

- 2254 [185] Super-Kamiokande Collaboration, K. Abe *et al.*, Phys. Rev. D **97**, 072001 (2018),  
2255 <https://link.aps.org/doi/10.1103/PhysRevD.97.072001>.
- 2256 [186] Particle Data Group, J. Beringer *et al.*, Phys. Rev. D **86**, 010001 (2012).
- 2257 [187] Y. N. and, Journal of Physics: Conference Series **888**, 012191 (2017).
- 2258 [188] M. Jiang, *Study of the neutrino mass hierarchy with the atmospheric neutrino data*  
2259 *collected in Super-Kamiokande IV*, PhD thesis, Kyoto University, 2019.
- 2260 [189] S. N. K. Iyogi and Y. Obayashi., T2K Technical Note **027** (2011).
- 2261 [190] R. Wendell, *Three Flavor Oscillation Analysis of Atmospheric Neutrinos in Super-*  
2262 *Kamiokande*, PhD thesis, University of North Carolina, 2008.
- 2263 [191] A. M. Dziewonski and D. L. Anderson, Phys. Earth Planet. Inter. **25**, 297 (1981).
- 2264 [192] e. a. D. Barrow, T2K Technical Note **425** (2022).
- 2265 [193] R. G. Calland, A. C. Kaboth, and D. Payne, **9**, P04016 (2014).
- 2266 [194] R. Wendell, <http://www.phy.duke.edu/raw22/public/Prob3++/>.
- 2267 [195] F. Kallenborn, C. Hundt, S. Böser, and B. Schmidt, Computer Physics Communi-  
2268 *cations* **234**, 235 (2019).
- 2269 [196] L. Warsame, MaCh3 Analysis Progress.
- 2270 [197] S. Bourret, J. A. B. Coelho, and V. V. E. and, Journal of Physics: Conference Series  
2271 **888**, 012114 (2017).
- 2272 [198] C. Rott, A. Taketa, and D. Bose, Scientific Reports **5** (2015).
- 2273 [199] K. Hagiwara, N. Okamura, and K. ichi Senda, Journal of High Energy Physics  
2274 **2011** (2011).
- 2275 [200] D. Typinski, Earth Gravity, <http://www.typnet.net/Essays/EarthGravGraphics/EarthGrav.pdf>, Accessed: 24-06-2022.  
2276

# <sup>2277</sup> List of Figures

<sup>2278</sup> 2.1	The cross-section of neutrinos from various natural and man-made sources as a function of neutrino energy. Taken from [25] . . . . .	11
<sup>2280</sup> 2.2	The solar neutrino flux as a function of neutrino energy for various fusion reactions and decay chains as predicted by the Standard Solar Model. Taken from [26]. . . . .	12
<sup>2283</sup> 2.3	Left panel: The atmospheric neutrino flux for different neutrino flavours as a function of neutrino energy as predicted by the 2007 Honda model (“This work”) [43], the 2004 Honda model (“HKKM04”) [44], the Bartol model [42] and the FLUKA model [46]. Right panel: The ratio of the muon to electron neutrino flux as predicted by all the quoted models. Both figures taken from [43]. . . . .	14
<sup>2289</sup> 2.4	A diagram illustrating the definition of zenith angle as used in the Super Kamiokande experiment [47]. . . . .	15
<sup>2291</sup> 2.5	Prediction of $\nu_e, \bar{\nu}_e, \nu_\mu, \bar{\nu}_\mu$ fluxes as a function of zenith angle as calculated by the HKKM model [45]. The left, middle and right panels represent three values of neutrino energy, 0.32GeV, 1.0GeV and 3.2GeV respectively. Predictions for other models including Bartol [42], Honda [43] and FLUKA [46] are given in [47]. . . . .	15
<sup>2296</sup> 2.6	Constraints on the atmospheric oscillation parameters, $\sin^2(\theta_{23})$ and $\Delta m_{23}^2$ , from atmospheric and long baseline experiments: SK [52], T2K [53], NO $\nu$ A [54], IceCube [55] and MINOS [56]. Figure taken from [57].	16
<sup>2299</sup> 2.7	Reactor electron antineutrino fluxes for $^{235}\text{U}$ (Black), $^{238}\text{U}$ (Green), $^{239}\text{Pu}$ (Purple), and $^{241}\text{Pu}$ (Orange) isotopes. The inverse $\beta$ -decay cross-section (Blue) and corresponding measurable neutrino spectrum (Red) are also given. Top panel: Schematic of Inverse $\beta$ -decay interaction including the eventual capture of the emitted neutron. This capture emits a $\gamma$ -ray which provides a second signal of the event. Taken from [69]. . . . .	19
<sup>2305</sup> 3.1	A schematic diagram of the Super-Kamiokande Detector. Taken from [88].	26

2306      3.2	The location of “standard PMTs” (red) inside the SK detector. Taken from [86]. . . . .	30
2308      3.3	Schematic view of the data flow through the data acquisition and online system. Taken from [102]. . . . .	34
2310      3.4	The cross-section view of the Tokai to Kamioka experiment illustrating the beam generation facility at J-PARC, the near detector situated at a baseline of 280m and the Super Kamiokande far detector situated 295km from the beam target. . . . .	37
2314      3.5	The near detector suite for the T2K experiment showing the ND280 and INGRID detectors. The distance between the detectors and the beam target is 280m. . . . .	38
2317      3.6	Top panel: Bird’s eye view of the most relevant part of primary and sec- ondary beamline used within the T2K experiment. The primary beam- line is the main-ring proton synchrotron, kicker magnet, and graphite target. The secondary beamline consists of the three focusing horns, decay volume, and beam dump. Figure taken from [118]. Bottom panel: The side-view of the secondary beamline including the focusing horns, beam dump and neutrino detectors. Figure taken from [119]. . . . .	39
2324      3.7	The Monte Carlo prediction of the energy spectrum for each flavour of neutrino ( $\nu_e$ , $\bar{\nu}_e$ , $\nu_\mu$ and $\bar{\nu}_\mu$ ) in the neutrino dominated beam FHC mode (Left) and antineutrino dominated beam RHC mode (Right) expected at SK. Taken from [120]. . . . .	41
2328      3.8	Top panel: T2K muon neutrino disappearance probability as a function of neutrino energy. Middle panel: T2K electron neutrino appearance probability as a function of neutrino energy. Bottom panel: The neutrino flux distribution for three different off-axis angles (Arbitrary units) as a function of neutrino energy. . . . .	42
2333      3.9	The components of the ND280 detector. The neutrino beam travels from left to right. Taken from [118]. . . . .	43
2335      3.10	Comparison of data to Monte Carlo prediction of integrated deposited energy as a function of track length for particles that stopped in FGD1. Taken from [123]. . . . .	45

2338	3.11 Schematic design of a Time Projection Chamber detector. Taken from [124].	46
2339	3.12 The distribution of energy loss as a function of reconstructed momentum for charged particles passing through the TPC, comparing data to Monte Carlo prediction. Taken from [124].	47
2340		
2341		
2342	3.13 A schematic of the P0D side-view. Taken from [125].	48
2343	3.14 Left panel: The Interactive Neutrino GRID on-axis Detector. 14 modules are arranged in a cross-shape configuration, with the center modules being directly aligned with the on-axis beam. Right panel: The layout of a single module of the INGRID detector. Both figures are recreated from [118].	51
2344		
2345		
2346		
2347		
2348	4.1 Example of using Monte Carlo techniques to find the area under the blue line. The gradient and intercept of the line are 0.4 and 1.0 respectively. The area found to be under the curve using one thousand samples is 29.9 units.	56
2349		
2350		
2351		
2352	4.2 The area under a line of gradient 0.4 and intercept 1.0 for the range $0 \leq x \leq 10$ as calculated using Monte Carlo techniques as a function of the number of samples used in each repetition. The analytical solution to the area is 30 units as given by the red line.	57
2353		
2354		
2355		
2356	4.3 Three MCMC chains, each with a stationary distribution equal to a Gaussian centered at 0 and width 1 (As indicated by the black dotted lines). All of the chains use a Gaussian proposal function but have different widths (or 'step size $\sigma$ '). The top panel has $\sigma = 0.1$ , middle panel has $\sigma = 0.5$ and the bottom panel has $\sigma = 5.0$ .	62
2357		
2358		
2359		
2360		
2361	4.4 The log-likelihood from the fit detailed in <a href="#">DB: Link to AsimovA Sensitivity Section</a> as a function of the number of steps accumulated in each fit. Many independent MCMC chains were run in parallel and overlaid on this plot. The red line indicates the $1 \times 10^5$ step burn-in period after which the log-likelihood becomes stable.	63
2362		
2363		
2364		
2365		

2366      4.5	Left: The two dimensional probability distribution for two correlated parameters $x$ and $y$ . The red distribution shows the two dimensional probability distribution when $0 \leq x \leq 5$ . Right: The marginalised probability distribution for the $y$ parameter found when requiring the $x$ to be bound between $-5 \leq x \leq 5$ and $0 \leq x \leq 5$ for the black and red distribution, respectively. . . . .	66
2372      5.1	The NEUT prediction of the $\nu_\mu$ -H <sub>2</sub> O cross-section overlaid on the T2K $\nu_\mu$ flux. The charged current (black, solid) and neutral current (black, dashed) inclusive, charged current quasi-elastic (blue, solid), charged current 2p2h (blue, dashed), charged current single pion production (pink), and charged current multi- $\pi$ and DIS (Purple) cross-sections are illustrated. Figure taken from [159]. . . . .	74
2378      5.2	Illustration of the various processes which a pion can undergo before exiting the nucleus. Taken from [173]. . . . .	75
2380      5.3	Event displays from Super Kamiokande illustrating the “crisp” ring from a muon and the typically “fuzzier” electron ring. Each pixel represents a PMT and the color scheme denotes the accumulated charge deposited on that PMT. Figures taken from [181]. . . . .	78
2384      5.4	The electron/muon PID separation parameter for all sub-GeV single-ring events in SK-IV. The charged current (CC) component is broken down in four flavours of neutrino ( $\nu_\mu$ , $\bar{\nu}_\mu$ , $\nu_e$ and $\bar{\nu}_e$ ). Events with positive values of the parameter are determined to be electron-like. . .	82
2388      5.5	The variation of the measured dark rate as a function of date, broken down by PMT type. The SK-IV and SK-V periods span September 2008 to May 2018 and January 2019 to July 2020, respectively. The break in measurement in 2018 corresponds to the period of tank repair and refurbishment. Figure adapted from [183]. . . . .	84
2393      5.6	Comparison of the measured raw charge deposited per event from the stopping muon data samples between SK-IV (Blue) and SK-V (Red), split by the primary muon subevent and the associated decay electron subevent. . . . .	85

2397	5.7	The distribution of the reconstructed momentum from the muon ring divided by the distance between the reconstructed muon and decay electron vertices as found in the stopping muon data sets of SK-IV (Black) and SK-IV (Red). Only events with one tagged decay electron are considered. A Gaussian fit is considered in the range [2.0, 2.4] MeV/cm and illustrated as the solid curve. . . . .	86
2403	5.8	The $\chi^2$ difference between the SK-IV and SK-V reconstructed muon momentum divided by range when the SK-V is modified by the scaling parameter $\alpha$ . Both additive (Blue) and multiplicative (Black) scaling factors have been considered. In practice, the additive scaling factor actually uses the value of $(\alpha - 1.0)$ but is illustrated like this so the results can be shown on the same axis range. . . . .	87
2409	5.9	A depiction of the topology patterns for fully-contained (FC), partially-contained (PC) and up-going muon (Up- $\mu$ ) samples included in this analysis. . . . .	88
2412	5.10	The predicted neutrino flux of the fully contained (FC) sub-GeV and multi-GeV, partially contained (PC), and upward-going muon (Up- $\mu$ ) events. The prediction is broken down by the $\nu_x \rightarrow \nu_e$ prediction (top left), $\nu_x \rightarrow \nu_\mu$ prediction (top right) and $\nu_x \rightarrow \nu_\tau$ prediction (bottom). All systematic dials are set to their nominal values and the Asimov A oscillation parameters are assumed. . . . .	90
2418	6.1	The density of the Earth given as a function of the radius, as given by the PREM model (Black), and the constant density four-layer approximation (Blue), as used in the official SK-only analysis. . . . .	95
2421	6.2	An “oscillogram” that depicts the $P(\nu_\mu \rightarrow \nu_e)$ oscillation probability as a function of neutrino energy and cosine of the zenith angle. The zenith angle is defined such that $\cos(\theta_Z) = 1.0$ represents neutrinos that travel from directly above the detector. The four-layer constant density PREM model approximation is used and Asimov A oscillation parameters are assumed (Table 2.2). . . . .	95

2427      6.3	The effect of $\delta_{CP}$ for atmospheric neutrinos given in terms of the neutrino energy and zenith angle. This oscillogram compares the $P(\nu_\mu \rightarrow \nu_e)$ oscillation probability for a CP conserving ( $\delta_{CP} = 0.0$ ) and a CP violating ( $\delta_{CP} = -1.601$ ) value taken from the Asimov A parameter set. The other oscillation parameters assume the Asimov A oscillation parameter set given in Table 2.2. . . . .	97
2433      6.4	An illustration of the matter-induced effects on the oscillation probability, given as a function of neutrino energy and zenith angle. The top row of panels gives the $P(\nu_e \rightarrow \nu_e)$ oscillation probability and the bottom row illustrates the $P(\bar{\nu}_e \rightarrow \bar{\nu}_e)$ oscillation probability. The left column highlights the oscillation probability in a vacuum, whereas the middle and right column represents the oscillation probabilities when the four-layer fixed density PREM model is assumed. All oscillation probabilities assume the “Asimov A” set given in Table 2.2, but importantly, the right column sets an inverted mass hierarchy. The “matter resonance” effects at $E_\nu \sim 5\text{GeV}$ can be seen in the $P(\nu_e \rightarrow \nu_e)$ for normal mass hierarchy and $P(\bar{\nu}_e \rightarrow \bar{\nu}_e)$ for inverted hierarchy. . . . .	98
2444      6.5	The oscillation probability for beam neutrino events given as a function of neutrino energy. All oscillation parameters assume the “Asimov A” set given in Table 2.2 unless otherwise stated. Each panel represents a change in one of the oscillation parameters whilst keeping the remaining parameters fixed. . . . .	99
2449      6.6	The number of electron-like events in the FHC and RHC operating mode of the beam, as a function of the oscillation probabilities. Both normal hierarchy (Solid) and inverse hierarchy (Dashed) values of $\Delta m_{23}^2$ are given. . . . .	100
2453      6.7	The oscillation probability $P(\nu_\mu \rightarrow \nu_e)$ , given as a function of neutrino energy and zenith angle, which highlights an example of the “fast” oscillations in the sub-GeV upgoing region. . . . .	102
2456      6.8	Illustration of the averaging procedure for $N = 2$ . The oscillation probabilities calculated on the finer left binning are averaged to obtain the oscillation probabilities in the coarser right binning. These averaged oscillation probabilities with the coarser binning are then applied to each event during the fit. . . . .	104

2461	6.9 Event rate of the SubGeV_elike_0dcy sample as a function of the num- 2462 ber of sub-divisions per coarse bin. Each subplot represents the event 2463 rate of the sample at a different oscillation parameter set thrown from 2464 the PDG priors detailed in Table 2.1. The red line in each subplot 2465 represents the mean of the event rate over the different values of sub- 2466 divisions for that particular oscillation parameter throw. . . . .	106
2467	6.10 Variance of event rate for each atmospheric sample as a function of the 2468 number of sub-divisions per coarse bin. The solid red line indicates 2469 the 0.1% threshold and the dashed red line indicates the variance at a 2470 sub-division $N = 10$ . . . . .	107
2471	6.11 Variance of sample likelihood, when compared to ‘Asimov data’ set 2472 at Asimov A, for each atmospheric sample as a function of the num- 2473 ber of sub-divisions per coarse bin. The solid red line indicates the 2474 0.1% threshold and the dashed red line is a graphical indication of the 2475 variance at a sub-division $N = 10$ . . . . .	108
2476	6.12 The oscillation probability, $P(\nu_\mu \rightarrow \nu_e)$ (top row) and $P(\nu_e \rightarrow \nu_e)$ (bot- 2477 tom row), given as a function of neutrino energy and zenith angle. The 2478 left column gives the “fine” binning used to calculate the oscillation 2479 probabilities and the right column illustrates the “coarse” binning used 2480 to reweight the Monte Carlo events. The fine binning choice is given 2481 with $N = 10$ , which was determined to be below the threshold from 2482 Figure 6.10 and Figure 6.11. . . . .	109
2483	6.13 The calculation time taken to both calculate the oscillation probabilities 2484 and fill the “coarse” oscillograms, following the technique given in 2485 section 6.2, for the CUDAProb3 and ProbGPU (Red) calculation engines. 2486 CUDAProb3 has both a GPU (Blue) and CPU (Black) implementation, 2487 where the CPU implementation is multithreaded. Therefore, 8-threads 2488 (solid) and 40-threads (dashed) configurations have been tested. Prob3, 2489 which is a CPU single-thread implementation has a mean step time of 2490 1.142s. . . . .	110

- |      |  |     |
|------|--|-----|
| 2491 | 6.14 The oscillation probability, $P(\nu_\mu \rightarrow \nu_e)$ (top row) and $P(\nu_e \rightarrow \nu_e)$ (bottom row), given as a function of neutrino energy and zenith angle. The left column gives probabilities where the constant $Z/A = 0.5$ approximation which is used in the official SK-only analysis. The middle column gives the probabilities where $Z/A = [0.468, 0.498]$ values are used, as given in Table 6.1. The right column illustrates the difference in oscillation probability between the two different techniques. . . . .                    | 112 |
| 2498 | 6.15 The density of the Earth given as a function of the radius, as given by the PREM model (Black), the constant density four-layer approximation (Blue), as used in the official SK-only analysis, and the quadratic approximation of the PREM model (Red). . . . .  | 113 |
| 2502 | 6.16 The oscillation probability, $P(\nu_\mu \rightarrow \nu_e)$ (top row) and $P(\nu_e \rightarrow \nu_e)$ (bottom row), given as a function of neutrino energy and zenith angle. The left column gives probabilities where the four-layer constant density approximation is used. The middle column gives the probabilities where the density is integrated over the trajectory, using the quadratic PREM approximation, for each $\cos(\theta_Z)$ is used. The right column illustrates the difference in oscillation probability between the two different techniques. | 115 |
| 2509 | 6.17 The oscillation probability, $P(\nu_\mu \rightarrow \nu_e)$ (top row) and $P(\nu_e \rightarrow \nu_e)$ (bottom row), given as a function of neutrino energy and zenith angle. The left column gives probabilities where a fixed production height of 25km is used. The middle column gives the probabilities where the production height is analytically averaged. The right column illustrates the difference in oscillation probability between the two different techniques.   | 119 |

# 2515 List of Tables

<small>2516</small>	2.1	The 2018 Particle Data Group constraints of the oscillation parameters taken from [81]. The value of $\Delta m_{23}^2$ is given for both normal hierarchy (N.H.) and inverted hierarchy (I.H.) and $\sin^2(\theta_{23})$ is broken down by whether its value is below (Q1) or above (Q2) 0.5. . . . .	<small>2517</small> 21
<small>2518</small>	2.2	Reference values of the neutrino oscillation parameters for two different oscillation parameter sets. . . . .	<small>2519</small> 23
<small>2520</small>	3.1	The various SK periods and respective live-time. The SK-VI live-time is calculated until 1 <sup>st</sup> April 2022. SK-VII started during the writing of this thesis. . . . .	<small>2521</small> 25
<small>2522</small>	3.2	The trigger thresholds and extended time windows saved around an event which were utilised throughout the SK-IV period. The exact thresholds can change and the values listed here represent the thresholds at the start and end of the SK-IV period. . . . .	<small>2523</small> 34
<small>2524</small>	3.3	The threshold momentum and energy for a particle to generate Cherenkov light in ultrapure water, as calculated in Equation 3.2 in ultrapure water which has refractive index $n = 1.33$ . . . . .	<small>2525</small> 36
<small>2526</small>	4.1	Jeffreys scale for strength of preference for two models $A$ and $B$ as a function of the calculated Bayes factor ( $B_{AB} = B(A/B)$ ) between the two models [140]. The original scale is given in terms of $\log_{10}(B(A/B))$ but converted to linear scale for easy comparison throughout this thesis.	<small>2527</small> 68
<small>2528</small>	6.1	Description of the four layers of the Earth invoked within the constant density approximation of the PREM model [191]. . . . .	<small>2529</small> 94
<small>2530</small>	6.2	The quadratic polynomial fits to the PREM model for four assumed layers of the PREM model. The fit to calculate the coefficients is given in [192], where $x = R/R_{Earth}$ . . . . .	<small>2531</small> 114
<small>2532</small>			
<small>2533</small>			
<small>2534</small>			
<small>2535</small>			
<small>2536</small>			
<small>2537</small>			
<small>2538</small>			
<small>2539</small>			
<small>2540</small>			